

RICE UNIVERSITY

**Title TBD**

by

**Roger Ding**

A THESIS SUBMITTED  
IN PARTIAL FULFILLMENT OF THE  
REQUIREMENTS FOR THE DEGREE

**Doctor of Philosophy**

APPROVED, THESIS COMMITTEE:

---

F. Barry Dunning, *Chair*  
Sam and Helen Worden Professor of Physics

---

Thomas C. Killian  
Professor of Physics and Astronomy

---

Junichiro Kono  
Professor of Electrical and Computer Engineering  
Professor of Physics and Astronomy

HOUSTON, TEXAS

JUNE 2019

**ABSTRACT**

**Title TBD**

by

**Roger Ding**

Abstract goes here.

## ACKNOWLEDGMENTS

Acknowledgments go here.

Person 1 Person 1 description.

Person 2 Person 2 description.

Person 3 Person 3 description.

Person 4 Person 4 description.

## Table of Contents

<b>1</b>	<b>Introduction</b>	<b>1</b>
1.1	Motivation . . . . .	1
1.2	Strontium Rydberg Atoms . . . . .	3
1.3	Rydberg Dressing . . . . .	3
1.4	Long-Range Interactions . . . . .	4
<b>2</b>	<b>Strontium Rydberg Experiment</b>	<b>5</b>
2.1	Producing Cold and Ultracold Gases of Strontium . . . . .	5
2.1.1	Pre-cooling on the 461 nm Transition . . . . .	6
2.1.2	461 nm “Blue” MOT and Magnetic Trap . . . . .	8
2.1.3	689 nm “Red” MOT . . . . .	10
2.1.4	Optical Dipole Trap . . . . .	12
2.2	Vacuum System . . . . .	14
2.2.1	Source-side Vacuum System . . . . .	15
2.2.2	Zeeman Slower . . . . .	17
2.2.3	Experiment-side Vacuum System . . . . .	18
2.3	Magnetic Field Trim Coils . . . . .	20
2.4	Dual MOT Coils . . . . .	21
2.5	Laser Systems for Producing Cold and Ultracold Strontium Gases . . . . .	24
2.5.1	461 nm “Blue” Laser System . . . . .	24
2.5.2	481 nm Repumping System . . . . .	28
2.5.3	689 nm “Red” Laser System . . . . .	29

Chapter	Page
2.5.4 Optical Dipole Trap System . . . . .	33
2.6 Making and Detecting Rydberg Atoms . . . . .	35
2.6.1 320 nm UV Laser System . . . . .	35
2.6.2 Electric Field System . . . . .	38
2.6.3 Charged Particle Detection . . . . .	41
<b>3 Spectroscopy of <math>^{87}\text{Sr}</math> Triplet Rydberg States</b>	<b>47</b>
3.1 Ionization Limit of $^{87}\text{Sr}$ . . . . .	48
3.2 Hyperfine Rydberg States of $^{87}\text{Sr}$ . . . . .	49
3.2.1 Singly Excited $S$ states . . . . .	51
3.2.2 Singly Excited $D$ states . . . . .	60
3.3 Experimental Method . . . . .	61
3.3.1 Calibrating the EXFO WA-1500 Wavemeter . . . . .	63
3.4 Results and Discussion . . . . .	65
3.5 Conclusion . . . . .	74
<b>4 Excited Dimer Rydberg Molecules</b>	<b>79</b>
4.1 Experiment . . . . .	79
4.1.1 Spin-Polarization . . . . .	79
4.1.2 Density correction term . . . . .	80
4.2 Experimental Results . . . . .	80
4.3 Conclusion . . . . .	80
<b>5 Progress Towards an <i>In Situ</i> Measurement of <math>g^{(3)}(R)</math></b>	<b>81</b>
5.0.1 Correcting for density . . . . .	81
5.1 Results . . . . .	81
5.2 Conclusion . . . . .	81

Chapter	Page
<b>6 Conclusions</b>	<b>83</b>
<b>A Isotope-Dependent Optical Trapping</b>	<b>85</b>
A.1 Challenges in Producing Quantum Degenerate Gases of $^{88}\text{Sr}$ and $^{87}\text{Sr}$ . . . . .	85
A.2 Isotope-Dependent Optical Trapping . . . . .	86
A.2.1 Trap Design . . . . .	87
A.2.2 Polarizability . . . . .	90
A.3 Single-Isotope Testing with $^{84}\text{Sr}$ . . . . .	91
A.3.1 Producing an $^{84}\text{Sr}$ BEC in the Dimple . . . . .	93
A.4 Sympathetically Cooling $^{88}\text{Sr}$ with $^{86}\text{Sr}$ . . . . .	93
A.5 Proposal Sympathetically Cooling $^{87}\text{Sr}$ with $^{86}\text{Sr}$ . . . . .	93
A.6 Preliminary Conclusions and Future Directions . . . . .	95
<b>B Notations and Definitions</b>	<b>97</b>
B.1 Symbols used in optical diagrams . . . . .	97
<b>C Strontium Data</b>	<b>99</b>
C.1 Physical Properties . . . . .	99
C.2 Scattering Properties . . . . .	99
C.3 Electronic properties . . . . .	99
C.4 Rydberg Properties . . . . .	100
C.4.1 Mass-scaled $^{87}\text{Sr}$ ionization limit . . . . .	100
C.4.2 Strontium Rydberg Constant . . . . .	101
C.4.3 Data from papers . . . . .	102
C.5 Measured Strontium Rydberg Energies . . . . .	102
C.6 Data presented in Ding et al. . . . .	111

Chapter	Page
<b>D Optical Dipole Traps</b>	<b>113</b>
D.1 Optical Dipole Potential . . . . .	113
D.1.1 A tale of three lasers . . . . .	114
<b>E Absorption Imaging of Strontium</b>	<b>115</b>
E.1 Imaging $^{84}\text{Sr}$ , $^{86}\text{Sr}$ , and $^{88}\text{Sr}$ . . . . .	115
E.2 Imaging $^{87}\text{Sr}$ . . . . .	116
<b>F Tips and Tricks</b>	<b>117</b>
F.1 Working with (high-power) fibers . . . . .	117
F.2 Fiber injection lock slave lasers . . . . .	117
F.3 Scanning the UV laser . . . . .	117
F.3.1 Switching sidebands to increase scan range . . . . .	118
F.3.2 “Continuous” scanning of the transfer cavity . . . . .	118
F.4 Winding coils on aluminum U-channels . . . . .	118
F.5 Hard Drive Shutters and Drivers . . . . .	119
<b>G Suggested Upgrades</b>	<b>121</b>
G.0.1 Locking the 481 nm with a “Super Lock” . . . . .	121
G.0.2 Upgrading to a ULE Cavity . . . . .	121
G.0.3 Redoing the 1064 nm ODT system . . . . .	122
G.0.4 Fiber-Coupling the Red MOT . . . . .	123
<b>H Derivations</b>	<b>125</b>
H.1 Gaussian Beams . . . . .	125
H.1.1 Circular Gaussian Beam . . . . .	128
H.2 Unitary transformation . . . . .	128

Chapter	Page
H.3 Hyperfine Mixing Matrix Elements . . . . .	129
H.3.1 Singly excited $S$ states . . . . .	130
H.3.2 $D$ -states . . . . .	133
H.4 Density distributions . . . . .	135
H.4.1 Harmonic approximation . . . . .	135
<b>I Various Drawings</b>	<b>137</b>
I.1 Dual MOT Coils . . . . .	137
<b>Bibliography</b>	<b>139</b>

# 1. Introduction

---

## 1.1 Motivation

\*\*\*\*\* (0) Long-range and anisotropic interactions

(0a) Few-/Many-body physics

(0b) Ultra-long-range Rydberg molecules

(1) Spectroscopy

(2) Effects of quantum statistics – use Joe’s figure?

Add in repumper spectrum.

\*\*\* Need good intro to why study long-range interactions \*\*\*

The ability to produce ~~cold~~ and ultracold samples paved the way towards achievement of quantum degenerate gases of atoms which are ideal systems for studying quantum interactions. From the observation of BEC-BCS crossover, to xxx, and yyyy, most of the work so far has been based on short-range, isotropic contact interactions which require the atomic wave functions to overlap. An “easy” way to extend these systems to more complexity and to study other phenomena \*\* D-wave super conductors? \*\* is to incorporate long-range interactions. Now, the atoms no longer need to have an overlap to interact.

The three primary methods for incorporating long-range interactions into quantum systems are currently being pursued:

**Polar molecules** The addition of an extra body to a single atom leads to a wealth of additional effects and complexity. Using bialkali as an example, heteronuclear molecules can have large (permanent) electric dipole moments [1]. The drawback is that the

An important recent trend in the field of ultracold atomic gases is the study of systems with long-range interactions.

additional complexity typically makes it very difficult to produce ultracold and quantum degenerate samples. Steady progress has been made in the direct laser cooling of molecules [2] as well as the recent producing of a degenerate Fermi gas of  $^{40}\text{K}^{87}\text{Rb}$  [3] produced by photoassociating ultracold atoms. These have the advantage of, ignoring chemical reactions for now, extremely long lifetimes.

**Magnetic atoms** Atoms themselves can have permanent dipole moments which can be used to study long-range interactions. Quantum degeneracy has been reached with chromium [4, 5], erbium [6, 7], and dysprosium [8, 9]. Although simpler than molecules, their dipolar interactions are limited by the magnetic moment of atoms and typically requires tuning the short-range interactions to be weaker than the dipole interaction to observe their effects \*\* cite \*\*. \*\* There's also been a recent proposal for creating ultracold dysprosium atoms which exhibit an electric dipole moment in addition to the magnetic dipole moment [10]. \*\*

**Rydberg states** Highly excited Rydberg states of atoms (and molecules) with principal quantum number  $n \gg 1$  can also exhibit strong dipole interactions \*\* [11] \*\*. \*\* Many of the relevant scales scale with  $n$ . \*\* The advantage of Rydberg atoms is that they permit the use of well-established techniques for producing quantum degenerate gases of atoms so that their interactions can be readily incorporated to existing setups. \*\* (Justify/clarify) The Rydberg-Rydberg interactions can also be very strong, much stronger than the magnetic dipole-dipole interaction in dysprosium. The Rydberg dipole-dipole interaction also provide tunability where both the strength and sign of the interaction can be chosen based  $n$ . The major drawbacks are the sensitivities to stray electric fields due to the high- $n$  necessary for achieving strong interactions and Rydberg lifetimes due to both blackbody and Rydberg-Rydberg interactions. Rydberg interactions can be (nearly) isotropic with  $S$ -states ( $L = 0$ ) or anisotropic with  $L > 0$  states \*\* add refs \*\*. Rydberg excitations have even been observed in solid state systems [12].

Our experiment pursues the latter by studying strontium Rydberg atoms. Building on the expertise at Rice for producing ultracold and quantum degenerate strontium of the Killian lab and the creation, control, and detection of Rydberg atoms in the Dunning lab, our experiment melds the expertise of both groups.

## 1.2 Strontium Rydberg Atoms

Compared to other work in ultracold and quantum degenerate Rydberg systems (primarily Rb and Cs with a growing interest in K), strontium offers some nice advantages over the alkalis.

\*\*\*\*\*

The work in this thesis was done with the alkaline earth metal atom strontium. Being a Group II element, it has two valence electrons around a closed shell which gives it some nice properties regarding laser cooling and spectroscopy: -Ground-state has no/very weak magnetic moment - We don't have Feshbach resonances like the alkalis do but it's also relatively insensitive to magnetic fields.  $-^{87}\text{Sr}$  has a large ( $I = 9/2$ ) nuclear spin, making it interesting for \*\* INSERT REASONS \*\*. -The narrow intercombination line at 689 nm provides a really nice transition for performing spectroscopy and laser cooling. Simon Stellmer has a nice writeup of the history of strontium in his PhD thesis [13].

## 1.3 Rydberg Dressing

Our experiment was originally built to pursue Rydberg dressing where atomic interactions are modified by incorporating strongly interacting Rydberg states [14, 15]. After work by our group [16–18], the Pfau group [19] \*\* CHECK IF CORRECT PFAU PAPER \*\*, and the Porto group [20, 21] found that Rydberg dressing was lossy, we moved on to other things.

too colloquial

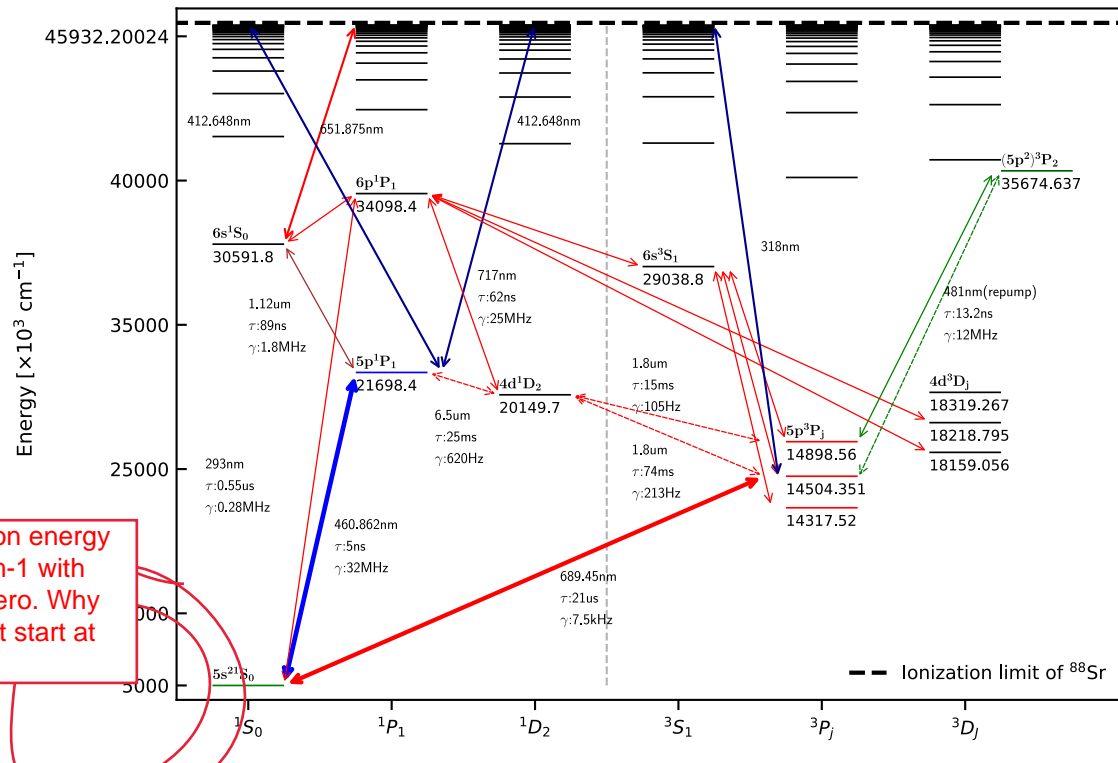


Figure 1.1: Grotrian diagram for (bosonic) strontium ( $^{88}\text{Sr}$  in particular).

## 1.4 Long-Range Interactions

A lot of recent interest in Rydberg atoms (and long-range interactions in general) has been from quantum computing \*\* cite DeMille paper? \*\* where these can be used to entangle gates.

DeMille paper is the proposal for molecular QC. The Lukin/Cote/Zoller PRL paper on fast quantum gates is usually the reference here.

Our experiment has a more fundamental focus on these studies. We don't use the dipole interaction, but instead use the "orbiting" Rydberg electron to probe correlations in quantum gases.

## 2. Strontium Rydberg Experiment

---

This chapter describes the Rydberg apparatus used in this work. It provides documentation of the current state of various systems for producing ultracold and quantum degenerate gases of strontium. Being the third **ultracold strontium at Rice**, we were able to leverage lessons learned **from** the previous experiments (generally referred to as “Neutral” and “Plasma”) to build **quite** a capable and flexible system.

Although most of our system looks very similar to other ultracold strontium systems, what makes our system different is the inclusion of systems for creating, manipulating, and detecting charged particles. In particular, we have in-vacuum electric field plates to cancel stray electric fields as well as ramp to ionizing fields which direct electrons or ions towards the microchannel plate (MCP) detector.

too colloquial

ur old-school “metal can” setup can’t compete with the optical access provided by many recently started alkaline-earth Rydberg tweezer systems using glass cells [22–24].

There’s still a place for our system which likely provides capabilities for better shielding from stray electric fields, performing SFI, and the ability to detect charged particles which, without going to significantly custom systems, are somewhat limiting on the standard glass cell setups.

Our experiment  
is world  
class....not  
needing  
apology that  
"there's still a  
place for our  
system..."

### 2.1 Producing Cold and Ultracold Gases of Strontium

We follow the standard laser cooling and trapping sequence for producing cold and ultracold gases of strontium. Detailed explanations of the techniques are available from various sources (e.g., [13, 25–29]) so the process will only be outlined here for context.

### 2.1.1 Pre-cooling on the 461 nm Transition

Due to strontium's low vapor pressure, an oven is required to sublime strontium into a gaseous form. Our strontium oven operates at about 425 °C with the nozzle at about 390 °C<sup>1</sup>. Other strontium experiments typically run their ovens between (450 – 650) °C<sup>2</sup> so we have some headroom to increase the oven temperature and increase the strontium flux<sup>3</sup>. See section 2.2.1 for more details about our strontium oven.

Immediately after the atoms exit the oven, they pass through the two-dimensional (2D) collimator stage which applies transverse optical molasses [34–38] to reduce the divergence of the atomic beam. The 461 nm ( $5s^2$ )  $^1S_0 \rightarrow (5s5p)$   $^1P_1$  transition is used because of the large  $\Gamma/2\pi = 30.5$  MHz linewidth. Some experiments have incorporated a 2D magneto-optical trap (MOT) which can not only focus the atomic beam but can also deflect the atoms so that only cold atoms enter the experiment region [39]<sup>4</sup>. In order to maximize the efficiency of the 2D collimator, elliptical beams are used to increase the intensity along the atomic beam.

Since the 2D collimator has no effect on the longitudinal velocity, the atoms are still moving at about  $v_{\text{avg}} \approx \boxed{500}^{-15}$ , much too quickly to be trapped by a MOT operating on the 461 nm transition which has a capture velocity of about  $v_C \approx 14 \text{ m s}^{-1}$  [44, 45]. The atoms are slowed longitudinally with a Zeeman slower where a spatially-varying magnetic field keeps the atoms in resonance with a 461 nm beam counterpropagating their direction of travel [46]. Because the magnetic field is axial, a circularly polarized 461 nm beam is

---

<sup>1</sup>Ideally the nozzle should be hotter than the oven to reduce the chances of clogging but it's likely that our actual oven temperature is a bit lower due to the temperature sensor being buried in the oven's heating element rather than in the oven itself.

<sup>2</sup>450 °C [30], 500 °C [31], 575 °C (body) and 850 °C (nozzle) [25, 32], 600 °C (reservoir) and 650 °C (nozzle) [29, 33], (600 – 750) °C [13, 26].

<sup>3</sup>Although this could possibly degrade our trap lifetime.

<sup>4</sup>The designs presented in [40–43] are probably the more “traditional” 2D MOT which forms a cold line of atoms which are then “pushed” to the main chamber.

<sup>5</sup>Assuming the atomic beam leaves the oven at  $T = 425$  °C:  $v_{\text{mp}} \approx 445 \text{ m s}^{-1}$ ,  $v_{\text{avg}} \approx 483 \text{ m s}^{-1}$ , and  $v_{\text{rms}} \approx 514 \text{ m s}^{-1}$  [44].

<sup>6</sup>The capture velocity defined as  $v_C \equiv \Gamma/k$  where  $\Gamma$  is the transition linewidth and  $k$  is the transition wavevector [44].

used. The atoms scatter about \*\* xxx photons \*\* which means they exit the Zeeman slower at about \*\* xxx m/s \*\*. Atoms moving faster than the \*\* design velocity of the Zeeman slower \*\* remain unaffected and continue through without being slowed.

\*\*\*\*\*

Isotope shift of the 461 nm transition.

Table 2.1: Isotope shifts of the 461 nm  $(5s^2)^1S_0 \rightarrow (5s5p)^1P_1$  transition relative to  $^{88}\text{Sr}$ . Due to the hyperfine structure of  $^{87}\text{Sr}$ , the isotope shift is given relative to the center-of-gravity of the upper  $(5s5p)^1P_1$  state. Transitions to a specific  $(5s5p)^1P_1, F$  state can be calculated with the  $A$  and  $B$  hyperfine constants in Tab. 2.2.

Isotope	Lower level	Upper level	$\nu - \nu_{88}$ [MHz]	Ref.
$^{88}\text{Sr}$	$(5s^2)^1S_0$	$(5s5p)^1P_1$	0	
$^{87}\text{Sr}$	$(5s^2)^1S_0$	$(5s5p)^1P_1$	-46.3(20)	[47]
			-49.2(36)	[48]
			-44.6(4)	[49]
$^{86}\text{Sr}$	$(5s^2)^1S_0$	$(5s5p)^1P_1$	-124.8(3)	[47]
			-124.5(13)	[48]
			-126.3(2)	[49]
$^{84}\text{Sr}$	$(5s^2)^1S_0$	$(5s5p)^1P_1$	-270.8(14)	[47]
			-270.6(24)	[48]
			-273.2(3)	[49]

Table 2.2:  $^{87}\text{Sr}$  hyperfine  $A$  and  $B$  coefficients for the  $(5s5p)^1P_1$  state and calculated shifts from the center-of-gravity.

$A$ [MHz]	$B$ [MHz]	Ref.	Lower level	Upper level	$\Delta E_{HF}$ [MHz]
-3.4(4)	39(4)	[50]	$(5s^2)^1S_0, F = 9/2$	$(5s5p)^1P_1, F = 7/2$	36.6(29)
				$(5s5p)^1P_1, F = 11/2$	-5.5(21)
				$(5s5p)^1P_1, F = 9/2$	-22.6(27)
-3.334(25)	40.29(21)	[49]	$(5s^2)^1S_0, F = 9/2$	$(5s5p)^1P_1, F = 7/2$	36.80(17)
				$(5s5p)^1P_1, F = 11/2$	-4.93(12)
				$(5s5p)^1P_1, F = 9/2$	-23.53(14)

### 2.1.2 461 nm “Blue” MOT and Magnetic Trap

Now that a significant portion of the atoms have been slowed by the Zeeman slower, they enter the main chamber where they are cooled and trapped by a standard six-beam 461 nm “blue” MOT. The MOT uses a quadrupole magnetic field and light detuned below atomic resonance to provide both position-dependent and velocity-dependent forces [that] captures and cools the atoms [44, 51, 52]. Our blue MOT typically produces samples of atoms around (1 – 2) mK. Some experiments (e.g., [29]) implement a “cold MOT” stage where detuning, intensity, and quadrupole gradient are ramped during the repumping process to obtain colder temperatures for the red MOT but we found that our temperatures are sufficient for decent transfer to the red MOT.

almost always....if there is no comma, use 'that'. If there is a comma, use 'which'. The actual rule is not so hard. When qualifying an object, if you are distinguishing between a particular example of that object and other examples of that object, use 'that.' If you are providing extra description but not trying to distinguish, use a comma and 'which'. Sometimes, either will work without changing the meaning, but sometimes one or the other significantly changes the meaning of the sentence.

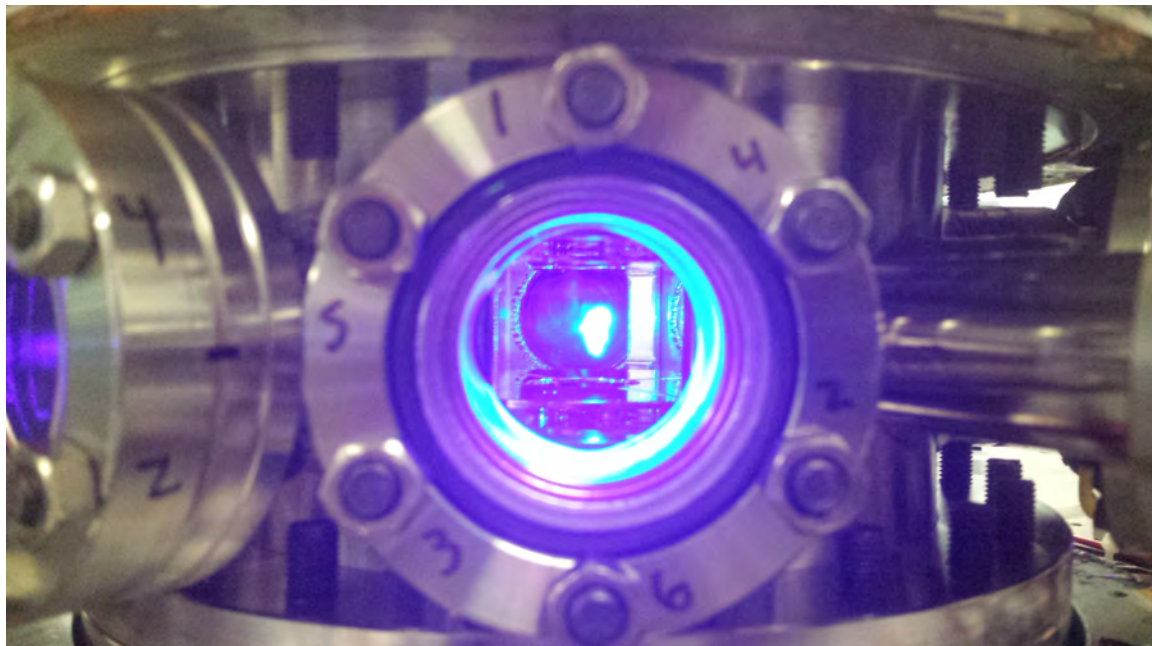


Figure 2.1: An early picture of our  $^{88}\text{Sr}$  blue MOT taken on 2014/08/29 through a 2.75 in viewport with the atom source and Zeeman slower are off to the right. Considering the electric field plates are separated by about 1 in, this blue MOT is likely has a diameter of about 0.5 in. A video is available at <https://youtu.be/ENDIizrlqMA>.

light

Although the 461 nm is capable of scattering many photons per second, the Doppler

limit of this transition is about  $T_D = 732 \mu\text{K}$ <sup>7</sup> [44]. Although sub-Doppler cooling is not available in the bosonic ~~temperature~~ to the lack of hyperfine structure, it has been observed in <sup>87</sup>Sr where the blue MOT was measured to be about 300  $\mu\text{K}$  [53, 54]. Interestingly, as noted in [53], cooling bosonic alkaline-earth atoms on the  $^1S_0 \rightarrow ^1P_1$  transition always seem typically yields temperatures of a few times the Doppler cooling limit until the intensity is close to zero [54–56].

• The  $^1S_0 \rightarrow ^1P_1$  transition is not completely closed with about 1:50 000 decays following the  $(5s5p) ^1P_1 \rightarrow (5s4d) ^1D_2$  decay path. About 2/3 then decay to the  $(5s5p) ^3P_1$  which then decays to the  $(5s^2) ^1S_0$  and return to the 461 nm cooling cycle. The remaining 1/3 decay to the long-lived metastable  $(5s5p) ^3P_2$  states with lifetimes of about 520 s [57], effectively removing them from the blue MOT cooling cycle. Of the  $(5s5p) ^3P_2$  states, the low-field seeking  $m_J = 1, 2$  states can become trapped in the quadrupole magnetic field of the blue MOT. This decay path, initially seen as a loss from the blue MOT, ends up being a powerful tool for accumulating atoms in metastable reservoir [58] at roughly the same temperature as the blue MOT. The magnetic trap was an essential tool in overcoming the abysmal 0.56(2) % natural abundance of <sup>84</sup>Sr to produce the first strontium BECs [59, 60].

use the latest number from the Endres paper and reference the paper.

\*\* For details of our magnetic trap, see [45]. \*\* The magnetic trap is also essential when loading multiple isotopes. Since the isotope shift of the 461 nm transition are comparable to the linewidth, it's difficult to simultaneously laser cool multiple isotopes with this transition. Trapping multiple isotopes is achieved through by sequentially operating a blue MOT tuned to different isotopes which loads the magnetic trap with the specific isotope before tuning the laser to another trap another isotope.

returned to the ground state.

Before moving on to the next cooling stage, atoms in the magnetic trap need to be recovered. Several transitions have been explored for repumping atoms out of the metastable reservoir over the years ([13] gives excellent descriptions in his thesis): \*\* I don't know if I want to keep the list below since it's very similar to one in Simon Stellmer's thesis \*\*

- $(5s6s) ^3S_1$  at 707 nm – this is a popular transition and is used by a lot of past and

<sup>7</sup>For the 461 nm transition:  $k_B T_D \equiv \hbar \Gamma / 2 = 732 \mu\text{K}$ ,  $k_B T_r \equiv \hbar^2 k^2 / 2M = 512 \text{nK}$ .

current strontium experiments [22, 23, 25, 31, 32, 61, 62] since it's well characterized and easily accessible with available laser diodes. The drawback is that this upper state is  $J = 1$  meaning  $(5s6s)^3S_1$  can decay to the metastable  $(5s5p)^3P_0$  state as well, requiring another laser at 679 nm to repump out of this state.

- $(5s4d)^3D_2$  – at 3011.84 nm driving the  $(5s5p)^3P_2 \rightarrow (5s4d)^3D_2$  [63] transition. Being a  $J = 2$  state means a single laser can be used to clear out the  $(5s5p)^3P_2$  reservoir but the 3  $\mu\text{m}$  wavelength is difficult to produce.
- $(5s5d)^3D_2$  – at 496.93 nm driving the  $(5s5p)^3P_2 \rightarrow (5s5d)^3D_2$  transition [13, 64, 65]. The challenge of using this transition is the difficulty in producing the green repumping light which typically requires frequency doubling (e.g., [66]).
- $(5s6d)^3D_{1,2}$  – at 403.35 nm driving the  $(5s5p)^3P_2 \rightarrow (5s6d)^3D_2$  transition [64, 65]. Similar attributes as using the  $(5s5d)^3D_2$  with the added advantage of being accessible with Blu-ray laser diodes.
- $(5p^2)^3P_{1,2}$  – at 481.323 nm driving the  $(5s5p)^3P_2 \rightarrow (5p^2)^3P_2$  transition [45, 67–70].

On our experiment, we use the 481 nm transition.

### 2.1.3 689 nm “Red” MOT

After repumping, we further cool the sample by operating a MOT on the narrow ( $\Gamma/2\pi = 7.5 \text{ kHz}$ )  $(5s^2)^1S_0 \rightarrow (5s5p)^3P_1$  transition at 689 nm which has a Doppler limit of  $T_D = 180 \text{ nK}$  and recoil limit of  $T_r = 229 \text{ nK}$ . Following [71], MOTs can be characterized by the ratio of the transition linewidth ( $\Gamma$ ) to the single photon recoil frequency shift ( $\omega_R$ ) with typical MOTs operating in the regime  $\Gamma/\omega_R \gg 1$  compared to narrow line MOTs where  $\Gamma/\omega_R \sim 1$ . Operating in the  $\Gamma/\omega_R \sim 1$  regime where a few photon recoils can kick an atom out of resonance with the cooling lasers leads to very different dynamics. The differences in dynamics are especially apparent in the shape of the bosonic red MOTs \*\*

FIGURE? \*\*. The fermionic red MOT may look similar to a  $\Gamma/\omega_R \gg 1$  MOT but it's shape is due to complications arising from hyperfine structure. An excellent description of how the narrow 689 nm “red” MOT works for both the bosons and fermion is presented in [13]<sup>8</sup> with additional resources in [25, 72].

Considering first the bosonic case, the  $\Gamma/2\pi = 7.5$  kHz transition is a bit too narrow to effectively capture the  $\sim 2$  mK atoms from the blue MOT. In order to increase the transfer efficiency, the spectrum of the red MOT light is artificially broadened by frequency modulation, typically a few megahertz, which can be somewhat thought of as making the transition linewidth broader. Once enough atoms have been captured in the “broadband” red MOT, the frequency modulation and intensity is ramped down<sup>9</sup> to a narrow or single-frequency red MOT where the coldest temperatures are achieved.

While the bosonic isotopes of strontium behave like an ideal  $J = 0 \rightarrow J = 1$  MOT as described in texts (e.g., [44, 52]) and are relatively straightforward to cool to sub-2  $\mu$ K temperatures, the hyperfine structure of  $^{87}\text{Sr}$  poses a unique challenge. Since the ground state has (essentially) no magnetic moment, the position-dependent Zeeman shift is only experienced by the upper state but this results in the both a restoring force for some positions and transitions and an anti-trapping force for other transitions and positions. Narrow line laser cooling of  $^7\text{Sr}$  was first achieved by the Tokyo group <sup>through the use of</sup> a “trap” laser resonant with the  $(5s^2)^1S_0, F = 9/2 \rightarrow (5s5p)^3P_1, F = 11/2$  transition and a second “stir” laser resonance with  $(5s^2)^1S_0, F = 9/2 \rightarrow (5s5p)^3P_1, F = 9/2$  to quickly redistribute the population and take advantage of the Clebsch-Gordan coefficients so that, on-average, the atoms experience a restoring force [13, 73].

\*\*\*\* An alternative method, Saw-tooth Wave Adiabatic Passage (SWAP) cooling, was recently developed which avoids the need for the traditional broadband red MOT in favor of a carefully designed frequency ramps <sup>that</sup> adiabatically move atoms between the  $^1S_0$  and

---

<sup>8</sup>Generally referred to as the “Red MOT Bible”.

<sup>9</sup>Reducing the frequency modulation essentially increases the intensity of each comb tooth in the FM spectrum.

$^3P_1$  states [74–77]. The advantage of this method is particularly apparent for  $^{87}\text{Sr}$  which eliminates the need for the “stir” laser. The drawback is that the temperatures achieved seem to be limited to about  $10\ \mu\text{K}$  due to the need to maintain an efficient adiabatic transfer [74] so the current scheme is to use SWAP cooling instead of the broadband red MOT before transferring to a single-frequency red MOT to reach colder temperatures [78]. \*\*\*

Due to the large isotope shifts compared to the  $7.5\ \text{kHz}$  linewidth of the transition, multiple red MOTs can be operated simultaneously for multiple isotope. After laser cooling on the  $689\ \text{nm}$  transition, our sample temperatures are typically  $\sim (1 - 2)\ \mu\text{K}$ , which is sufficient for loading into an optical dipole trap (ODT).

#### 2.1.4 Optical Dipole Trap

Strontium in the  $(5s^2)^1S_0$  ground state has no magnetic moment meaning it cannot be magnetically trapped<sup>10</sup> meaning optical dipole traps (ODTs) are required.

and  
\*\*\*\* Work through details of this derivation! \*\*\*\* no....don't rederive the standard formula.

Following the derivation in [32] with more details in ??, we start by considering a two-level atom with states  $|g\rangle$  and  $|e\rangle$  separated by energy  $\hbar\omega_0$ . Applying an off-resonant laser with frequency  $\omega_L$  field couples these two states which shifts their energy levels by

$$\Delta E = -\frac{E_0^2}{4} \left( \frac{2|d|^2}{\hbar} \frac{\omega_0}{\omega_0^2 - \omega_L^2} \right) = -\frac{E_0^2}{4} \alpha(\omega_L) \quad (2.1)$$

where  $\alpha(\omega_L)$  is the (dipole) polarizability and  $d \equiv \langle g | \vec{d} | e \rangle$  is the dipole matrix element. A simple generalization to a multi-level atom is relatively straightforward by summing the contributions for other levels. The resulting polarizability can be written as

$$\alpha_g(\omega_L) = \frac{2}{\hbar} \sum_e |d_{ge}|^2 \frac{\omega_{ge}}{\omega_{ge}^2 - \omega_L^2} \quad (2.2)$$

Here,  $g$  doesn't necessarily need to be the ground state. Spatial confinement is achieved by considering  $I = c\epsilon_0 E_0^2/2$  so by designing a spatially-varying intensity  $I(\vec{r})$ . \*\*\* FIX

<sup>10</sup>There is some interest in producing quantum degenerate gases of alkaline-earth atoms in metastable states some of which are magnetically trappable (e.g., the  $(5s5p)^3P_2$ ) [79]. Quantum degenerate gases of metastable atoms have been realized for helium [80–82].

EQUATION \*\*\*

$$\alpha_g(\omega_L) = \frac{2}{\hbar} \sum_e |d_{ge}|^2 \frac{\omega_{ge}}{\omega_{ge}^2 - \omega_L^2} \quad (2.3)$$

\*\*\* FIX EQUATION \*\*\*

For strontium, the red MOT spatial distribution and the particular isotope(s) being loaded needs to be taken in to account when designing an ODT. While the fermionic red MOT traps atoms in an ellipsoidal volume around the quadrupole zero, the atoms in a bosonic red MOT form a thin shell below the quadrupole center [26, 72]. As a result, improved loading of atoms in to an ODT can be obtained by “mode-matching” the trapping volume of the ODT to better match the spatial distribution of atoms in the red MOT. The preferred ODT geometry appears to be a high-aspect ratio horizontal “pancake” or “light sheet” where the tight axis is along gravity as this matches well with the red MOT shape. Our main trap is currently a single “sheet” beam with waist sizes of about \*\* 26  $\mu\text{m}$   $\times$  260  $\mu\text{m}$

\*\*<sup>11</sup>

The specific isotope(s) being worked with also have an effect on both loading in to an ODT as well as the evaporation due to their wildly varying intra- and inter-isotope scattering lengths (see Tab. 2.3). The first strontium BECs were achieved with <sup>84</sup>Sr, which has an ideal

Table 2.3: Measured *s*-wave scattering lengths of strontium.

Isotope	[85]	[86]	[87]
<sup>88</sup> Sr- <sup>88</sup> Sr	-1.4(6)	-2.00(27)	
<sup>87</sup> Sr- <sup>87</sup> Sr	96.2(1)	96.198(68)	
<sup>86</sup> Sr- <sup>86</sup> Sr	823(24)	798(12)	810.6(3)(9)
<sup>84</sup> Sr- <sup>84</sup> Sr	122.7(3)	122.762(92)	
<sup>88</sup> Sr- <sup>87</sup> Sr	55.0(2)	54.819(92)	
<sup>88</sup> Sr- <sup>86</sup> Sr	97.4(1)	97.374(69)	
<sup>88</sup> Sr- <sup>84</sup> Sr	1790(130)	1658(54)	
<sup>87</sup> Sr- <sup>86</sup> Sr	162.5(5)	162.25(21)	
<sup>87</sup> Sr- <sup>84</sup> Sr	-56(1)	-57.61(61)	
<sup>86</sup> Sr- <sup>84</sup> Sr	31.9(3)	31.65(14)	

scattering length  $a = 123 a_0$  [86] and was easily evaporated to quantum degeneracy in low-

<sup>11</sup>Some traps used by other groups: 18  $\mu\text{m}$   $\times$  250  $\mu\text{m}$  [26]; 22.8  $\mu\text{m}$   $\times$  228  $\mu\text{m}$  and 16  $\mu\text{m}$   $\times$  270  $\mu\text{m}$  [29, 83]; 17  $\mu\text{m}$   $\times$  340  $\mu\text{m}$  [31, 84].

aspect ratio traps [59, 60]. An unpolarized degenerate Fermi gas of  $^{87}\text{Sr}$  was also obtained in a nearly-circular ODT [88] but spin-polarized degenerate Fermi gases requires sympathetic cooling [26]. Early work towards producing quantum degenerate gases of  $^{88}\text{Sr}$  and  $^{86}\text{Sr}$  were hindered by the tight waists [89, 90] which leads to inelastic losses of  $^{86}\text{Sr}$ . Only by going to a large-volume high-aspect ratio ODT was a BEC of  $^{86}\text{Sr}$  realized [91]. The first BEC of  $^{88}\text{Sr}$  was achieved by sympathetic cooling with  $^{87}\text{Sr}$  [92].

Some recent work towards developing systems for trapping strontium in optical tweezer arrays showed results that an ODT around  $(501 - 520)$  °C is close to a “magic” wavelength<sup>12</sup> for the  $(5s^2)^1S_0 \rightarrow (5s5p)^3P_1$  transition [22, 23]. It should be noted that both our current 1064 nm ODT and a ‘green’ ODT are both expected to be repulsive for Rydberg states [95, 96] for strontium Rydberg states.

## 2.2 Vacuum System

An overview of our vacuum system is shown in Fig. 2.2 and follows the cooling stages described above. Perhaps the most noticeable aspect of our vacuum system is that it was designed to have the majority of the horizontal laser beams 3.5 in = 8.89 cm from the surface of the optical table. Keeping most of the beams at this fixed height significantly reduced the need for rigid supporting structures to elevate both the entire vacuum system as well as the various platforms for optics. This also diminished the need for periscopes to elevate laser beams from the table to the height of an elevated vacuum chamber<sup>13</sup>.

To facilitate vertically propagating beams, two holes were cut through the table: a semicircle for the vertical 2D collimator arm and a 10 in diameter circle under the main chamber. We had originally planned on mounting vertical optics directly to the main chamber but decided instead to mount them to a single elevated platform above the main

---

<sup>12</sup>A wavelength is “magic” when two states experience the same shift (i.e., no differential shift) [93, 94].

<sup>13</sup>Fiber-coupling all the laser beams is a potential alternative to avoiding periscopes but that includes some unavoidable loss in power and some wavelengths (i.e., the 320 nm UV laser) would be difficult fiber couple at the present time.

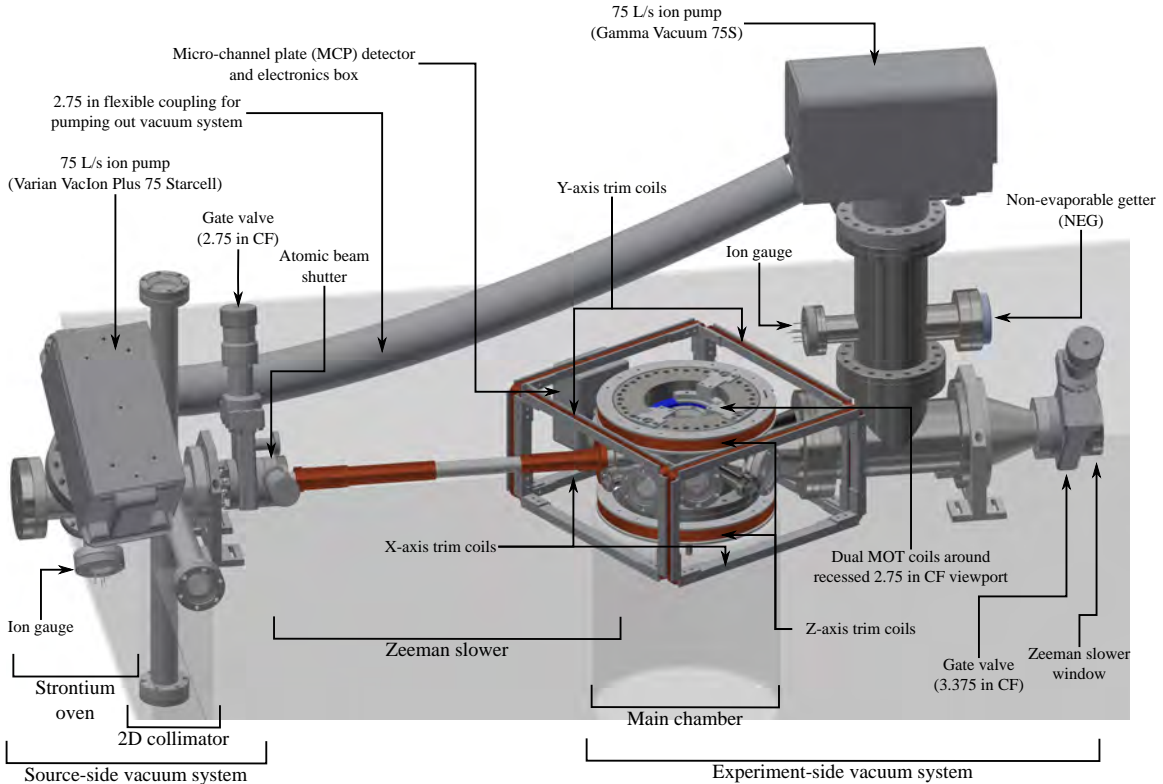


Figure 2.2: Overview of the strontium Rydberg apparatus highlighting the main sections of the vacuum system and various components.

chamber and another platform on the underside of the table. This should reduce sensitivity to vibrations as the main chamber is (almost) “free-floating” from the optics mounted to the table. Adding the breadboard under the table required tapping 1/4"-20 threads on the underside of the table. The major disadvantage of our current setup is the long distance between the undertable breadboard and the bottom of the main chamber which is about 12 in<sup>14</sup> which makes it difficult to design, install, and align sensitive vertical beams.

### 2.2.1 Source-side Vacuum System

This section of the vacuum chamber is where strontium oven and 2D collimator are located. Although there are now various designs for strontium ovens [30, 97], and even commercial systems from AO Sense, we used a design which has shown success in the

<sup>14</sup>The thickness of the optical table.

that

Killian lab. It's a simple design where a Watlow FIREROD cartridge heater<sup>15</sup> provides the majority of the heating power to the atomic oven. An array of capillary tubes forms a nozzle to provide some degree of collimation and resistive heater wire is wrapped around them to reduce the effects of strontium building up in the capillary tubes and clogging. We typically run our main FIREROD oven heater around 425 °C<sup>16</sup> with the nozzle heater wire around 390 °C. Figure 2.3 shows a similar oven made to replace the Neutral's strontium oven and is very similar to the one on our setup but it was mounted on the much smaller 2.75 in flange whereas ours is mounted on a 3.375 in flange which provides some extra room for various feedthroughs without being too cramped.



Figure 2.3: Neutral's new strontium oven during construction before thermocouple and nozzle heating wire have been attached. The design is very similar to our oven but is mounted on a 2-3/4 in CF flange instead of a 3-3/8 in CF flange as on our experiment. (Left) Oven without heat shield. (Right) After adding heat shield.

After atoms exit the oven, they pass through a two-dimensional (2D) collimator which applies transverse optical molasses [36, 37, 98] to increase the flux of atoms down the Zeeman slower. The long arms of the 2D collimator help prevent strontium buildup on the

---

<sup>15</sup>These are neat little devices which come with leads for both the resistive heating element and an integrated thermocouple.

<sup>16</sup>Note that the FIREROD temperature sensor is inside the ceramic body whereas the nozzle thermocouple is attached to the nozzle itself.

AR coated viewports.

describe the  
tube ...length, width,  
construction...

Before the atoms leave this section of the vacuum system ~~and enter the Zeeman slower,~~ the pass through a small differential pumping tube ( $C \approx 0.85 \text{ L s}^{-1}$ ) which helps maintain the pressure differential between the source and experiment sides of the system. The pressure in the source side is typically higher than the experiment side and is around  $7.6 \times 10^{-9} \text{ Torr}$ <sup>17</sup>. We suspect the ion pump on the source side is being restricted by the zero-length reducer which adapts the 4.5 in flange on the source-side vacuum chamber to the 6 in flange on the Varian ion pump.

A shutter and a gate valve was also installed between the source-side vacuum system and the Zeeman slower. The shutter allows us to physically block the atomic beam ~~since we don't have 2~~ which should extend the time between needing to change the Zeeman slower entrance window. The gate valve should, in principle, allow us to isolate the source-side vacuum system from the rest of the chamber to facilitate reloading the strontium oven without venting the entire vauum chamber but we found this valve to be somewhat leaky when we initially pumped out our system<sup>18</sup>.

### 2.2.2 Zeeman Slower

Since an oven is required to produce enough strontium vapor for trapping, a Zeeman slower is required to slow the atoms down so that they can be captured by the MOT. The Zeeman slower was designed and built by Francisco Camargo and is detailed in his master's thesis [45] so it will only be briefly covered here. Our Zeeman slower uses a spatially-varying axial magnetic field and circularly-polarized light to keep the atoms resonant with a light propagating counter to the direction of the atomic beam so that they continuously scatter photons as they slow [46]. Our particular design is a "spin-flip"-type Zeeman slower where

---

<sup>17</sup> MiniVac ion pump controller outputting  $7.9 \text{ mV} = 7.9 \times 10^{-6} \text{ A}$  for the rebuilt VacIon Plus 75 Starcell on 2019/06/13.

<sup>18</sup> Something similar was noticed by the Weld group at UCSB and they used two gate valves to separate their atomic source from their UHV main chamber [33].

the amplitude of the axial magnetic field crosses zero between the ends.

Our Zeeman slower was custom made with a double wall that acts as a water cooling jacket where the inner wall separates the water from UHV and the outer wall where the <sup>15</sup> magnetic field coils are wrapped. Due to space constraints, the source-side welded to a 2.75 in flange whereas it's connected to the main chamber by a 2.125 in flange. These flanges are also where cooling water enters and exits the jacket. It's possible to avoid water-cooling by using a permanent magnet Zeeman slower [99–102] but the magnetic field would likely require shielding and/or more significant cancellation at in order for it to not interfere with other aspects of the experiment.  
~~cannot be turned off.~~

The Zeeman slower coil was constructed in multiple layers so that subsequent layers can be designed so that the resulting field was matched the desired profile. Each layer was attached to the Zeeman slower with thermally-conductive epoxy<sup>19</sup> and measured before deciding on how to wrap the next layer of windings. Due to our relatively long Zeeman slower ( $C \approx 1.4 \text{ L s}^{-1}$ ), it should provide some additional differential pumping between the source and experiment sides.

### 2.2.3 Experiment-side Vacuum System

The experiment-side vacuum system can be broken down in to the main chamber where experiments take place and a “pumping tower”. The custom main chamber <sup>20</sup> features:

- Recessed top and bottom flanges bring the 2.75 in viewports closer to the center of the chamber while providing room for the MOT coils to fit around the viewport. The in-vacuum electric field plates are mounted to the bottom flange which has eleven 10 kV safe high voltage (SHV) feedthroughs for high-voltage connections.
- Six 2.75 in horizontal viewports provide optical access for the various MOT and optical

<sup>19</sup>Emerson and Cuming STYCAST 2762 or STYCAST 2762 FT with Catalyst 14, 17, or 17M-1.

<sup>20</sup>Fabricated by Huntington Mechanical Labs.

dipole trap beams.

- Three 1.33 in horizontal viewports used for the various 689 nm and 320 nm excitations beams ~~and~~ are oriented perpendicular and parallel to the MCP.
- Room for a Photonis miniTOF micro-channel plate (MCP) detector.
- A conical expansion to a 6 in flange for increased conductance to the pumps.

Most of the viewports were anti-reflection (AR) coated for 461 nm, 689 nm, and 1064 nm (see Fig. 2.4). Vacuum pressure on the experiment-side is maintained by a  $75 \text{ L s}^{-1}$  ion pump<sup>22</sup>

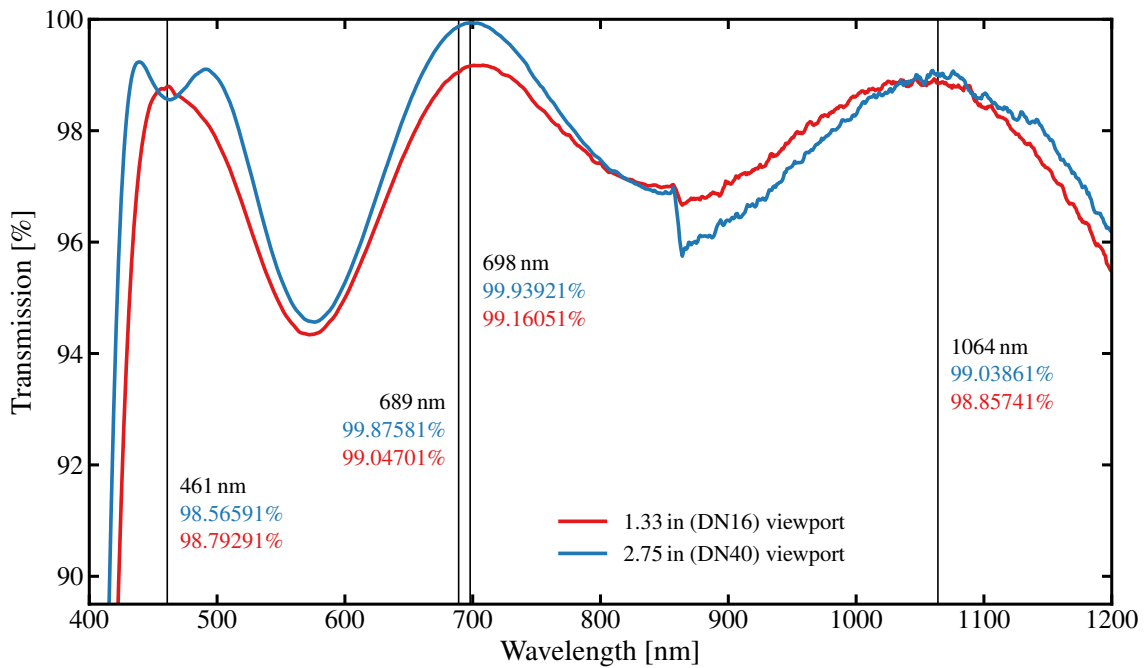


Figure 2.4: Transmission data of the Reynard Corporation<sup>21</sup>anti-reflection (AR) coating on the 1.33 in and 2.75 in viewports from MDC Vacuum Products. It's fortuitous that the AR coating should be very good for 698 nm (clock transition) and reasonable for 532 nm and 813 nm should we ever decide to use traps at those wavelengths.

located at the top of the pumping tower. The ion pump current suggests the vacuum on

---

<sup>21</sup>I would like to thank Robyn Miller at Reynard Corporation for finding and sending me the reflection and transmission data from the order we placed six years ago.

<sup>22</sup>Gamma Vacuum TiTan 75S-CVX-6S-SC-N-N.

this side is about  $3.4 \times 10^{-9}$  Torr<sup>23</sup>. Additional pumping is provided by a non-evaporable getter (NEG)<sup>24</sup> located about halfway up the pumping tower. In retrospect, we should have also included a titanium sublimation pump (TSP) for additional pumping capability.

We also added a 3.375 in gate valve between the Zeeman slower window and main chamber to facilitate changing the ~~sacrificial~~ Zeeman slower entry viewport once it gets coated with strontium<sup>25</sup>.

### 2.3 Magnetic Field Trim Coils

Three pairs of Helmholtz coils are used to cancel stray magnetic fields and to apply a bias field. The “X-axis” and “Y-axis” coil pairs produce fields in the horizontal plane parallel to the table surface and are oriented such that the “X-axis” produce a field towards or away from the MCP whereas the “Y-axis” produces a field perpendicular. The “Z-axis” coils produces a field along the vertical axis perpendicular to the surface of the table.

Both the horizontal (X-axis and Y-axis) trim coils are constructed from 17.5 AWG wire<sup>26</sup> with 45 turns wound on aluminum U-channel and held together with polyimide tape. Due to the choice of keeping the center of the chamber at 3.5 in above the table surface, this required the horizontal (X-axis and Y-axis) trim coils to be centered at this height which required their geometry be rectangular instead of square or circular.

The vertical (Z-axis) coils were ~~wound~~ on circular aluminum U-channel forms and fit around the outside of the top and bottom flanges of the main chamber which allowed us to put many turns on them. The circular U-channels used as the forms also feature a radial slice, filled with epoxy, to mitigate the generation of eddy currents. In retrospect, we should made the horizontal coils beefier (especially along the X-axis) in order generate larger bias

---

<sup>23</sup>MiniVac ion pump controller outputting  $-4.8 \text{ mV} = 4.8 \times 10^{-6} \text{ A}$  for the Gamma Vacuum TiTan 75S on 2019/06/13.

<sup>24</sup>SAES CapaciTorr D 200.

<sup>25</sup>Neutral has tried using Plasma’s pulsed Nd:YAG laser to perform ablation on their coated Zeeman viewport with a moderate level of success.

<sup>26</sup>MWS Wire Industries 17.5 HAPT-200 (NEMA MW 35-C).

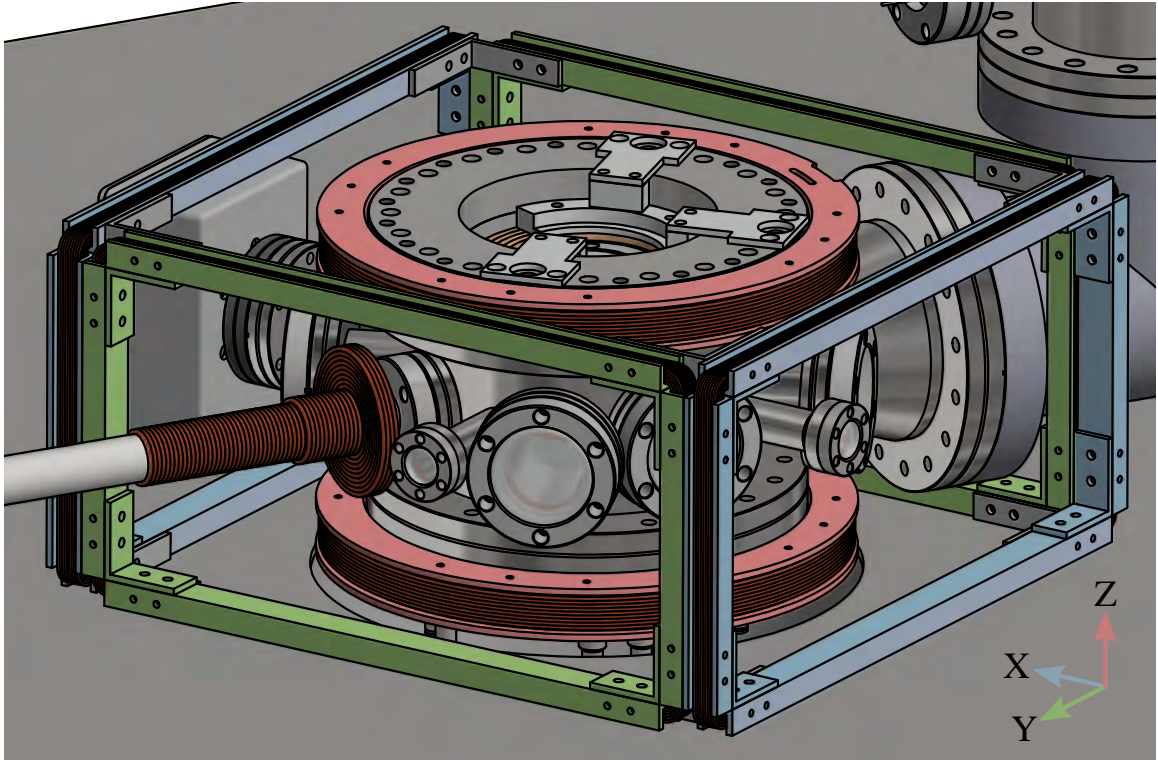


Figure 2.5: Magnetic field trim coils around main chamber for nulling stray fields and/or applying bias fields. The trim coil axes are defined relative to the MCP (equivalently, the 1.33 in viewports for the Rydberg excitation lasers) and gravity with the  $X$ -axis (blue) oriented towards the MCP, the  $Z$ -axis (red) perpendicular to the table surface/gravity, and the  $Y$ -axis (green) perpendicular to the other two axes (following the right-hand rule, of course).

fields along the MCP axis and increase detection efficiency. We found that having bias fields along other directions (i.e., not towards/away from the MCP) reduced our detection efficiency, likely due to the Lorentz force steering electrons away from the MCP.

## 2.4 Dual MOT Coils

One of the things we did differently from the previous strontium experiments is that we have two pairs of MOT coils instead of a single pair (see Fig. 2.6) where the larger pair is used for the blue MOT while the smaller pair for the red MOT. This allows us to use two different current supplies without needing a controller that has the dynamic

range to provide the  $\sim 40$  A to generate the  $\sim 40$  G cm $^{-1}$  field for the blue MOT while also generating a low-noise  $\sim 1$  G cm $^{-1}$  gradient for the red MOT.

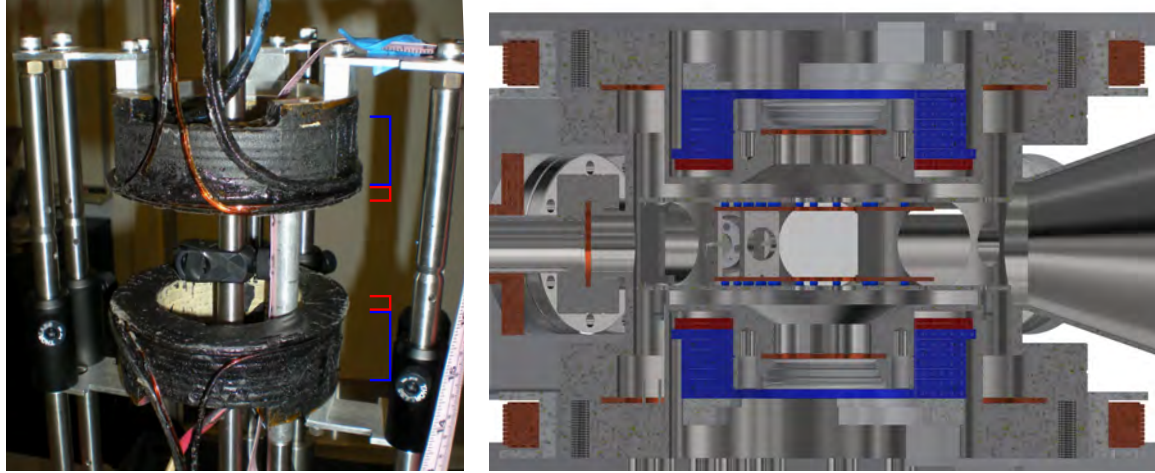


Figure 2.6: (Left) Picture of our assembled dual MOT coils on a test setup. (Right) CAD rendering of how they are centered around the buket windows of the main chamber. \*\* Redo with 2D CAD drawing instead of rendered image. \*\*

The blue MOT coils are made from xxx<sup>27</sup> hollow inside with approximately \*\* \*\* outer dimensions with a hollow \*\* \*\* through the middle for water. We typically run the blue MOT coils with around \*\* 40-50 amps \*\* of current from a fixed power supply \*\* GIVE MODEL \*\*. A \*\* MOSFET \*\* is used to quickly switch off the current to the coils. \*\* We so far haven't included a flyback diode although the MOSFET we use seems to include an internal flyback diode. \*\* These coils produce a magnetic field gradient of about 1.25 G cm $^{-1}$  A $^{-1}$ .

The red MOT coils are constructed from square 13 AWG copper wire<sup>28</sup> and are epoxied to the undersides of the blue MOT coils, placing them closer to the center of the vacuum chamber. We currently use a homebuilt voltage-controlled current driver<sup>29</sup> but we should be able to use any current driver capable of supplying up to about \*\* 5 A \*\*. Our current geometry for the red MOT coils produce a magnetic field gradient of about 1 G cm $^{-1}$  A $^{-1}$ .

<sup>27</sup>S&W Wire 125SQ DPG/BARE (NEMA 46-C).

<sup>28</sup>MWS Wire Industries 13 SQ HML-240 (NEMA MW 20-C).

<sup>29</sup>\*\*Powered by an APEX PA12\*\*.

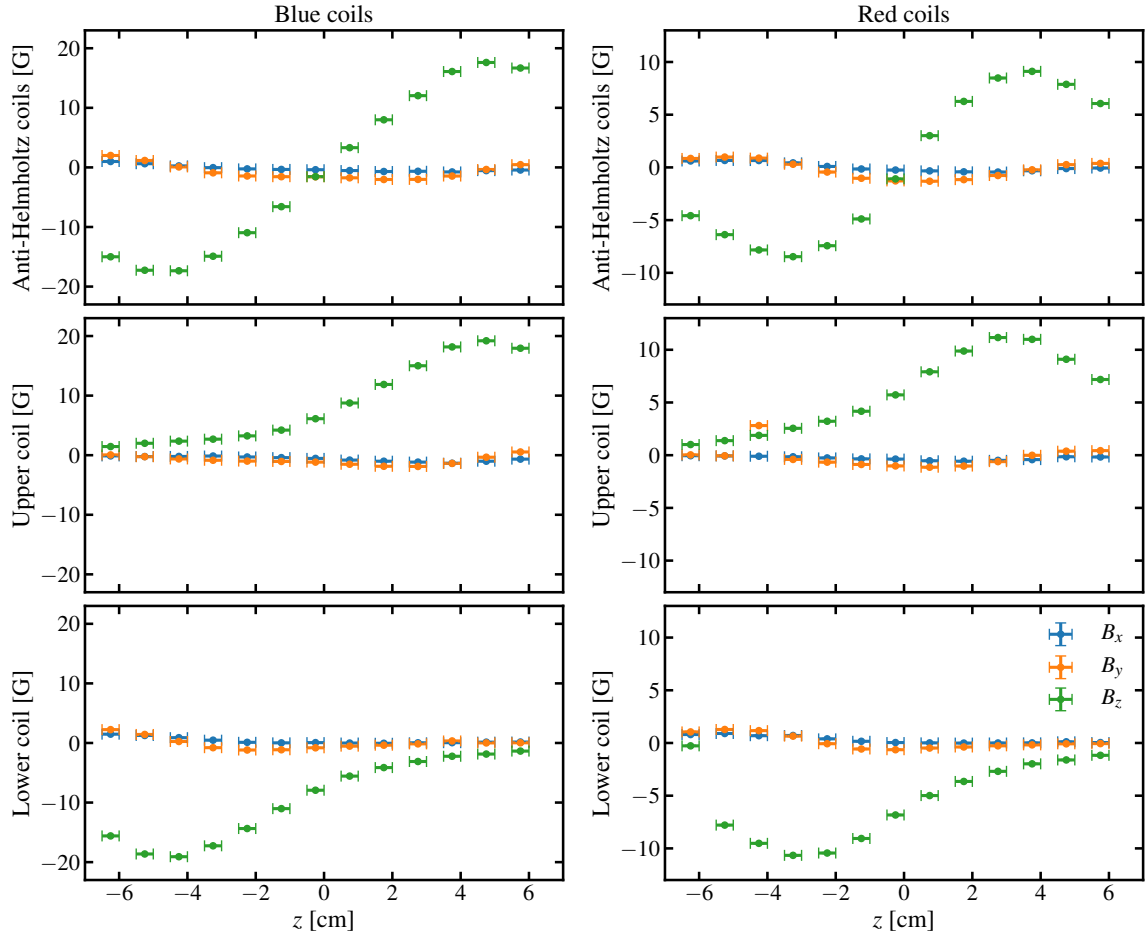


Figure 2.7: Blue MOT coil (left) and red MOT coil (right) magnetic fields measured along the  $z$ -axis on the test setup shown in Fig. 2.6 with  $I = 4$  A. The uncertainties are estimated to be  $\delta_z = \pm 2.5$  cm and  $\delta_B = \pm 0.05$  G. The non-zero measured values of  $B_x$  and  $B_y$  suggest that the probe was slight off the  $z$ -axis. There also appears to be a slight systematic shift in zero-crossing of the anti-Helmholtz coils likely due to an uncertainty in determining the physical center of the coils.

\*\* It would have been nice to have an extra MOSFET switch on the blue MOT coils so that we'd be able to apply extremely large fields along the Z-axis such as e.g. Pedro's experiment Feshbach coils. We're not too worried about not having this capability since ground-state strontium has no magnetic Feshbach resonances and the fact that we've observed a decrease MCP detection efficiency we believe is due to the Lorentz force as the MCP is oriented along the X-axis. \*\*

## 2.5 Laser Systems for Producing Cold and Ultracold Strontium Gases

Figure 2.8 gives an overview of the orientation of our various laser cooling and trapping beams.

### 2.5.1 461 nm “Blue” Laser System

The experiment currently has three blue diode lasers in a master-slave configuration that provides all the 461 nm power available for our experiment. In a master-slave setup, a single (typically low-power) “master” external cavity diode laser (ECDL) is frequency stabilized relative to the atomic transition and is used to injection lock high-power “slave” lasers to amplify the laser power [103, 104].

Our current ECDL master laser<sup>30</sup> outputs about 40 mW and is locked relative to the  $(5s^2)^1S_0 \rightarrow (5s5p)^1P_1$  in a homebuilt strontium saturated absorption cell using Doppler-free saturated absorption spectroscopy. The error signal is obtained by modulating the magnetic field around the saturated absorption cell and using circularly-polarized pump and probe beams. Although this laser tunes relatively well and generally remains single-mode when tuning between the various isotopes, we have been very disappointed with output quality of the laser which has what appears to be a Hermite-Gaussian TEM<sub>00</sub> output mode (\*\*see Fig. XX). \*\* INCLUDE BEAM PROFILER FIGURE \*\* Due to this poor output

---

<sup>30</sup>New Focus TLB-6802: a Littman-Metcalf external cavity diode laser (ECDL).

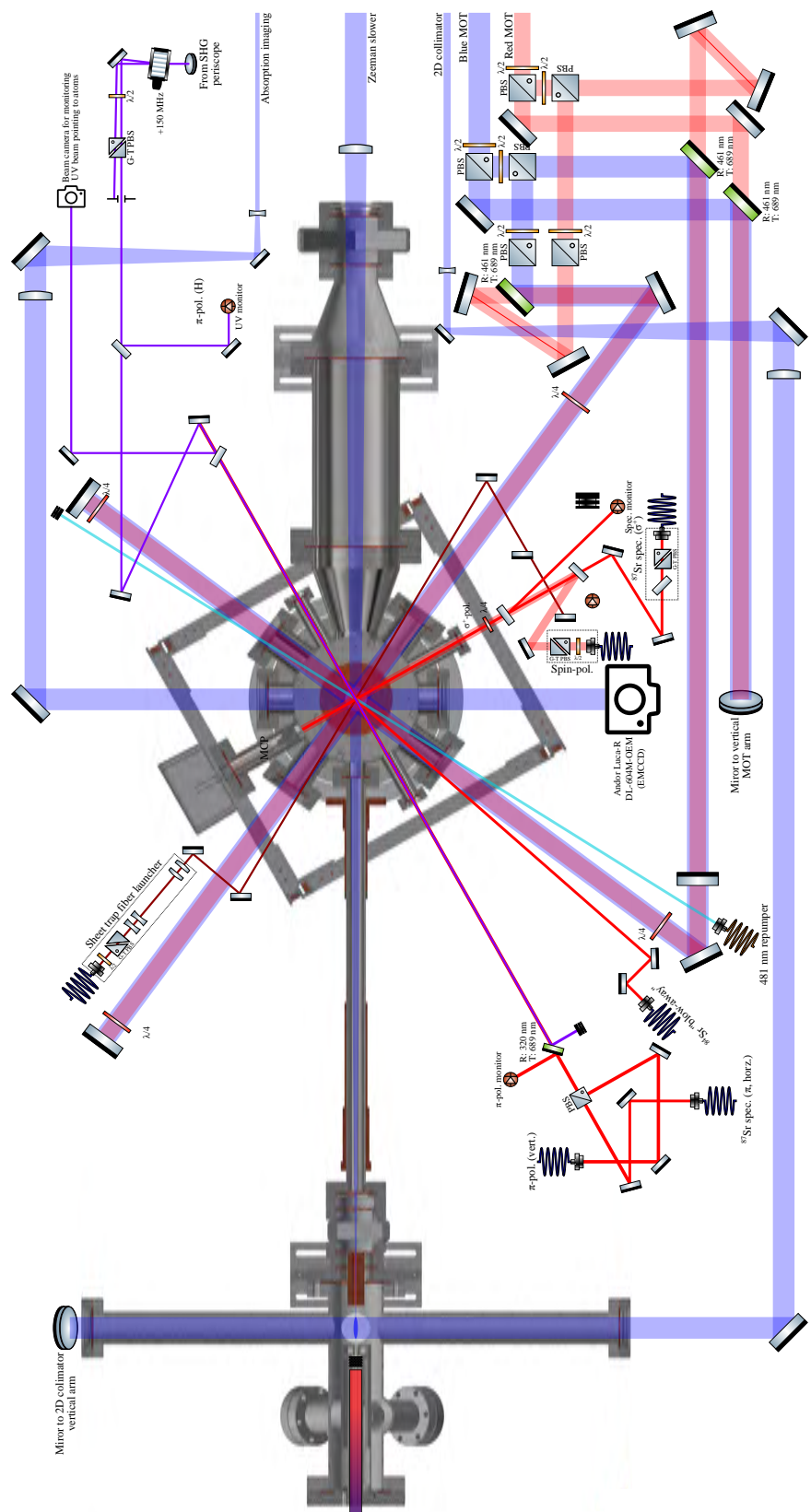


Figure 2.8: Simplified schematic of the various trapping and cooling lasers and the Rydberg excitation beams.

mode, a D-mirror was used to split the beam in to two nearly-Gaussian beams. One of **define the acronym** the beams is directed to a **SMPM** fiber **that** injection locks both our slave lasers whereas

the other is currently unused. After using the laser for about six years, the piezo tuning element died<sup>31</sup> and the laser had to be sent back to New Focus for repairs. During the

repairs, we changed our setup so that the two slave lasers are injection locked from the

**output of a fiber so that we can easily change master lasers should this laser die again.** We also noticed some **weird grounding issues** with the TLB-6700 drivers New Focus sent us

with the lasers<sup>32</sup>. **We also have concerns about the long-term cost-effectiveness and reliability [33] of the New Focus ECDL, and we have purchased a Toptica 461 nm ECDL system [34] as a future replacement and to enable additional experiments.**

Light from the master laser injection locks two slave lasers<sup>35</sup>. We have previously tried homebuilding our own 461 nm slave laser with can-opened blue diode<sup>36</sup> but found it to be unsatisfactory. We ended up going with two New Focus TLB-6802-IJ<sup>37</sup> both of which output about 100 mW of power. The “MOT” slave is injection locked at the same frequency as the master laser and its power is split between the blue MOT, 2D collimator, and the imaging beam. The injection beam for the “Zeeman” slave is first shifted by -535 MHz relative to the master laser before injection locking the laser. This allows all the power out from the slave to be used for operating the Zeeman slower instead of taking a hit going through an AOM.

The entire 461 nm system is housed at far end of our table from the vacuum system and boxed in an opaque enclosure to contain the blue light, even a little of which can lead to

---

<sup>31</sup>The laser died after powering down and keying off the laser driver...

<sup>32</sup>Similar issues were noticed by Jun Ye’s group when I asked them if they have observed issues with the New Focus lasers.

**requires installation of a new diode, even when the existing diode is fine, and the initially quoted**

**cost was 11,500. This was significantly reduced after extended discussions with the company.**

<sup>34</sup>We ended up purchasing a 461 nm ECDL from Toptica but both companies provided quotes for NEW lasers, about 21k from MOGLabs and about 25k from Toptica but with about 100 mW of output power.

<sup>35</sup>New Focus TLB-6802-IJ-D: a gratingless version of the TLB-6802 likely with a higher-power diode as well.

<sup>36</sup>Nichia NDB4216E - a non-AR coated diode with about 100 mW of output power.

<sup>37</sup>From what we can tell, these are simply their standard TLB-6802 without the grating and probably using the Nichia NDB4216E non-AR coated diode which is specified to output about 100 mW.

Describe it  
enough to be  
helpful to  
future  
students.

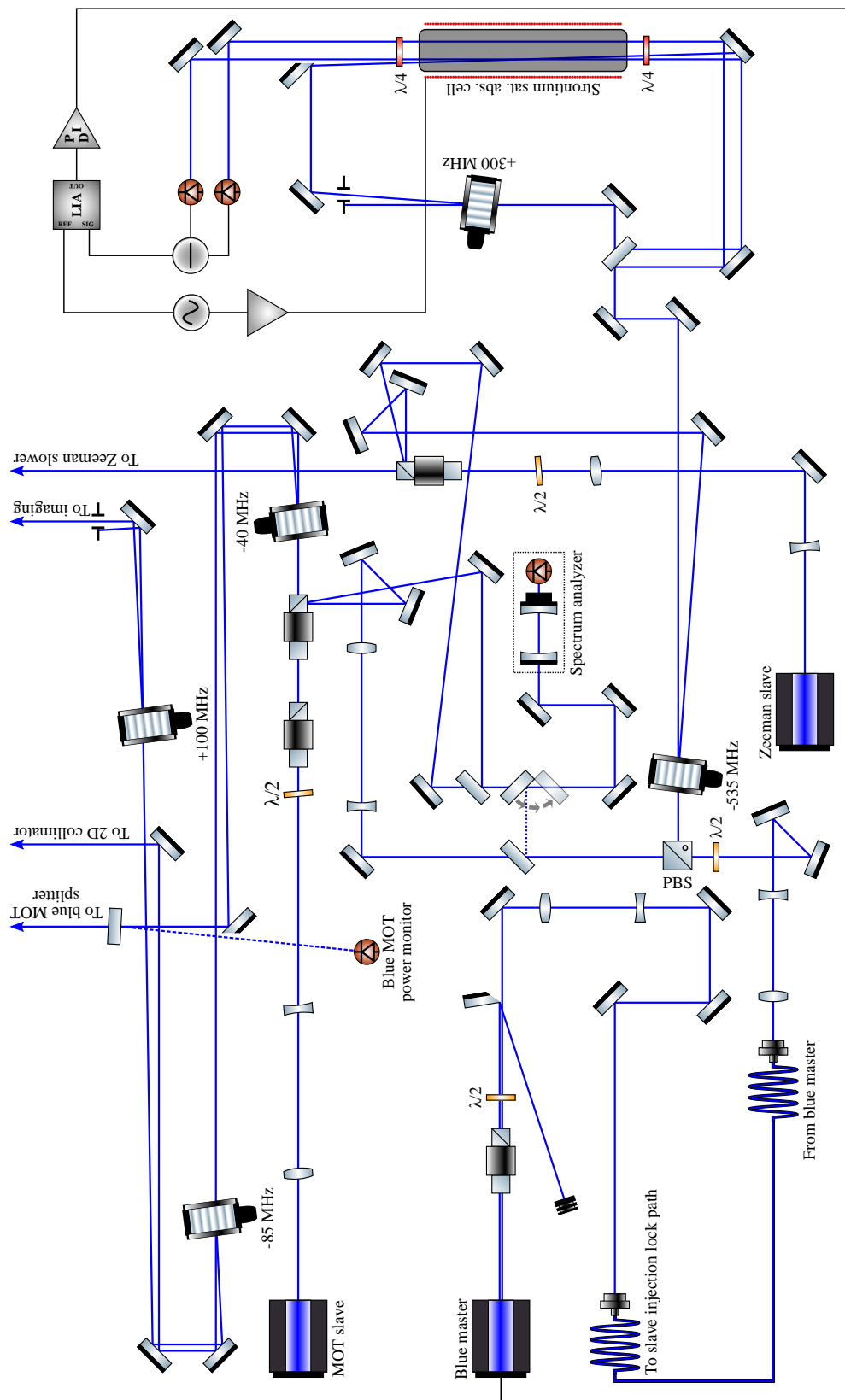


Figure 2.9: Simplified diagram of the 461 nm laser system.

heating our samples. Mechanical shutters<sup>38</sup> are used to provide 100 % extinction. \*\* Some details about our blue cooling system can be found in [45, 68]. \*\*

### 2.5.2 481 nm Repumping System

Before moving on to the narrow line “red” MOT, the atoms in the metastable reservoir are dark to both the 461 nm and 689 nm cooling light and must be brought back to the ground state.

The current 481 nm repumper system is shown in Fig. 2.10. The 481 nm light is provided by a Toptica DL 100<sup>39</sup> which outputs about \*\* 10 mW \*\* of power. For now, this laser is stabilized to a Doppler-broadened  $^{130}\text{Te}_2$  line [67] that has a transition at  $20\ 776.0886\ \text{cm}^{-1}$  [105] which is close to the  $(5s5p)\ ^3P_2 \rightarrow (5p^2)\ ^3P_2$  transition at  $20\ 776.087\ \text{cm}^{-1}$  [106]. Originally, when the lab was working with a single isotope, simply tuning the lock point to maximize repumping efficiency of the isotope of interest was good enough (typically  $^{84}\text{Sr}$  since it’s the least abundant). Now that we routinely work with multiple isotopes and mixtures, a free-space electro-optic modulator (EOM) was introduced to add sidebands to the 481 nm light in order to address multiple isotopes and the hyperfine shift of  $^{87}\text{Sr}$ . The hyperfine shift of the lower  $(5s5p)\ ^3P_2$  state is known [107] and cover the hyperfine shift of the upper  $(5p^2)\ ^3P_2$  doubly-excited, is which is to be small \*\*because of the lack of an s-electron<sup>40</sup> CHECK \*\*.

In principle, it should be possible to lock to a hollow cathode lamp (HCL) due to collisions populating enough metastable atoms to perform spectroscopy on [108]. Instead of using an HCL, we plan on using a “super lock” [109–112] (see Appendix xxxx for future upgrade plans) since we already have a stable 689 nm reference laser (although we could also lock to a stabilized HeNe). We also considered a lock to the wavemeter as in [69] but ultimately decided against it as our wavemeter’s accuracy is lacking, its sampling rate a bit

<sup>38</sup>We use hard drive shutters as we’ve found them to be the most reliable.

<sup>39</sup>The laser is equipped with a LD-0488-0060-1 diode.

<sup>40</sup>I.e., the magnetic dipole hyperfine contribution comes from the  $\delta(r)$ ....

lock what to what aspect of a lamp?

possible to lock the frequency of the 481 nm laser using the  $5s5p3p2-5p23p2$  absorption feature in a hollow cathode lamp.

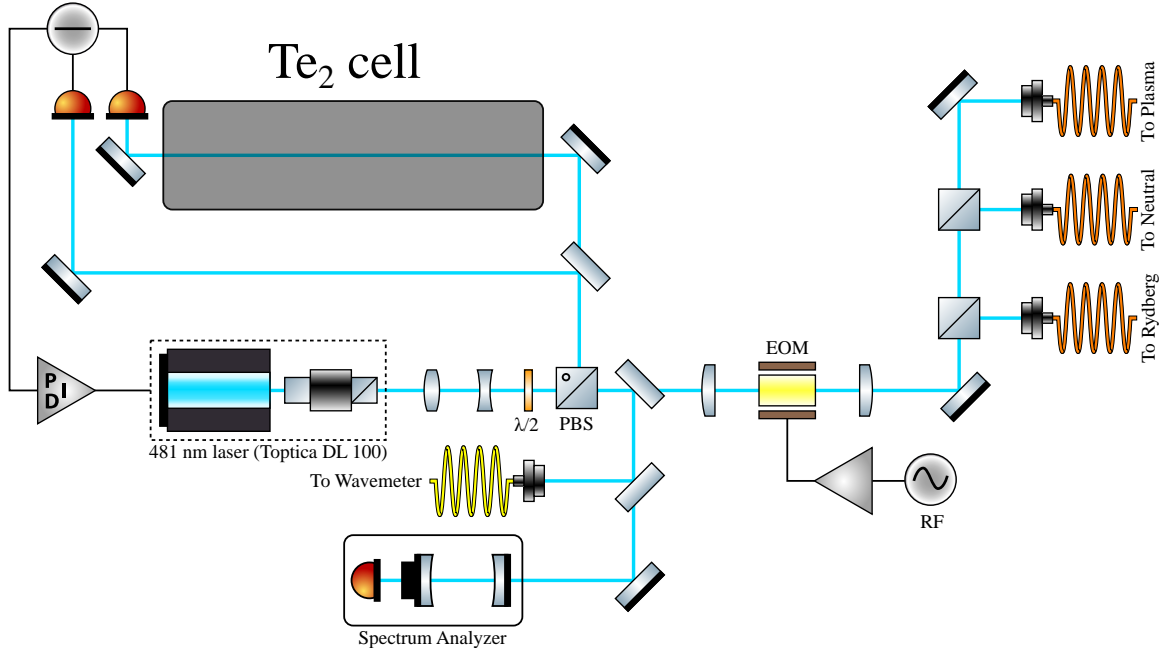


Figure 2.10: Simplified diagram of our current 481 nm repumper laser system. A portion of the light from the 481 nm external cavity diode laser (ECDL) is used to lock to a Doppler-broadened  $^{130}\text{Te}_2$  line in a cell heated to about 555 °C. The rest of the light is sent through a free-space electro-optic modulator (EOM) at about 565 MHz which is used to apply sidebands to the light in order to address the various isotopes and hyperfine states. 481 nm light is delivered to the various experiments by multimode fibers.

too slow, and we needed the wavemeter for other tasks (e.g., finding Rydberg lines).

### 2.5.3 689 nm “Red” Laser System

Some details about our narrow line cooling system can be found in [68]. The operation of the narrow line 689 nm “red” MOT can be found in [13, 25, 29, 31, 68]. ~~Details of the~~  $^{87}\text{Sr}$  red MOT is particularly well described in [13] and will not be reproduced here.

#### 689 nm Master Laser

A single 689 nm Toptica DL pro ECDL serves as our master laser and is shared between the Rydberg and Neutral experiments. The laser is first locked to a homebuilt high-finesse

Fabry-Pérot (FP) cavity<sup>41</sup> which is then locked to a heated strontium saturated absorption cell. Since the  $^1S_0 \rightarrow ^3P_1$  is very weak, the cell is relatively long to allow enough absorption to occur. For most of the experiments described in this thesis, the red master laser was found to have a linewidth of about 30 kHz. A diagram of the red master laser system is presented in [68]. \*\* More details of the 689 nm master laser system is provided in Jim's Ph.D. thesis. \*\* We recently purchased a ULE cavity from Stable Laser Systems (SLS). Some additional details in appendix G.0.2.

Due to the ease of building 689 nm slave lasers [68], we only need a single 689 nm stabilized master laser system to run both the Rydberg and Neutral experiments. From the red master table, two fibers run to each experiment with light at the following frequencies:

- $f_{\text{master}}$  – This light is locked to  $-82$  MHz of the  $(5s^2)^1S_0 \rightarrow (5s5p)^3P_1$  transition in  $^{88}\text{Sr}$ .
- $f_{\text{master}} - 1440.440$  MHz – This light is generated by passing the light directly out of the 689 nm master laser though a freespace gigahertz AOM before being sent to fibers to the Rydberg and Neutral experiments (instead of each experiment operating inefficient gigahertz AOMs to generate their own light for trapping  $^{87}\text{Sr}$ ). This light is used to injection lock slave lasers for producing the  $^{87}\text{Sr}$  “trap” red MOT light.

We currently do not implement a fiber phase noise cancellation system [113, 114] so it's possible that the light at the slave lasers is broadened to \*\* kilohertz-levels \*\* over the 25 m fibers delivering master light to the Rydberg experiment but it shouldn't be too difficult to implement in the future when necessary.

## Rydberg Red Laser System

Once the red light arrives on the Rydberg table, typically only about 1 mW is available so we use the master light to injection lock slave lasers to increase the available 689 nm power.

---

<sup>41</sup>  $F \gtrsim 2040$ . Additional details can be found in [28].

689 nm slave lasers are relatively easy to build and are detailed in [68]. We currently use a rejected beam from the slave laser isolator to monitor the mode of the slave laser. In the future, I would instead use a stray reflection or beam sampler after the isolator as the current arrangement could lead to a small amount of light from the spectrum analyzer cavity getting back to the slave lasers (especially since we share the spectrum analyzer cavity with multiple slaves), possibly leading to instability issues.

Figure 2.11 shows what the red MOT system looks like when set up for trapping any combination of isotopes. In practice, we don't always have all the red MOT AOMs lined up, typically only keeping the AOMs necessary for trapping the isotope(s) for a particular experiment while the other red MOT AOMs are used to generate various other beams (e.g., spectroscopy, "blow away", etc.). Without using a fiber combiner, we're able to devote a lot of power to the red MOT for each isotope, enabling us to use large red MOT beams. The drawbacks is that we're much more sensitive to misalignments and the ugly intensity profiles out of the diodes lead to strange red-MOT shapes.

We currently have three slave lasers that amplify the light from the red master. We found that fiber-coupling the injection beams made them much less sensitive to mechanical drifts and greatly increased the ease of switching the frequency of the slave laser by changing the source of the injection beam.

\*\*\*\* Image of  $^{84}\text{Sr}$  and  $^{87}\text{Sr}$  red MOTs. \*\*\*\*

Since the red MOT is only operated for a few hundred milliseconds, the zeroth-order from the red MOT AOMs also provide the light for various other purposes (e.g., spectroscopy, loss, etc.).

\*\* Mention SWAP cooling? [Snigirev2019.arXiv.1903.06435, 75–77]. \*\*

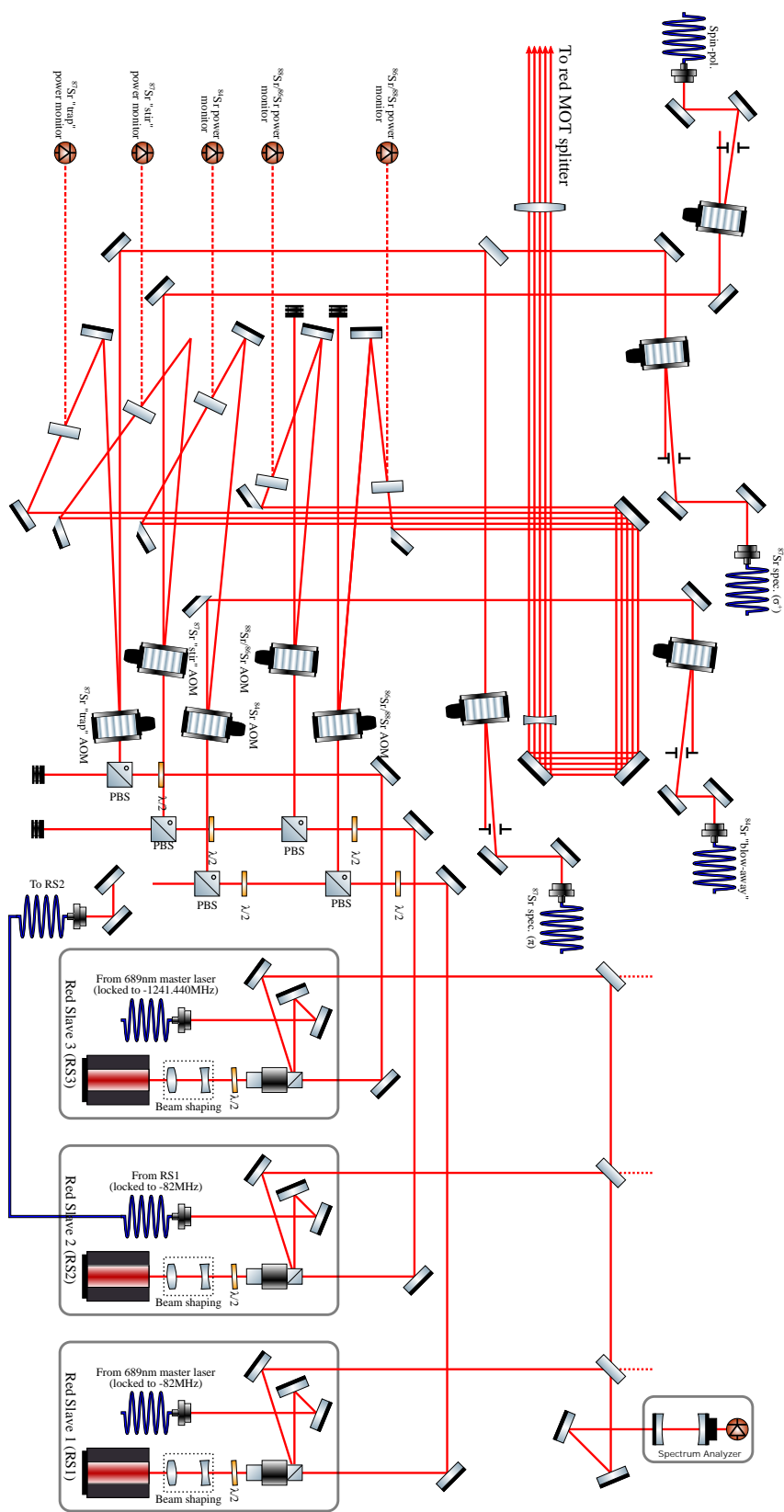


Figure 2.11: Simplified diagram of the red MOT system (when everything is put together) for multi-isotope trapping. The master laser frequency is referenced to the  $(5s^2)1S_0 \rightarrow (5s5p)3P_1$  in  $^{88}\text{Sr}$ .

### 2.5.4 Optical Dipole Trap System

**atoms**

Strontium in the ground ( $5s^2$ )  $^1S_0$  state have a negligible magnetic moment meaning

**They cannot be magnetically trapped. This necessitates**

the use of optical traps.

too many  
'we' and  
'our'  
statements.

Our current high-power 1064 nm laser system is powered by a Nufern NuAMP SUB-1382

which amplifies a few milliwatts of 1064 nm seed light to about 50 W. There are apparently

**We use a standard amplifier, without any modifications to reduce the amplitude noise such as those described recently for use in**

in quantum gas microscopes

[115, 116] but we have not done such modifications. Due to the high IR powers, we used fused silica optics whenever possible although we still have BK7 Brewster plates in the Thorlabs IO-5-1064-VHP isolator [115, 116].

**after**

We have used both free-space and fibered optical dipole traps but due to having to replace and realign the high-power IR lasers multiple times, the fibered systems due to them not losing alignment. The drawback to the fibered ODT systems is that it's difficult to couple more than about 10 W through a fiber continuously without thermal effects degrading the coupling efficiency. We get around this issue by only having the ODT on at high powers during the transfer from the red MOT before quickly moving on to the evaporation stage.

that's a lot of BECs

We started with a free-spaced crossed-beam optical dipole trap (XODT) with waists of about  $60 \mu\text{m} \times 60 \mu\text{m}$ . This trap was a bit tight but worked well for making 100 000 BECs of  $^{84}\text{Sr}$ . We found that loading was improved if the trap was artificially widened by driving the AOM with three slightly different frequencies before turning the sideband frequencies down and evaporating [117]. After going through three ODT lasers, we stuck with the sheet trap and vertical crossing trap because they were fiber coupled. Having the fiber-coupled sheet trap saved our ass as we've had to switch out the high-power laser multiple times (from the Coherent Verdi-IR, Nufern NuAmp, to IPG, back to Nufern NuAmp).

This is never appropriate in a scientific document.

For the high-power 1064 nm fibers, we've had good experiences using PMJ-A3AHPC,A3AHPC-

is this one fiber type or two?

1064-6/125-3AS-L-1<sup>42</sup> from OZ Optics.

The current main ODT is comprised of a single high-aspect ratio “sheet” trap with beam waists of about 28  $\mu\text{m}$  (vertical) by 264  $\mu\text{m}$  (horizontal), see Fig. 2.12. The design of the sheet trap was limited by the 1-inch-diameter optics used and the relatively long distance from the last lens to the atoms.

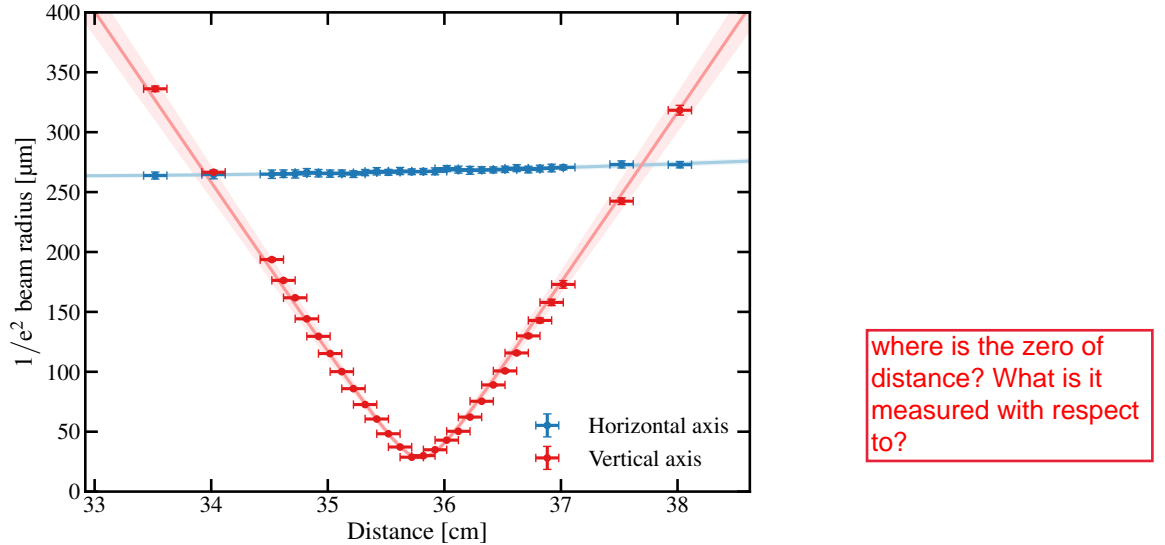


Figure 2.12: Beam profile of the sheet trap from which we fit to obtain the beam waists. For the vertical waist:  $w = 28.0(10) \mu\text{m}$ ,  $z_0 = 35.795(9) \text{ cm}$ , and  $M^2 = 1.18(4)$ . For the horizontal waist:  $w = 263.5(9) \mu\text{m}$ ,  $z_0 = 32.3(4) \text{ cm}$ , and  $M^2 = 1.0$ . Distances are measured from the end of the cage system assuming  $\pm 1 \text{ mm}$  uncertainty.

To increase the horizontal trap frequency, we also implemented a circular ODT beam that intersects the sheet trap at a near vertical angle. The measured beam profile of the vertical trap is shown in Fig. 2.13. We attempted to circularly polarized the vertical ODT so that we would be able to minimize the differential shifts and enable cooling in to the ODT [26, 118] but we didn’t observe any improvement in loading the ODT. This lack of improvement is probably due to our 689 nm laser system being a bit too broad to take advantage of this.

<sup>42</sup>These fibers are air-gapped and have an endcap on the ends that allows the beam to expand before entering/exiting the fiber, reducing the power density. The adjustable fiber tip positions allow for optimization of coupling efficiency in to the fiber.

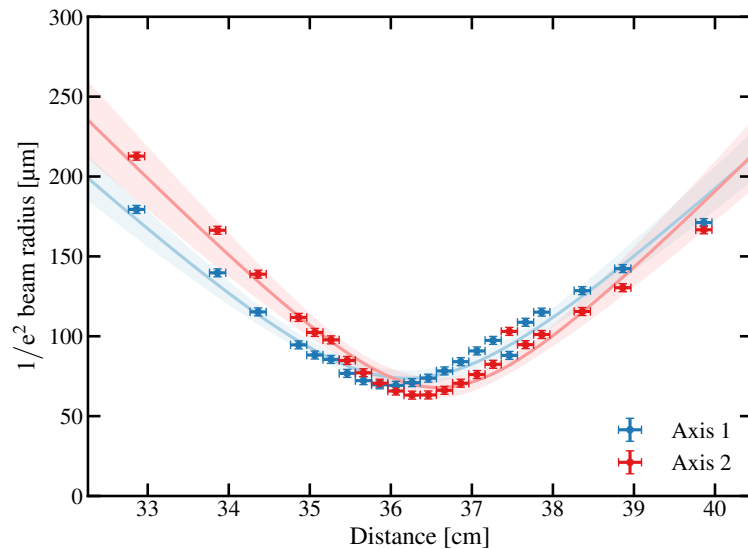


Figure 2.13: Beam profile of the vertical trap from which we fit to obtain the beam waists. An assumed  $\pm 1$  mm uncertainty in the measured distance and  $\pm 5 \mu\text{m}$  uncertainty in the measured waist size.

## 2.6 Making and Detecting Rydberg Atoms

After creating an ultracold sample of strontium,

Now that we have an ultracold sample of strontium, we use a 320 nm UV laser system to excite them to Rydberg atoms via the two-photon transition from the intermediate  $(5s5p)^3P_1$  state. The electric field system and charged particle detection will be detailed in Joe Whalen's upcoming Ph.D. thesis so they will only be briefly covered here.

### 2.6.1 320 nm UV Laser System

Strontium Rydberg atoms are produced using a two-photon transition where a 689 nm and a 320 nm photon drives atoms from the  $(5s^2)^1S_0$  ground state to either a  $(5sns)^3S_1$  or  $(5snd)^3D_J$  states.

Generation of the 320 nm radiation starts with a tunable, narrow linewidth 1064 nm seed laser that is amplified to about 7.5 W by a fiber amplifier<sup>43</sup>. We currently have two 1064 nm seed lasers have been used for experiments

<sup>43</sup>IPG Photonics YAR-15K-1064-LP-SF ytterbium fiber amplifier.

- Koheras Basik BMY10PztSPm, KOH2038 – The narrowest 640 nm lines we've observed with this seed are around \*\* 1 MHz \*\*, likely limited by the slow feedback bandwidth of the piezo element, but it's capable of tuning multiple GHz so it's preferred for experiments requiring large tuning.
- NP Photonics Rock RFLM-50-3-1064.53-1-S-0 – The feedback bandwidth of this laser is quite a bit better than the Koheras with \*\* 250 kHz \*\* being the narrowest features we've observed. Although the feedback bandwidth results with a narrow 640 nm linewidth, it's more difficult to continuously tune large ranges.

The output of the fiber amplifier pumps a Lockheed Martin Aculight Argos Model 2400 CW optical parametric oscillator (OPO) modified with a sum frequency generation stage. Similar to the setup described in [119], OPO-SFG is achieved by replacing the standard OPO crystal with periodically poled, magnesium-oxide-doped lithium niobate crystal (MgO:PPLN) where the first section is poled for OPO and second section is poled for SFG. The cavity dichroics were also replaced. The OPO section uses the  $\lambda_P = 1.064 \mu\text{m}$  pump to generate  $\lambda_S = 1.6 \mu\text{m}$  and  $\lambda_I = 3.2 \mu\text{m}$  light. The SFG section then combines the  $\lambda_S = 1.6 \mu\text{m}$  with another  $\lambda_P = 1.064 \mu\text{m}$  to produce  $\lambda_{\text{SFG}} = 640 \text{ nm}$ .

As mentioned in [120], temperature tuning of the crystal is required for efficient 640 nm generation but the Argos system was only designed for heating. A workaround was developed where a water-cooling block was attached to the outside of the OPO cavity housing to lower the temperature enough to where the Argos' internal heater is capable stabilizing the temperature (see Fig. 2.14). With this addition, we typically get about \*\* (1-1.5) W \*\* of 640 nm.

Stabilization of the 640 nm laser frequency is accomplished with a transfer cavity lock [121–123] where the length of a tunable optical cavity is first stabilized by locking a resonance feature to the 689 nm laser (which itself is stabilized to an atomic reference), and then stabilizing the 640 nm to the cavity. Some of the details of our transfer cavity are documented in [124]. Briefly, our transfer cavity is constructed from an Invar body with the cavity mirrors attached to a

feature to the 689 nm laser

The 640 nm laser is then stabilized by locking its frequency to a resonance of the cavity.

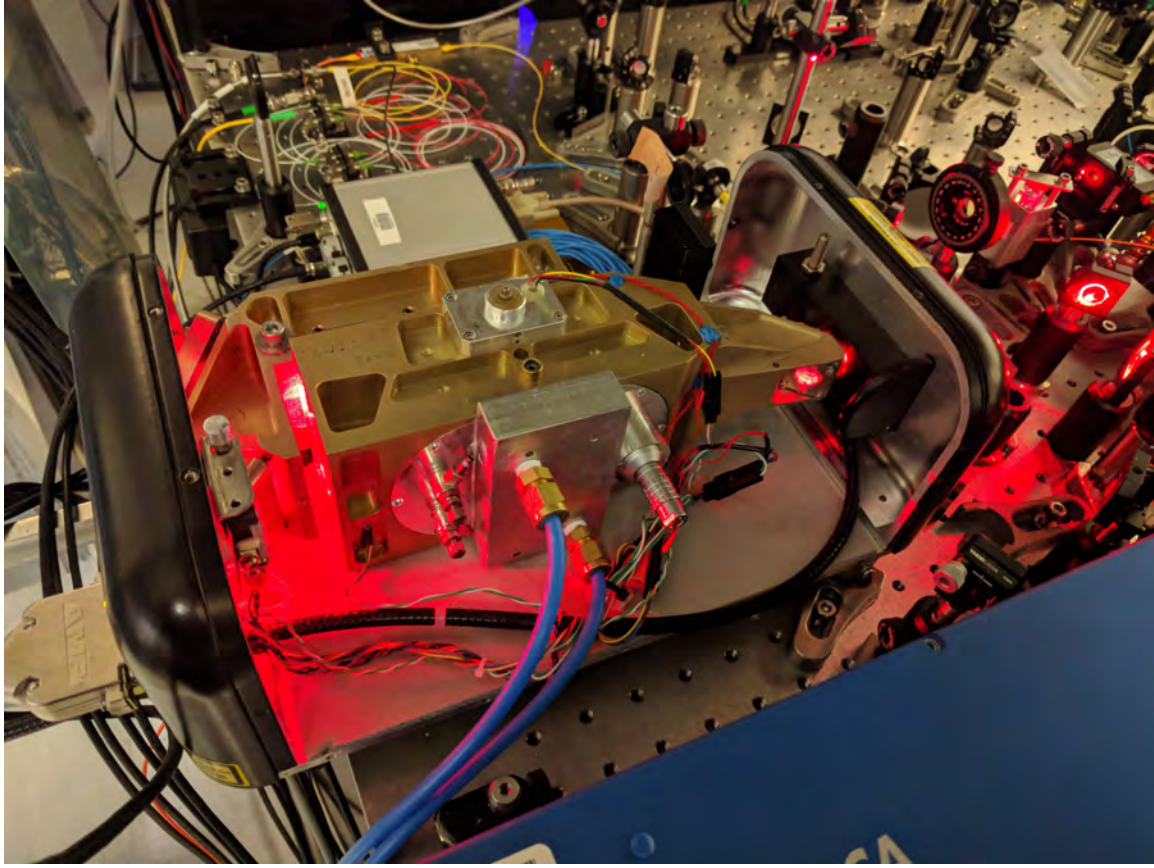


Figure 2.14: Picture of the Lockheed Martin Aculight Argos Model 2400 CW OPO with the custom water-cooling block attached to the cavity housing. The current tubing on the cooling block is a bit too stiff to bend enough to put the laser cover on.

piezoelectric (PZT) stack on each end. The PZT on one end is used to stabilize the cavity length to the 689 nm laser while the other end provides a tunable “offset” which we can use to lock to different FSRs of the transfer cavity. Pound-Drever-Hall (PDH) [125, 126] is used to lock the cavity length to the 689 nm reference and to lock the 640 nm to the cavity. The optical layout at the transfer cavity is shown in Fig. 2.15. Tunability is achieved with a broadband fiber EOM (fEOM) between the 640 nm laser output and the transfer cavity. The PDH error signal is fed back to the 1064 nm seed laser. Although we have not done a full characterization of the linewidth of the 640 nm laser, the narrowest Rydberg lines we have seen are about \*\* 150 kHz in 640 nm\*\* which can be considered an upper bound on the laser’s short-term stability. Longer-term stability isn’t as good where we have seen

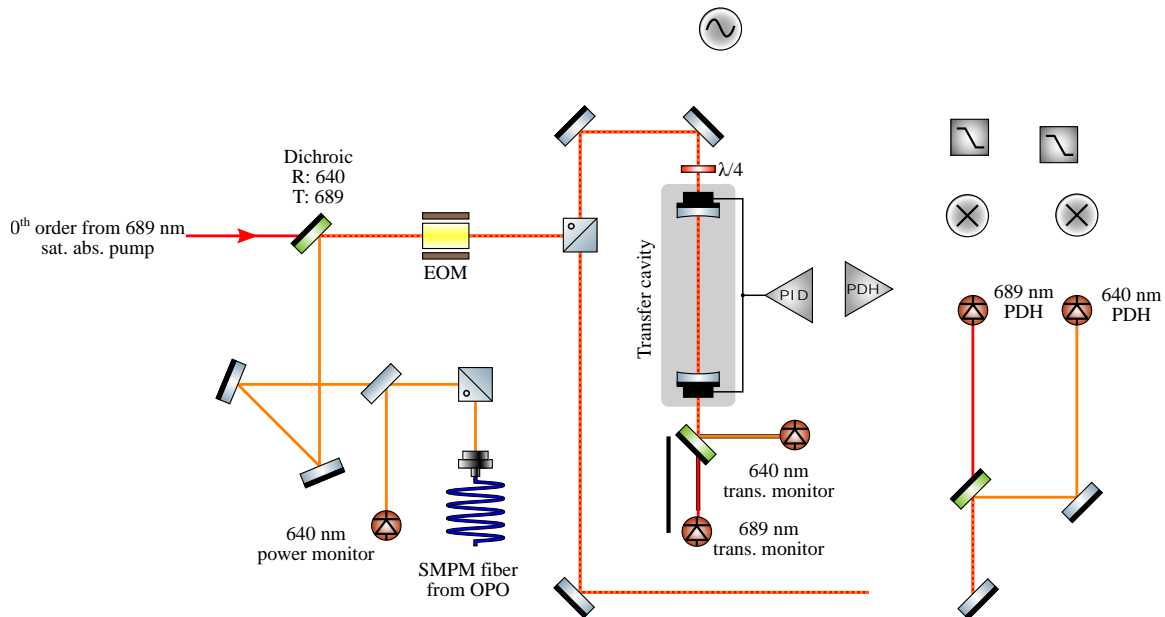


Figure 2.15: Simplified diagram of our transfer cavity setup. \*\* NEED TO FINISH \*\*.

drifts of about \*\* 500 kHz \*\* when scanning over the same Rydberg (molecule) lines. With the recent acquisition of a ULE cavity (see appendix G), we plan to eliminate the transfer cavity in favor of locking the 640 nm directly to the ULE cavity with a setup similar to the one presented in [127].

Now that we have a tunable and stabilized The 640 nm output from the OPO is ~~then~~ coupled in to a commercial Toptica second-harmonic generation (SHG) pro system which ~~produces~~ doubles the 640 nm to 320 nm. When well-tuned, the system is capable of outputting \*\* > 500 mW of power but it tends to degrade over time. Our typical operating powers are closer to about 100 mW.

## 2.6.2 Electric Field System

Due to the extreme  $n^7$  scaling of polarizability [11, 128], Rydberg atoms are extremely sensitive to electric fields. To mitigate stray electric fields at the location of the atoms as well as to provide the capability for trimming residual electric fields and perform selective field ionization (SFI), ~~we~~ installed in-vacuum electric field plates. The electric field plate

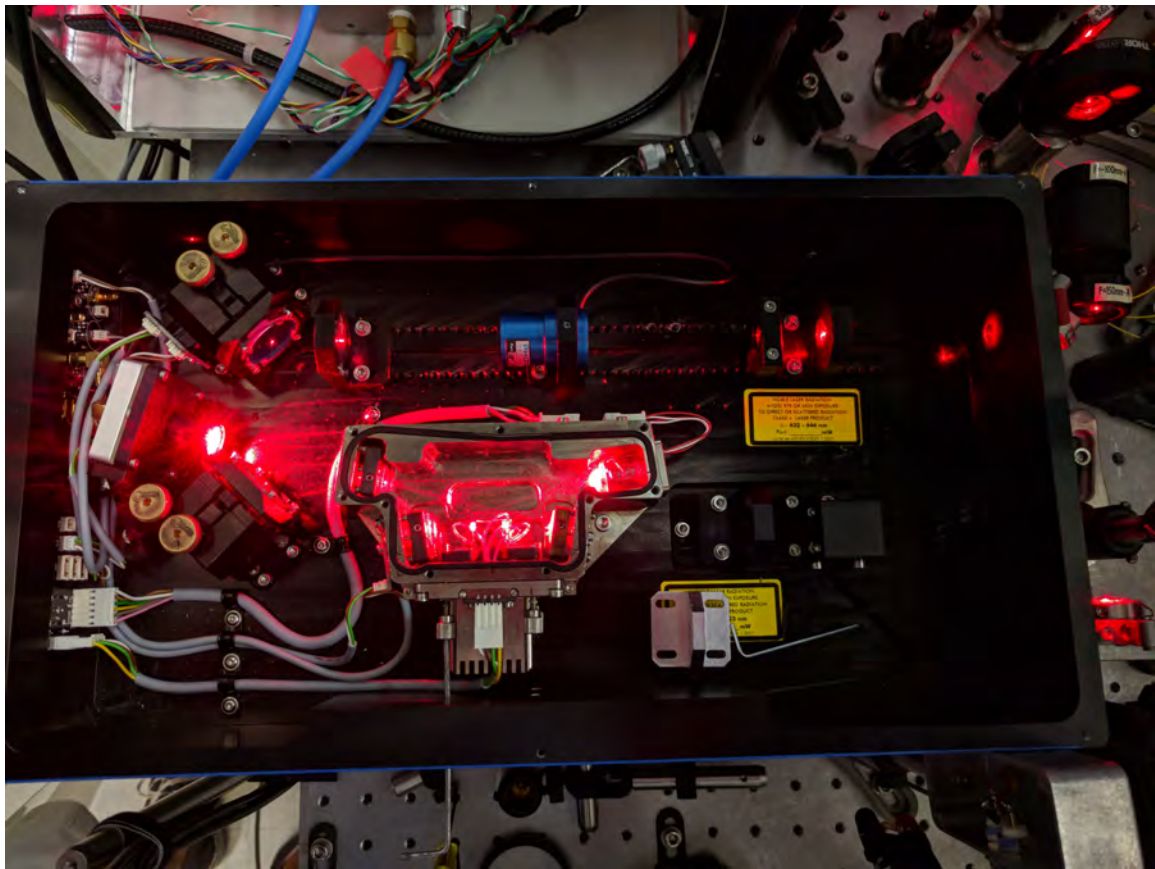


Figure 2.16: Picture of the Toptica SHG pro bow tie doubling cavity. The normally-sealed SHG cavity was opened up when realigning the 640 nm to the cavity.

system was designed by Francisco Camargo and additional details his Ph.D. thesis [117] and the design follows similar ones described in [129, 130] using a split-ring electrode geometry with four quadrant electrodes above and four quadrant electrodes below the center of the chamber (i.e., where the atoms are). The split-ring electrodes and in-vacuum wires are made from oxygen-free high conductivity (OFHC) copper with stainless steel making up the supporting scaffold, Einzel lens, and guiding plates. All parts were polished by hand before being sent off to be electropolished.

not if it is in Francisco's thesis.

Stuff about the scaffold and copper electric field plates. SIMION simulations? \*\*

We currently have a (limited) ability to change how the electric field plates are ramped depending on whether want want to detect electrons or ions, and whether we want to

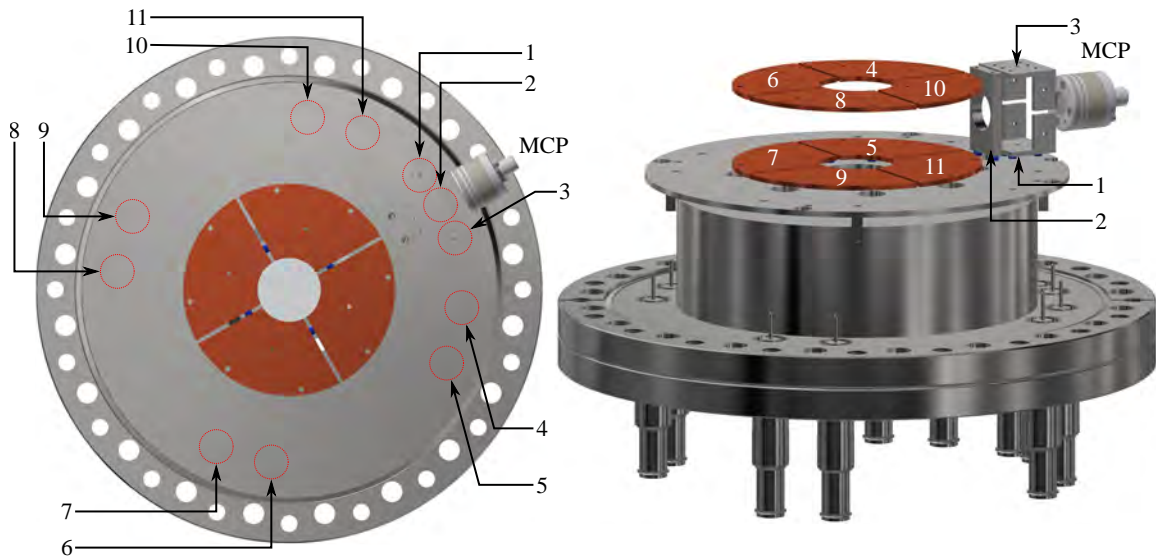


Figure 2.17: CAD renderings of the electric field plates with most of the supporting scaffold removed. Blue spheres represent the sapphire spacers used to isolate the high-voltage components from the grounded support structure. (Left) Top view of the eight electric field plates, Einzel lens, guiding plates, and MCP. The eleven 10 kV SHV feedthroughs are numbered clockwise. Red circles highlight the locations of the feedthroughs which are partially obstructed from view by the bottom scaffold plate. (Right) The electrodes are numbered corresponding to the feedthrough on the bottom flange.

perform selective field ionization (SFI). Most of the work presented in this thesis involves detecting electrons and just using the integrating the SFI spectra (i.e., we simply count all the electrons). When taking data, we monitor the SFI spectra to make sure that the entire Rydberg signal(s) is captured but the data analysis simply uses the total Rydberg electron counts. An example SFI spectrum is shown in Fig. 2.21.

too informal

Working at high- $n$ , Soumya was able to trim electric fields to better than \*\* xxxx V/cm

\*\* when taking spectra at  $n = 160$ . It should be possible to improve electric field zeroing more with careful biasing of the SFI HV switches, or using more advanced techniques.  
a bit more if we're more careful with switching would likely require going

For now, the electric field system is sufficient for our purposes.

Using spectra at high  $n$  (~sim 160), it is possible to trim electric fields to better than xxx [reference Soumya's thesis, don't state his name.]

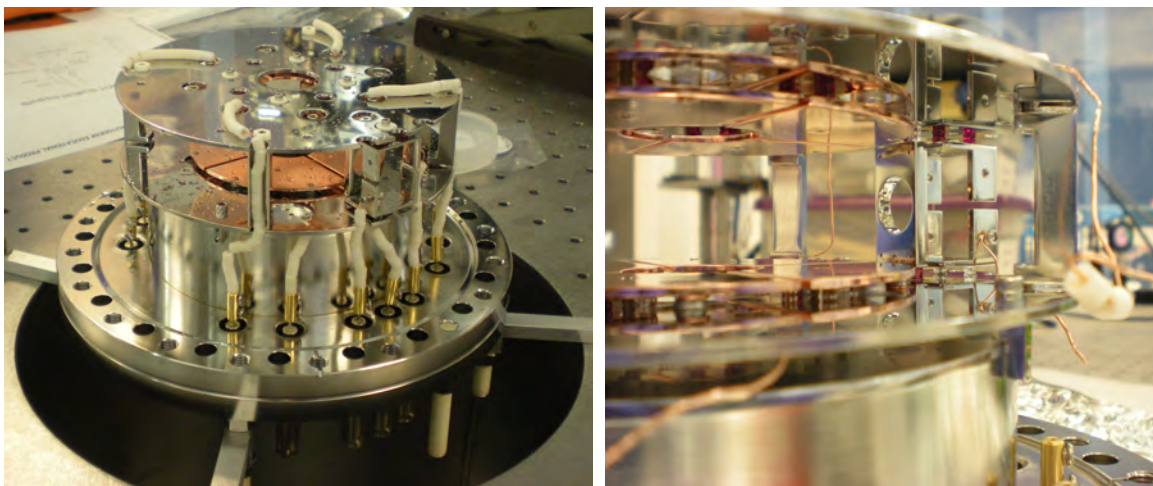


Figure 2.18: (Left) Overview of the actual electric field system mounted on the bottom flange of main chamber. Connections between the feedthroughs and the electric field plates are made with OFHC wires and insulated from the grounded supporting scaffold with ceramic fish spine beads. Beryllium-copper inline barrel connectors with two cross-screws attach the wires to the feedthroughs. (Right) Close up of the eight electric field plates, Einzel lens, and guiding plates. The sapphire spheres (red or clear) which isolate the high-voltage parts from the grounded scaffold structure are also visible.

### 2.6.3 Charged Particle Detection

One of the major aspects which separates our experiment from most other neutral atom experiments is the ability to detect charged particles. Some of the previous work with strontium Rydberg experiments was carried out in the Neutral apparatus but since they lacked the ability to detect charged particles, they had to resort to detecting atom loss in absorption images [16, 17, 131]. Our system was designed from the beginning to be able to detect charged particles which we've found to be incredibly sensitive with teh ability to detect signals spanning several orders of magnitude [132]. \*\* Since Joe will be detailing the electric field ionization and detection system in his upcoming Ph.D. thesis, only the major details are included here for completeness. \*\*

too informal

An overview of how our charted particle detection system works is shown in Fig. 2.19. The following procedure explains how we detect electrons as that's what we primarily work with but we have configured our system to detection ions instead. \*\* CHECK !! \*\*

After performing a Rydberg excitation on a sample, we typically apply a symmetric field ramp where the plates closer (further) from the MCP are ramped to positive (negative) high-voltage to push electrons towards the MCP. The length of the cables from the HV switch<sup>44</sup> to each of the feedthroughs are about the same length to keep the capacitance approximately equal. We adjust the HV supplies for the electric field plate ramps depending

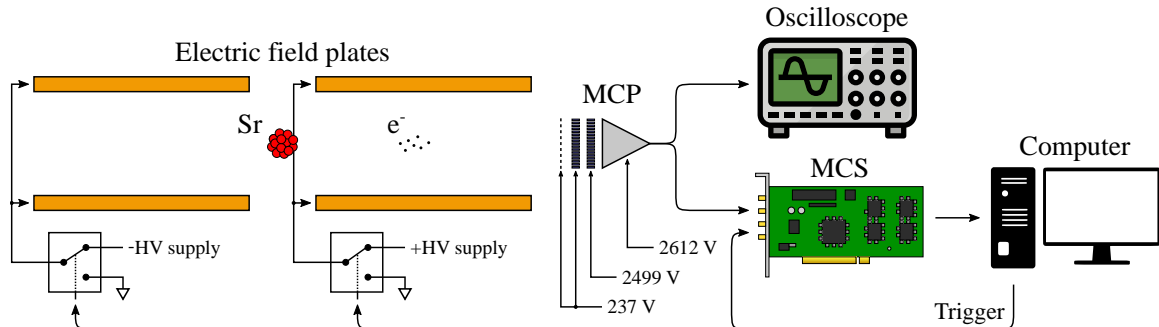


Figure 2.19: Simplified diagram of how the charged particle detection system works when set up for counting electrons.

on which principal quantum number ( $n$ ) of the Rydberg state we are exciting. Due to the cable capacitance, this also affects the ramp rate of the applied electric field but it doesn't significantly affect our data since we're primarily interested in the integrated SFI spectrum,

Charged particles are detected with an MCP<sup>45</sup>, where the front plate is kept fixed at 200 V while the back of the MCP is fixed at 2650 V. The MCP is mounted to a 2.75 in flange with four HV feedthroughs with ceramic insulation. Currently, the MCP's output is first connected to a preamplifier<sup>46</sup> which is then fed in to an RF amplifier<sup>47</sup> to remove DC offsets before going to the MCS<sup>48</sup>. An example Rydberg signal from the MCS is shown in Fig. 2.21.

As seen in Fig. 2.22, MCPs are known to “saturate” and become non-linear as the count rate increases. This non-linearity is important to characterize to determine when the

which is the primary quantity of interest.

<sup>44</sup>Willamette High Voltage PHSVW-005.

<sup>45</sup>Photonis Advanced Performance Detector (APD) 2 miniTOF. It's important to note that we purchased the version with PEEK components so care must be taken when performing a bake-out.

<sup>46</sup>Stanford Research Systems SR445.

<sup>47</sup>ZFL-500LN.

<sup>48</sup>FAST ComTec GmbH MCA-3 P7882.

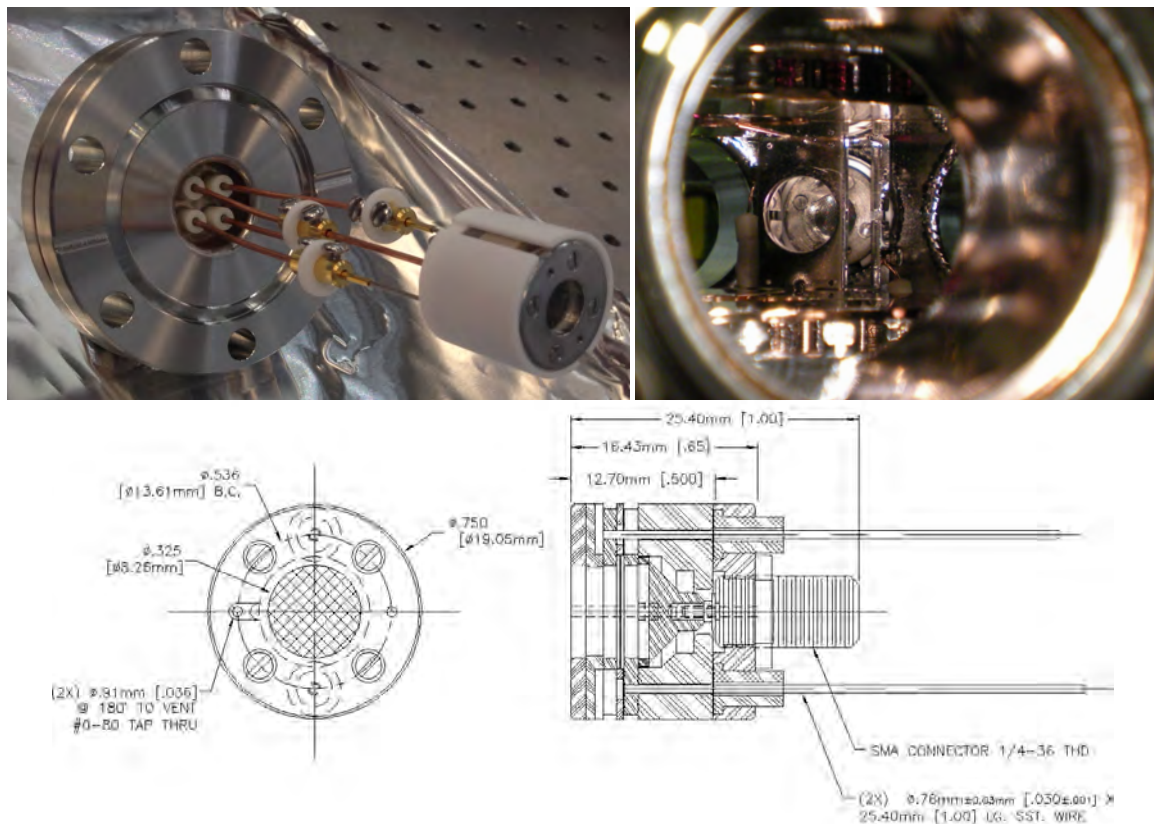


Figure 2.20: (Top left) The MCP mounted to a 2.75 in flange with high-voltage feedthroughs. Connections are made using beryllium-copper inline barrel connectors with ceramic washers ~~were placed between the screws to act as a spacer~~ to keep the connections from touching each other and the main vacuum chamber. (Top right) The MCP in the main chamber. (Bottom) Mechanical drawing of the APD 2 miniTOF MCP provided by Photonis USA.

signal is in the linear regime and when we need to start taking in to account the non-linearity in detection efficiency. Performing a fit to the empirical model

$$y = A[1 - \exp(Bx)] \quad (2.4)$$

~~allows us to determine~~ the constants  $A$  and  $B$ , so ~~that we can extract~~ correct for undercounting regardless of whether our signal is in the allowing for correction for undercounting in the non-linear regime.

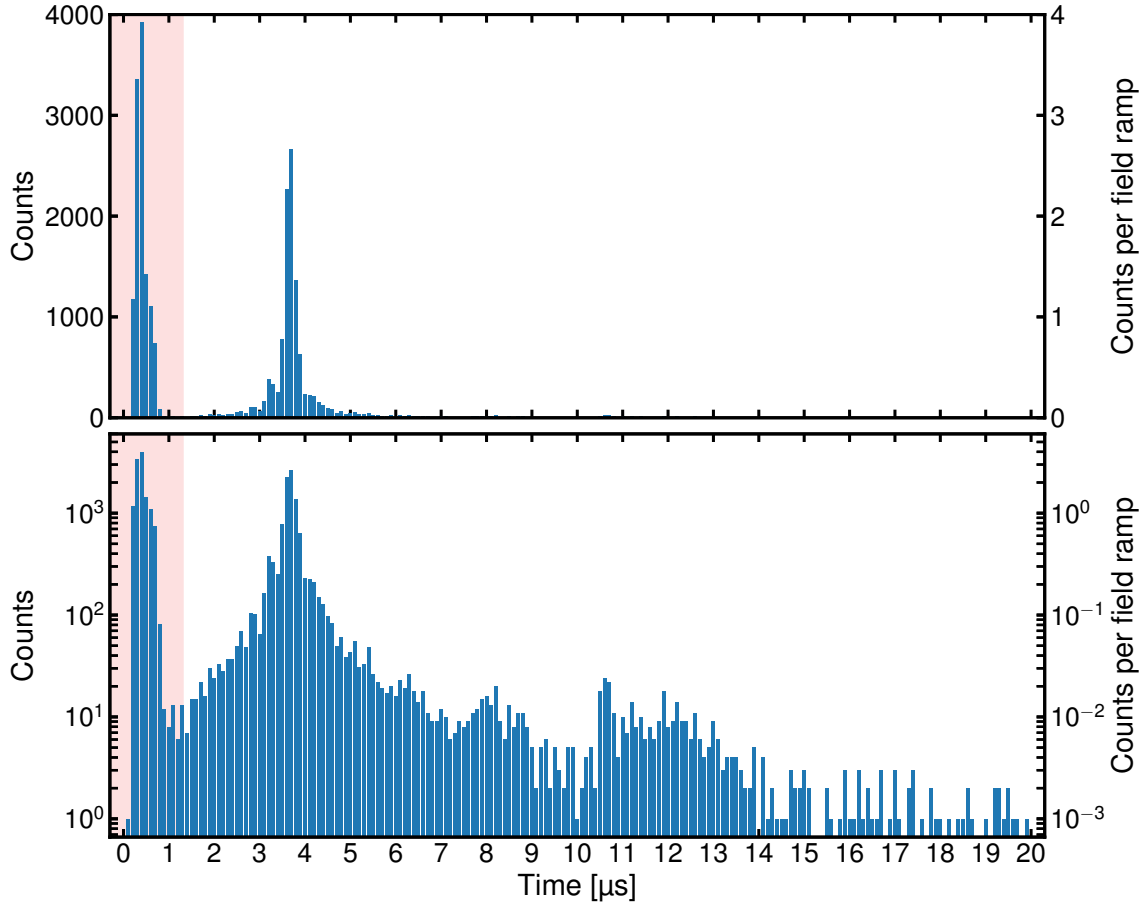


Figure 2.21: Example MCS signal from the  $(5s38s)^3S_1, F = 11/2$  Rydberg line in  $^{87}\text{Sr}$  for a single detuning in (top) linear scale and (bottom) log scale. There are 200 100 ns bins with the electric field ramp starting at  $t = 0$  ns. To increase signal, we perform multiple excitation-detection sequences and sum the resulting counts bin-by-bin. Dividing by the total number of loops gives the counts per bin per loop (1000 loops were used in the data above). The MCS detects a large “kick” for first several bins (shaded region) so the data in those bins (shaded region) are dropped before proceeding with the analysis.

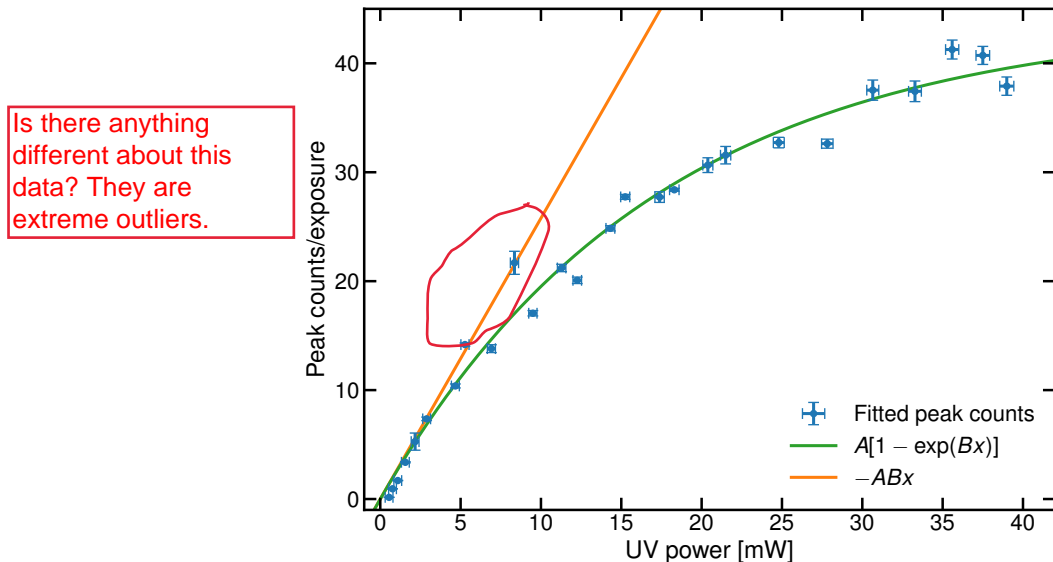


Figure 2.22: Peak integrated SFI spectrum per  $10\text{ }\mu\text{s}$  exposure vs. UV excitation power exciting to the  $(5s33s)^3S_1, F = 11/2$  state of  $^{87}\text{Sr}$  in a  $B_x \approx 1.1\text{ G}$  bias field ( $689\text{ nm}$  power kept constant). The peak counts were obtained by fitting to the Zeeman-split spectra and extracting the height of the  $m_F = 11/2$  line. Since  $1000\text{ }10\text{ }\mu\text{s}$  exposures were used for each frequency point, the fitted peak counts was divided by  $1000$  to obtain the counts per exposure. Fitting to the empirical model  $A[1 - \exp(Bx)]$  results with the coefficients  $A = 44.0(17)$  and  $B = -0.059(5)$ .



### 3. Spectroscopy of $^{87}\text{Sr}$ Triplet Rydberg States

---

In order to study strontium Rydberg atoms, it's necessary to ~~be able~~ to locate and identify the Rydberg state being excited. Most spectroscopic studies of strontium Rydberg systems have focused on the most abundant isotope,  $^{88}\text{Sr}$ , which has no nuclear spin ( $I = 0$ ). This lack of nuclear spin ~~means no hyperfine structure~~ and leads to relatively simple excitation spectra ~~because of the lack of hyperfine structure, and the Rydberg spectrum is well understood.~~ [133–141].

In contrast, ~~the~~ on  $^{87}\text{Sr}$  which has a large nuclear spin ( $I = 9/2$ ) which leads to a strong hyperfine interaction, complicating the Rydberg excitation spectrum. Of the previous experimental work [142–146], excitation was performed to singlet Rydberg states ( $(5sns)^1S_0$  and  $(5snd)^1D_2$ ) with triplet states being observed due to state mixing. In order to better understand the  $^{87}\text{Sr}$  Rydberg spectra, we mapped the triplet Rydberg states by directly exciting  $(5sns)^3S_1$  and  $(5snd)^3D_{1,2,3}$  through the intermediate  $(5s5p)^3P_1$  state. Collaborating with theorists, we were able to develop an understanding of the  $^{87}\text{Sr}$  hyperfine Rydberg states.

Below is a summary of our work, published in [147], which was a combined experimental and theoretical study of  $(5sns)^3S_1$  and  $(5snd)^3D_{1,2,3}$  Rydberg states in  $^{87}\text{Sr}$ . The experimental work was performed at Rice with theoretical calculations performed by Dr. Shuhei Yoshida and Dr. Joachim Burgdörfer at the Institute for Theoretical Physics, Vienna University of Technology.

### 3.1 Ionization Limit of $^{87}\text{Sr}$

The first indication that the Rydberg levels of  $^{87}\text{Sr}$  were not as simple as for the bosonic isotopes was the reported ionization limit,  $E_{\text{ion}}^{87} = 45\,932.2861(10) \text{ cm}^{-1}$  [106, 134], being well above those of the bosonic isotopes (see Fig. 3.1 and Tab. C.3). Mass-scaling the

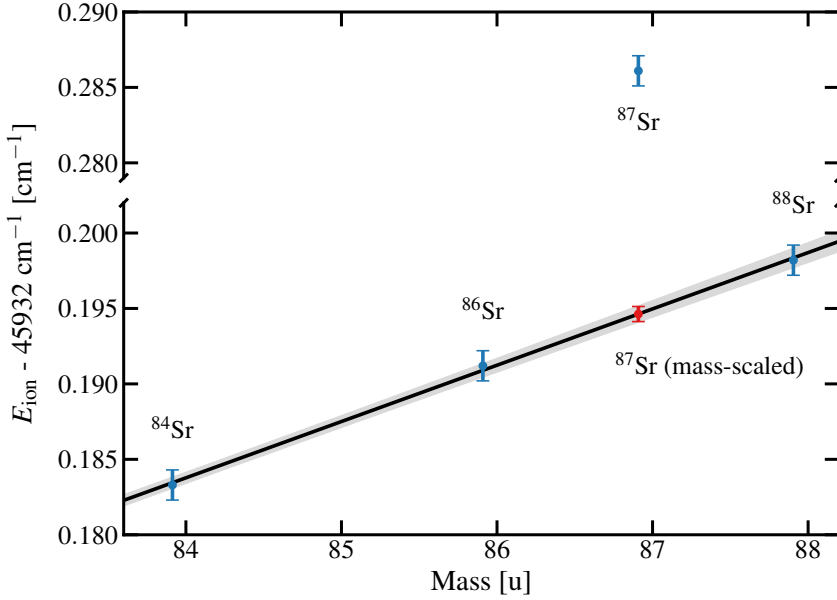


Figure 3.1: (Blue points) Reported isotopic ionization limits ( $E_{\text{ion}}$ ) vs. isotope mass. A linear fit (black line) is used to estimate the  $E_{\text{ion}}^{87}$  for an assumed  $I = 0$   $^{87}\text{Sr}$  atom from the ionization energies of the bosonic isotopes. See appendix C for isotopic masses and ionization energies.

ionization energies of the bosonic isotopes suggests that the ionization energy for an assumed  $I = 0$   $^{87}\text{Sr}$  atom should be  $45\,932.1946(5) \text{ cm}^{-1}$ , about 2.74 GHz below the reported ionization energy.

The source of this discrepancy is likely related to the hyperfine interaction in the ground state of  $^{87}\text{Sr}^+$ . Since ground state  $^{87}\text{Sr}^+$  has a rubidium-like structure with a single valence  $s$  electron outside a filled [Kr] core, the hyperfine interaction can be written as (see, e.g., [148])

$$\hat{V}_{\text{hfs}} = A_{\text{hfs}} \hat{\vec{\mathbf{I}}} \cdot \hat{\vec{\mathbf{J}}} = A_{\text{hfs}} \hat{\vec{\mathbf{I}}} \cdot \hat{\vec{\mathbf{S}}} \quad (3.1)$$

where  $\vec{\mathbf{J}} = \vec{\mathbf{L}} + \vec{\mathbf{S}}$  and  $A_{\text{hfs}}$  is the strength of the magnetic dipole hyperfine interaction. Note that there are no higher order contributions (e.g., electric quadrupole) since the valence electron is in an  $s$  state so only the contact interaction is non-zero [149]. Following the usual procedure by defining  $\vec{\mathbf{F}} = \vec{\mathbf{J}} + \vec{\mathbf{I}}$ , the energy shift can be evaluated as

$$\langle \hat{V}_{\text{hfs}} \rangle = \frac{A_{\text{hfs}}}{2} \langle \hat{\mathbf{F}}^2 - \hat{\mathbf{J}}^2 - \hat{\mathbf{I}}^2 \rangle = \frac{A_{\text{hfs}}}{2} [F(F+1) - J(J+1) - I(I+1)] \quad (3.2)$$

In the ground state of  $^{87}\text{Sr}^+$ ,  $S = s = 1/2$  and  $I = 9/2$  meaning the the  $(5s)^2 S_{1/2}$  is split in to  $F = 4$  and  $F = 5$  components. Using  $A_{\text{hfs}} = -1\,000\,473.673(11)$  kHz<sup>49</sup> [150], the  $F = 4$  and  $F = 5$  states are shifted by

$$\langle \hat{V}_{\text{hfs}} \rangle = \begin{cases} -\frac{11}{4} A_{\text{hfs}} = 2.751\,302\,601(30) \text{ GHz}, & F = 4 \\ \frac{9}{4} A_{\text{hfs}} = -2.251\,065\,764(25) \text{ GHz}, & F = 5 \end{cases} \quad (3.3)$$

Notice that  $\langle \hat{V}_{\text{hfs}} \rangle_{F=4}$  nearly matches the 2.74 GHz discrepancy between the reported ionization limit of  $^{87}\text{Sr}$  and the ionization limit determined by mass-scaling from the bosonic isotopes. This seems reasonable since most of the earlier spectroscopic work on  $^{87}\text{Sr}$  primarily focused on the singlet Rydberg states of which converges to the upper  $F = 4$  [145] state of  $^{87}\text{Sr}^+$ .

In the analysis below, we used  $E_{\text{ion}}^{87} = 45\,932.1956(7)$  cm $^{-1}$  for the ionization limit instead of the slightly lower value  $E_{\text{ion}}^{87} = 45\,932.1943(10)$  cm $^{-1}$  obtained by subtracting  $\langle \hat{V}_{\text{hfs}} \rangle_{F=4}$  from the reported  $^{87}\text{Sr}$  ionization limit in [106, 134]. As described in [147], it was found that the higher  $E_{\text{ion}}^{87}$  resulted in the quantum defects of the  $(5sns)^1 S_0$  and  $(5sns)^3 S_1$  states converging to a nearly constant value.

### 3.2 Hyperfine Rydberg States of $^{87}\text{Sr}$

Accurate *ab initio* theoretical descriptions of the Rydberg structure of multielectron atoms is currently challenging due to the interaction of the Rydberg electron with the

---

<sup>49</sup>Sunaoshi et al. determined  $A_{\text{hfs}}$  by measuring the splitting of the  $(5s)^2 S_{1/2}, F = 4$  and  $(5s)^2 S_{1/2}, F = 5$  ground state of  $^{87}\text{Sr}^+$  in an ion trap. They measured the splitting to be  $E_{F=4} - E_{F=5} = 5\,002\,368.363(57)$  kHz.

ionic core. This interplay may lead to different configurations (“channels”) of the Rydberg electron and the ionic core which share the same total energy, angular momentum, and parity [11, 151]. When the ionic states are not well-separated from the Rydberg states, multichannel quantum defect theory (MQDT) is the commonly used method for analyzing the Rydberg states of these multielectron atoms. and it can describe the Rydberg state in terms of a few parameters [11, 152, 153]<sup>50</sup>.

Focusing on two-electron systems (e.g., <sup>3</sup>He, <sup>9</sup>Be, <sup>25</sup>Mg, <sup>43</sup>Ca, <sup>87</sup>Sr, <sup>135</sup>Ba, <sup>137</sup>Ba), we follow the approach adopted in [145, 146, 155] and separate the total Hamiltonian for the system into a part that does not depend on the nuclear spin ( $\hat{H}_0^{I=0}$ ) and the hyperfine interaction ( $\hat{V}_{\text{hfs}}$ ) which does depend on the nuclear spin

$$\hat{H}^{I \neq 0} = \hat{H}_0^{I=0} + \hat{V}_{\text{hfs}} \quad (3.4)$$

$\langle \hat{H}_0^{I=0} \rangle$  contains the effects up to the fine structure level. The convenience of separating out the  $\hat{H}_0^{I=0}$  term becomes apparent because the eigenenergies (up to the fine structure level) can be obtained from the Rydberg-Ritz formula

$$\langle \hat{H}_0^{I=0} \rangle = E_{\text{ion}} - \frac{R}{(n - \mu_{n,L,S,J})^2} \quad (3.5)$$

with the quantum defect given by [11, 156, 157]<sup>51</sup>

$$\mu_{n,L,S,J} = \mu_0 + \frac{\mu_2}{(n - \mu_0^2)^2} + \frac{\mu_4}{(n - \mu_0^2)^4} + \dots \quad (3.6)$$

Therefore, we only need to evaluate  $\langle \hat{V}_{\text{hfs}} \rangle$  to obtain the hyperfine shifts.

The hyperfine interaction can be expressed as [159–161]

$$\hat{V}_{\text{hfs}} = A \vec{\mathbf{I}} \cdot \hat{\vec{\mathbf{J}}} = \sum_i A_i \vec{\mathbf{I}} \cdot \hat{\vec{\mathbf{j}}}_i = \sum_i A_i \vec{\mathbf{I}} \cdot (\hat{\vec{\mathbf{l}}}_i + \hat{\vec{\mathbf{s}}}_i) \quad (3.7)$$

---

<sup>50</sup>I think [154], referenced and followed by [11], would probably be a good paper to work through as they provide an example calculation.

<sup>51</sup>\*\* There's an interesting discussion on how the equation for quantum defect is supposed to be recursive with  $n^* = n - \delta(n^*) = n - \delta_0 - \delta_2/(n - \delta)^2 - \delta_4/(n - \delta)^4 - \dots$  [158] vs. the power-series expansion presented in [156] \*\*.

### 3. SPECTROSCOPY OF $^{87}\text{Sr}$ TRIPLET RYDBERG STATES

for electron  $i \in \{1, 2\}$  with the (magnetic dipole) hyperfine constant contribution of each electron to the total hyperfine shift is

$$\langle \hat{V}_{\text{hfs}} \rangle_i = A_i \langle \hat{\mathbf{I}} \cdot \hat{\mathbf{j}}_i \rangle = \frac{A_i}{2} [f_i(f_i + 1) - I(I + 1) - j_i(j_i + 1)] \quad (3.8)$$

We now consider a singly-excited Rydberg states where the “inner” electron in the  $|ms\rangle$  state (i.e., an  $s$  electron in the ground state of the ion) and the “outer” Rydberg electron in a  $|n\ell\rangle$  state. \*\*\* I don’t really like this sudden transition.... \*\*\* Recalling that the  $\langle \hat{V}_{\text{hfs}} \rangle_i \sim 1/n^3$  \*\* [160–162] \*\*, it follows that for high- $n$  Rydberg states, the  $\langle \hat{V}_{\text{hfs}} \rangle_i$  can be approximated as

$$\langle \hat{V}_{\text{hfs}} \rangle_{\text{inner}} = A_{\text{inner}} \langle \hat{\mathbf{I}} \cdot \hat{\mathbf{s}}_{\text{inner}} \rangle \quad \boxed{\text{this should be fine....just 1st order perturbation theory.}} \quad (3.9)$$

$$\langle \hat{V}_{\text{hfs}} \rangle_{\text{outer}} = A_{\text{outer}} \langle \hat{\mathbf{I}} \cdot \hat{\mathbf{s}}_{\text{outer}} \rangle \approx 0 \quad (3.10)$$

Since the “outer” electron does not significantly contribute to  $\langle \hat{V}_{\text{hfs}} \rangle$ , it follows that  $\langle \hat{V}_{\text{hfs}} \rangle \simeq \langle \hat{V}_{\text{hfs}} \rangle_{\text{inner}}$ . Here,  $A_{\text{inner}}$  is taken to be \*\* ? \*\* as the same value as  $A$  in the  $(5s)^2 S_{1/2}$  state of  $^{87}\text{Sr}^+$ .

Combining the above results, we can write the expected energies of the hyperfine Rydberg levels of isotopes with  $I \neq 0$  as a shift from the “unperturbed” levels in an isotope with  $I = 0$ .

\*\*\* I need to come up with a better derivation.... I went down a bit of a rabbit hole above... \*\*\*

#### 3.2.1 Singly Excited $S$ states

The calculation for the hyperfine shifts of singly excited  $S$  Rydberg states is not too difficult with most of the details worked out in appendix H.3. It can be shown that the four hyperfine basis states are  $|^1S_0, F = I\rangle$ ,  $|^3S_1, F = I + 1\rangle$ ,  $|^3S_1, F = I\rangle$ , and  $|^3S_1, F = I - 1\rangle$ . Using these basis states, we can evaluate the matrix elements of the hyperfine interaction

can we say this? The inner electron spin couples to the outer electron... $f_i$  is not always well defined.

and find that only the  $F = I$  states interact with the matrix elements [145]

$$\langle ^1S_0, F = I | \hat{V}_{\text{hfs}} | ^1S_0, F = I \rangle = 0 \quad (3.11)$$

$$\langle ^1S_0, F = I | \hat{V}_{\text{hfs}} | ^3S_1, F = I \rangle = \frac{a_{ms}}{2} \sqrt{I(I+1)} \quad (3.12)$$

$$\langle ^3S_1, F = I | \hat{V}_{\text{hfs}} | ^1S_0, F = I \rangle = \frac{a_{ms}}{2} \sqrt{I(I+1)} \quad (3.13)$$

$$\langle ^3S_1, F = I | \hat{V}_{\text{hfs}} | ^3S_1, F = I \rangle = -\frac{a_{ms}}{2} \quad (3.14)$$

Therefore,  $\hat{H}^{I \neq 0}$  for the interacting  $F = I$  states is

$$\hat{H}^{I \neq 0} = \hat{H}^{I=0} + \hat{V}_{\text{hfs}} = \begin{pmatrix} E_{^1S_0} & 0 \\ 0 & E_{^3S_1} \end{pmatrix} + \frac{a_{ms}}{2} \begin{pmatrix} 0 & \sqrt{I(I+1)} \\ \sqrt{I(I+1)} & -1 \end{pmatrix} \quad (3.15)$$

As mentioned previously,  $E_{^1S_0}$  and  $E_{^3S_1}$  can be obtained from Eq. (3.26) with the appropriate quantum defects for each series.

\*\*\*\*\*

\*\*\*\*\*

\*\*\*\*\*

For singly excited Rydberg states  $| (5snl)^{2S+1}L_J, m_J \rangle_J$  with the “inner” electron in the  $|5s\rangle$  state and the Rydberg electron in the  $|nl\rangle$  state, the symmetric (+) and antisymmetric (-) orbital wave functions can be written as  $|L, m_L\rangle_{L\pm} = \frac{1}{\sqrt{2}} (|ms; nl, m_L\rangle \pm |nl; ms, m_L\rangle)$ .

Combining the orbital and spin wave functions for singlet and triplet states are

$$\begin{aligned} |(msnl)^1L_J, m_J\rangle_J &= \frac{1}{\sqrt{2}} (|ms; nl, m_L\rangle + |nl; ms, m_L\rangle) |0, 0\rangle_S \\ &= |L, m_L = m_J\rangle_{L+} |0, 0\rangle_S \end{aligned} \quad (3.16)$$

$$\begin{aligned} |(msnl)^3L_J, m_J\rangle_J &= \sum_{m_L} \sum_{m_S} C_{L, m_L; 1, m_S}^{J, m_J} \frac{1}{\sqrt{2}} (|ms; nl, m_L\rangle - |nl; ms, m_L\rangle) |1, m_S\rangle_S \\ &= \sum_{m_S} C_{L, m_L; 1, m_S}^{J, m_J} |L, m_L = m_J - m_S\rangle_{L-} |1, m_S\rangle_S \end{aligned} \quad (3.17)$$

with the Clebsch–Gordan coefficients defined as  $C_{J_1, M_1; J_2, M_2}^{J, M} = \langle J_1, M_1; J_2, M_2 | J, M \rangle$ .

\*\*\*\*\*

For singly-excited  $S$  Rydberg states in strontium with the ‘inner’ electron in the  $|5s\rangle$  state and the ‘outer’ electron in the  $|n\ell\rangle$  state, the singlet and triplet basis states can be written as

$$|(5sns)^1S_0, m_J = 0\rangle = \frac{1}{2}(|5s\rangle|ns\rangle + |)\rangle(|\rangle - |\rangle) \quad (3.18)$$

$$|(5sns)^3S_1, m_J = 1\rangle = \quad (3.19)$$

$$|(5sns)^3S_1, m_J = 0\rangle = \quad (3.20)$$

$$|(5sns)^3S_1, m_J = -1\rangle = \quad (3.21)$$

\*\*\*\*\*

For singly-excited states, the hyperfine interaction of the ‘outer’ electron with the core should scale as  $\sim 1/n^3$  [162]? and should be negligible for high-lying states. We make the assumption that  $\hat{V}_{\text{hf}} \simeq a_{ms}\hat{\mathbf{s}}_{\text{in}} \cdot \hat{\mathbf{I}}$  for singly-excited Rydberg states with inner electron  $|ms\rangle$  and Rydberg electron  $|n\ell\rangle$ . Expanding  $\hat{\mathbf{s}}_{\text{in}}$  and  $\hat{\mathbf{I}}$  in terms of ladder operators gives

$$\hat{V}_{\text{hf}} \simeq \frac{a_{ms}}{2} \left( \hat{s}_{\text{in},+}\hat{I}_- + \hat{s}_{\text{in},-}\hat{I}_+ + 2\hat{s}_{\text{in},z}\hat{I}_z \right) \quad (3.22)$$

with the usual ladder operators  $\hat{J}_{\pm} = \hat{J}_x \pm i\hat{J}_y$ . Note that  $\hat{V}_{\text{hf}}$  leaves the total spin  $m_F$  unchanged, meaning it couples states of the same  $m_F$ .

For a singly-excited Rydberg state where the Rydberg electron is in the  $|n\ell\rangle$  state while the inner electron remains in the  $|ms\rangle$  state, the Hamiltonian can be approximated as

$$\hat{H} = \left( \hat{H}_0 + \hat{H}_{\text{fs}} + \zeta_{nl}\hat{\mathbf{s}} \cdot \hat{\mathbf{I}} \right) + a_{ms}\hat{\mathbf{s}} \cdot \hat{\mathbf{I}} \quad (3.23)$$

where  $\zeta_{nl}$  is the magnitude of the spin-orbit interaction (of the Rydberg electron), and  $a_{ms}$  is the strength of the hyperfine interaction of the inner  $s$  electron. Making the assumption that the terms  $(\dots)$  are the same for all isotopes, then the remaining hyperfine shift is simply due to the contact interaction between the remaining  $ms$  electron and the ion. This allows us to leverage the simpler spectroscopic data of the bosonic isotopes from which we can deduce the eigenstates and eigenenergies of an assumed  $I = 0$  atom before incorporating

isotope-specific hyperfine interactions.

$$\hat{H}^{I \neq 0} = \hat{H}_0^{I=0}(m_{I=0}, m_{I \neq 0}) + \hat{V}_{\text{hfs}} \quad (3.24)$$

where  $\hat{H}_0^{88}(m_{88}, m_{87})$  is the unperturbed Hamiltonian that yields the eigenstates and eigenenergies, for  $^{88}\text{Sr}$  but scaled by the reduced mass  $m_{87} = m_e M_{87} / (m_e + M_{87})$ .  $\hat{V}_{\text{hfs}}$  is the hyperfine interaction,  $m_e$  the electron mass and  $M_{87}$  the mass of the  $^{87}\text{Sr}^+$  ion.

Focusing on strontium, corrections beyond the elementary isotope shift, in particular, the mass polarization correction, was estimated from earlier data for helium Rydberg states [163–165] and are expected to be  $\lesssim 1$  MHz and are neglected. Under this assumption, the energies of the  $^{87}\text{Sr}$  Rydberg states should be given by

$$\langle \hat{H}^{87} \rangle = \langle \hat{H}_0^{88}(m_{88}, m_{87}) \rangle + \langle \hat{V}_{\text{hfs}} \rangle \quad (3.25)$$

The values of  $\langle \hat{H}_0^{88}(m_{88}, m_{87}) \rangle$  are easily determined from the Rydberg-Ritz formula

$$\langle \hat{H}^{87} \rangle = \langle \hat{H}_0^{88}(m_{88}, m_{87}) \rangle = E_{\text{ion}}^{87} - \frac{R_{\text{Sr}}^{87}}{(n - \mu_{n,L,S,J})^2} \quad (3.26)$$

with the quantum defect given by \*\* [11, 156, 157] cite just Gallagher and Vaillant paper?

\*\*

$$\mu_{n,L,S,J} = \mu_0 + \frac{\mu_2}{(n - \mu_0^2)^2} + \frac{\mu_4}{(n - \mu_0^2)^4} \quad (3.27)$$

\*\* Use footnote? There's an interesting discussion on how the equation for quantum defect is supposed to be recursive with  $n^* = n - \delta(n^*) = n - \delta_0 - \delta_2/(n - \delta)^2 - \delta_4/(n - \delta)^4 - \dots$  [158] vs. the power-series expansion presented in [156]. \*\*

An important consideration in determining when effects cannot be neglected is when the energy scales become comparable. For strontium, the energy scale of the hyperfine interaction is given by  $a_{5s}$  and, as  $n$  increases this energy scale becomes comparable. As seen in Fig. 3.2, it first becomes comparable to the fine structure splitting, then the singlet-triplet splitting, then the Coulomb splitting. From Fig. 3.2, one would also expect hyperfine mixing to occur between  $n \sim 10$  and  $n \sim 20$  which was indeed observed [143, 144, 151]. Hyperfine mixing was also observed between the  $(5s19d)^1D_2$  and  $(5s19d)^3D_3$  states [166].

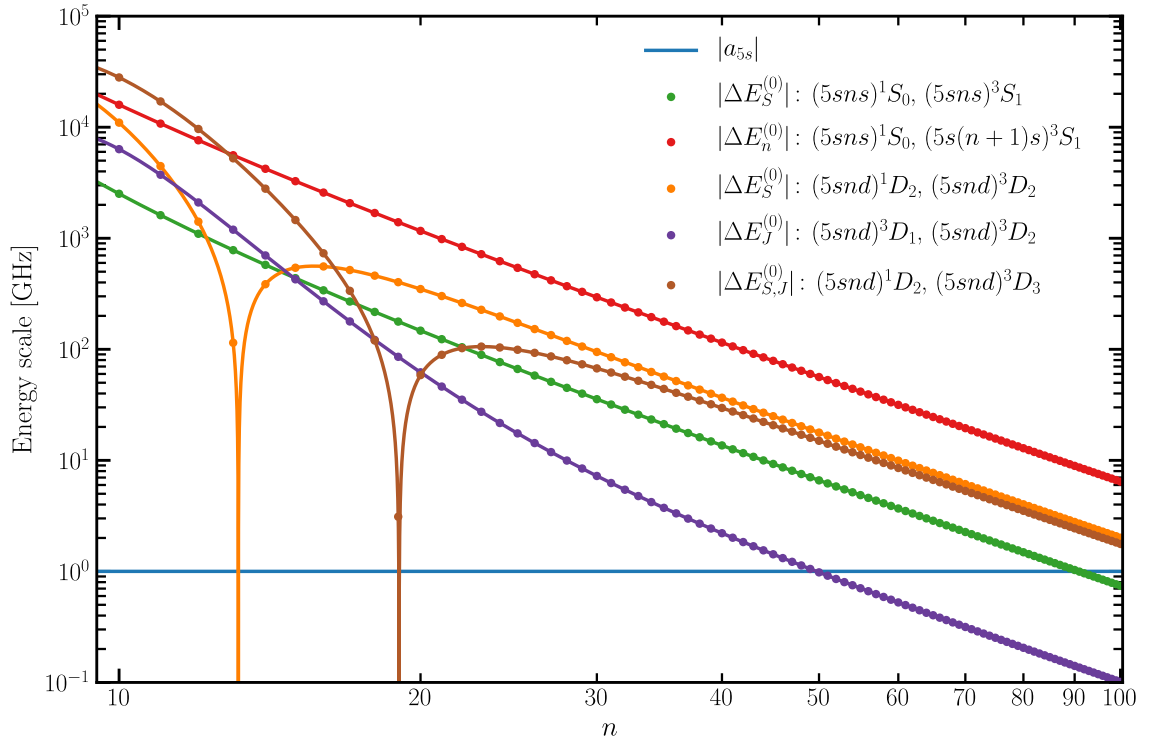


Figure 3.2: The  $n$  scaling of various splittings in  $^{88}\text{Sr}$  calculated using the most recently reported quantum defects and ionization energy [141, 157]. The energy scale of the hyperfine interaction in  $^{87}\text{Sr}$  is approximately constant and is  $|a_{5s}| \approx 1\text{ GHz}$  [150]. The splittings between various states are represented by  $\Delta E_X^{(0)}$  between the given states where  $X = S$  is the singlet-triplet splitting,  $X = J$  is the fine structure splitting, and  $X = n$  is the Coulomb splitting.

In the below, we follow the derivation outlined in [145, 146]. A more detailed derivation is provided in appendix H.3 where it is shown that  $\hat{V}_{\text{hf}}$  only mixes states of the same  $F$ . \*\* I need to actually do the derivation.... \*\*

Assuming there are no perturbing states, a reasonable assumption for  $n \gtrsim 12$  for the both the  $(5sns)^1S_0$  and  $(5sns)^3S_1$  Rydberg series [151], we start with the pure singly-excited singlet  $|^1S_0, F = I\rangle$  and triplet  $|^3S_1, F = I + 1\rangle$ ,  $|^3S_1, F = I\rangle$ , and  $|^3S_1, F = I - 1\rangle$

hyperfine states. Applying  $\hat{V}_{\text{hf}}$  to these basis states gives

$$\hat{V}_{\text{hf}} |^3S_1, F = I + 1\rangle = \frac{1}{2}a_{5s}I |^3S_1, F = I + 1\rangle \quad (3.28)$$

$$\hat{V}_{\text{hf}} |^1S_0, F = I\rangle = \frac{1}{2}a_{5s}\sqrt{I(I+1)} |^3S_1, F = I\rangle \quad (3.29)$$

$$\hat{V}_{\text{hf}} |^3S_1, F = I\rangle = \frac{1}{2}a_{5s} \left( \sqrt{I(I+1)} |^1S_0, F = I\rangle - |^3S_1, F = I\rangle \right) \quad (3.30)$$

$$\hat{V}_{\text{hf}} |^3S_1, F = I - 1\rangle = -\frac{1}{2}a_{5s}(I+1) |^3S_1, F = I - 1\rangle \quad (3.31)$$

From the above, it's apparent that the unmixed states have energy shifts

$$\langle ^3S_1, F = I + 1 | \hat{V}_{\text{hf}} |^3S_1, F = I + 1\rangle = \frac{1}{2}a_{5s}I \approx -2.25 \text{ GHz} \quad (3.32)$$

$$\langle ^3S_1, F = I - 1 | \hat{V}_{\text{hf}} |^3S_1, F = I - 1\rangle = -\frac{1}{2}a_{5s}(I+1) \approx 2.75 \text{ GHz} \quad (3.33)$$

The matrix elements of the mixed  $F = I$  states are

$$\langle ^1S_0, F = I | \hat{V}_{\text{hf}} |^1S_0, F = I\rangle = 0 \quad (3.34)$$

$$\langle ^3S_1, F = I | \hat{V}_{\text{hf}} |^3S_1, F = I\rangle = -\frac{1}{2}a_{5s} \quad (3.35)$$

$$\langle ^3S_1, F = I | \hat{V}_{\text{hf}} |^1S_0, F = I\rangle = \frac{1}{2}a_{5s}\sqrt{I(I+1)} \quad (3.36)$$

you keep doing little bits of the problem...and it is very hard to follow. It is only a 4x4 matrix. That is not that bad. I suggest you just define your basis and write out the matrix of V\_HF.

Therefore  $F = I$  submatrix of the block-diagonal  $\hat{V}_{\text{hf}}$  matrix can be written as

$$\hat{V}_{\text{hf}} = \frac{1}{2}a_{5s} \begin{pmatrix} 0 & \sqrt{I(I+1)} \\ \sqrt{I(I+1)} & -1 \end{pmatrix} \quad (3.37)$$

Diagonalizing the total Hamiltonian  $\hat{H} = \hat{H}_0 + \hat{V}_{\text{hf}}$  gives the eigenenergies

$$E^\pm = \frac{E_1 + E_3}{2} - \frac{1}{4}a_{5s} \pm \frac{1}{2}\sqrt{(E_1 - E_3)^2 + a_{5s}(E_1 - E_3) + a_{5s}^2 \left( I + \frac{1}{2} \right)^2} \quad (3.38)$$

Taking the limit  $a_{5s} \rightarrow 0$  (i.e., no hyperfine interaction), we observe  $E^+ \rightarrow E(^1S_0)$  and  $E^- \rightarrow E(^3S_1)$  meaning  $E^+$  corresponds to the energy of  $|(5sns)^1S_0, F = 9/2\rangle$  and  $E^+$  corresponds to energy of  $|(5sns)^3S_1, F = 9/2\rangle$ .

***n*-mixing**

At higher  $n$ , the hyperfine shift becomes comparable to the splitting between  $n$  and  $n' = n \pm 1$  as seen in Fig. 3.2. Hyperfine-induced  $n$ -mixing was experimentally observed around  $n = 113$  between the  $(5sns)^1S_0, F = 9/2$  and  $(5s(n+1)s)^3S_1, F = 9/2$  states [146].

The derivation above can be extended to incorporate  $n$ -mixing. Using the fact that  $\hat{V}_{\text{hf}}$  only couples states with the same  $F$  and the orthogonality of the radial wave functions for states of same spin multiplet but different  $n$ , the diagonal matrix elements of  $\hat{V}_{\text{hf}}$  for  $(5sns)^3S_1, F = I + 1$  and  $(5sns)^3S_1, F = I - 1$  can be written as

$$\langle (5sn's)^3S_1, F = I + 1 | \hat{V}_{\text{hf}} | (5sns)^3S_1, F = I + 1 \rangle = \frac{1}{2} a_{5s} I \delta_{n,n'} \quad (3.39)$$

$$\langle (5sn's)^3S_1, F = I - 1 | \hat{V}_{\text{hf}} | (5sns)^3S_1, F = I - 1 \rangle = -\frac{1}{2} a_{5s} (I + 1) \delta_{n,n'} \quad (3.40)$$

The off-diagonal elements vanish between these states because they remain uncoupled.

\*\*\*\*\* I don't think I can do this "expansion"... I think I want to just calculate matrix elements between  $n$  and  $n'$  states \*\*\*\*\* On the other hand, because  $\hat{V}_{\text{hf}}$  mixes the  $(5sns)^1S_0, F = I$  and  $(5sns)^3S_1, F = I$  states, we can write

$$|(5sns)^1S_0, F = I\rangle = |(n)^1S_0, F = I\rangle + \sum_{n'} |(n')^3S_1, F = I\rangle \quad (3.41)$$

$$|(5sns)^3S_1, F = I\rangle = |(n)^3S_1, F = I\rangle + \sum_{n'} |(n')^1S_0, F = I\rangle \quad (3.42)$$

where  $(n)^1S_0, F = I$  and  $(n)^3S_1, F = I$  represent pure singly-excited singlet and triplet  $F = I$  states (recalling that the radial wave functions are orthogonal for  $n \neq n'$  for states in the same spin multiplet). Calculating the matrix elements of  $\hat{V}_{\text{hf}}$  between  $(5sns)^1S_0, F = I$  and  $(5sns)^3S_1, F = I$  gives

$$\langle (5sn's)^1S_0, F = I | \hat{V}_{\text{hf}} | (5sns)^1S_0, F = I \rangle = 0 \quad (3.43)$$

you lost me here. How does 3.41 and 3.42 lead to this?

there must be expansion coefficients?

$$\langle (5sn's)^3S_1, F = I | \hat{V}_{\text{hf}} | (5sns)^3S_1, F = I \rangle = -\frac{1}{2} a_{5s} \delta_{n,n'} \quad (3.44)$$

The off-diagonal elements can be expressed as

$$\begin{aligned} \langle (5sn's)^1S_0, F = I | \hat{V}_{\text{hf}} | (5sns)^3S_1, F = I \rangle &= -\frac{1}{2}a_{5s}(\text{stuff to finish deriving}) \\ &= -\frac{1}{2}a_{5s}\sqrt{I(I+1)}O_{n,n'} \end{aligned} \quad (3.45)$$

where  $O_{n,n'}$  is the overlap between the singlet and triplet radial wave functions which can be estimated semiclassically [146, 167]

$$O_{n_1,n_2} = \langle n_1^* | n_2^* \rangle = (-1)^{n_2-n_1} \frac{2\sqrt{n_1^* n_2^*}}{n_1^* + n_2^*} \frac{\sin[\pi(n_2^* - n_1^*)]}{\pi(n_2^* - n_1^*)} \quad (3.46)$$

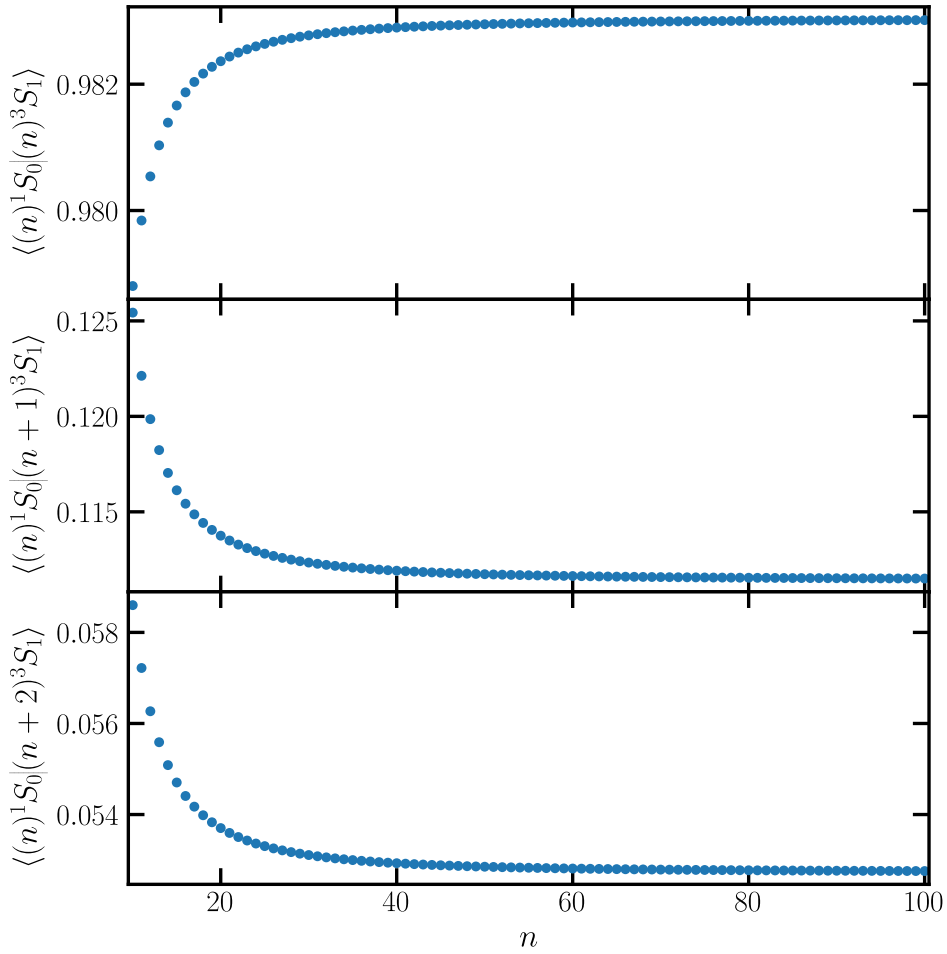


Figure 3.3: \*\* FIX FIGURE Y-AXIS LABELS \*\*. Semiclassical estimation of the radial wave function overlap [167] between  $(n)^1S_0$  and  $(n')^3S_1$  states ( $O_{n,n'}$ ) for  $n' = n, n+1, n+2$ .

Between adjacent  $n$  (i.e., for  $n_2 = n_1 + 1$ ) and  $\delta_2 \neq \delta_1$ , the approximation reduces to

$$O_{n_1,n_1+1} = \langle n_1^* | (n_1 + 1)^* \rangle = -\frac{2\sqrt{n_1^*(n_1 + 1)^*}}{n_1^* + (n_1 + 1)^*} \frac{\sin[\pi((n_1 + 1)^* - n_1^*)]}{\pi((n_1 + 1)^* - n_1^*)} \quad (3.47)$$

Since the  $(5sns)^1S_0, F = 9/2$  state is always higher in energy than the  $(5sns)^3S_1, F = 9/2$ , they should cross when  $n_1$  corresponds to the singlet state and  $n_2 = n_1 + 1$  corresponds to the triplet state. Using the quantum defects from [157], we expect  $\langle n_1^* | (n_1 + 1)^* \rangle \approx 0.1$  and  $\langle n_1^* | (n_1 + 1)^* \rangle \approx 0.05$  so we only include  $n$  and  $n + 1$  mixing.

As seen in Fig. 3.3, the strongest  $n$ -mixing occurs for  $\Delta n = \pm 1$  with  $O_{n,n'} \approx 0.1$  and quickly drops off for larger  $\Delta n$ .

\*\*\*\*\*

$$\langle (n) ^1S_0 | \hat{V}_{\text{hf}} | (n + 1) ^3S_1 \rangle = (\langle n_1^* | ^1S_0 |) \hat{V}_{\text{hf}} (^3S_1 | | (n + 1)_1^* |) \quad (3.48)$$

$$= \langle n_1^* | (n + 1)_1^* | \langle ^1S_0 | \hat{V}_{\text{hf}} | ^3S_1 \rangle \quad (3.49)$$

$$\langle (n) ^1S_0 | \hat{V}_{\text{hf}} | (n + 1) ^3S_1 \rangle = \langle (n) ^1S_0 | \left[ \hat{V}_{\text{hf}} | (n + 1) ^3S_1 \rangle \right] \quad (3.50)$$

$$\neq \frac{1}{2} a_{5s} \langle (n) ^1S_0 | \left[ \sqrt{I(I+1)} | (n + 1) ^1S_0 \rangle - | (n + 1) ^3S_1 \rangle \right] \quad (3.51)$$

$$= \frac{1}{2} a_{5s} \sqrt{I(I+1)} \langle (n) ^1S_0 | (n + 1) ^1S_0 \rangle \\ - \frac{1}{2} a_{5s} \langle (n) ^1S_0 | (n + 1) ^3S_1 \rangle \quad (3.52)$$

$$= \frac{1}{2} a_{5s} \sqrt{I(I+1)} \langle n_1^* | (n + 1)_1^* | \langle ^1S_0 | ^1S_0 \rangle \\ - \frac{1}{2} a_{5s} \langle n_1^* | (n + 1)_1^* | \langle ^1S_0 | ^3S_1 \rangle \quad (3.53)$$

$$= 0 \quad (3.54)$$

$$\langle (n) ^1S_0 | \hat{V}_{\text{hf}} \left( \sum_{n'} | (n') ^3S_1 \rangle \right) = \dots \quad (3.55)$$

\*\*\*\*\*

### 3.2.2 Singly Excited $D$ states

Even before including hyperfine interactions, the spin-orbit interactions leads to a breakdown of  $LS$  coupling and mixes the  ${}^1D_2$  and  ${}^3D_2$  states and is especially strong around  $n = 15$  where they swap singlet and triplet character [133, 143, 144, 151, 162]. To account for this mixing, the eigenstates  $(5sns){}^1D_2$  and  $(5sns){}^3D_2$  of the  $H_0(88, m_{87})$  are expanded as

$$|(5sns){}^1D_2\rangle = \cos\theta |(n){}^1D_2\rangle + \sin\theta |(n){}^3D_2\rangle \quad (3.56)$$

$$|(5sns){}^3D_2\rangle = -\sin\theta |(n){}^1D_2\rangle + \cos\theta |(n){}^3D_2\rangle \quad (3.57)$$

where  $\theta$  is the mixing angle [168] of the pure singlet  $|(n){}^1D_2\rangle$  and triplet  $|(n){}^3D_2\rangle$  states.

\*\*\* For higher  $n$ , the singlet-triplet mixing of the  ${}^1D_2$  and  ${}^3D_2$  states becomes nearly  $n$  independent as evidenced by their quantum defects [141, 157]. \*\* Calculations using a two-active-electron (TAE) model [169, 170] estimates that converges towards  $\theta \sim -0.16$  for high  $n$ . \*\* Where does  $\theta \sim -0.14$  come from? \*\*

\*\* See [162] for a calculation of mixing coefficients? \*\*

Calculating the hyperfine matrix elements of the  $D$  states is quite a bit more challenging than for the  $S$  states. In total, there are 20 singly excited  $D$  states ( $(5snd){}^1D_2$ ,  $(5snd){}^3D_1$ ,  $(5snd){}^3D_2$ , and  $(5snd){}^3D_3$ ) which each have  $2I + 1 = 10$  nuclear spin states. The matrix elements of  $\hat{V}_{\text{hfs}}$  can be evaluated analytically [162, 168, 171].

Due to these interactions, it's not clear how to assign the different states since  $S$  and  $J$  are no longer good quantum numbers. Instead, the state assignments were made by evaluating the overlap of the hyperfine-mixed states with the unperturbed  $(5sns){}^{2S+1}D_J$  state. \*\* CLARIFY I need to check with Shuhei that I'm understanding this correctly \*\*

Chapter 3 is very long and complicated....THere are some possibilities for making it better.  
 For starters, it would be very helpful to have a 30,000 foot section...give all the transitions for one or two n and talk about the structure..."we see singlet s and triplet s....hyperfine gives these splittings which are large or small, etc."  
 That would really help.  
 THat would allow you to give context to discussion of the theory...for example, when you talk about the hyperfine splitting and singlet triplet mixing, you can say "as we see in figure xx, the splitting is big or the mixing is small..."  
 I think it would work a little better to talk about the experiment and measurements first...give the 30,000 foot view. Then say "to fit the spectrum and get physical parameters, we need theory..." Then discuss the agreement of fit and expt and the derived constants like quantum defects. You could even make the theory and fit a separate chapter, but that is probably less important as long as you clearly separate the parts and give good transitions.  
 Right now, you make no intuitive contact between the theory and the observations, which is not so good..

## Experimental Method

A schematic diagram of the present experimental arrangement is presented in Fig. 3.4. cooling and trapping of strontium was described previously in this thesis so it will

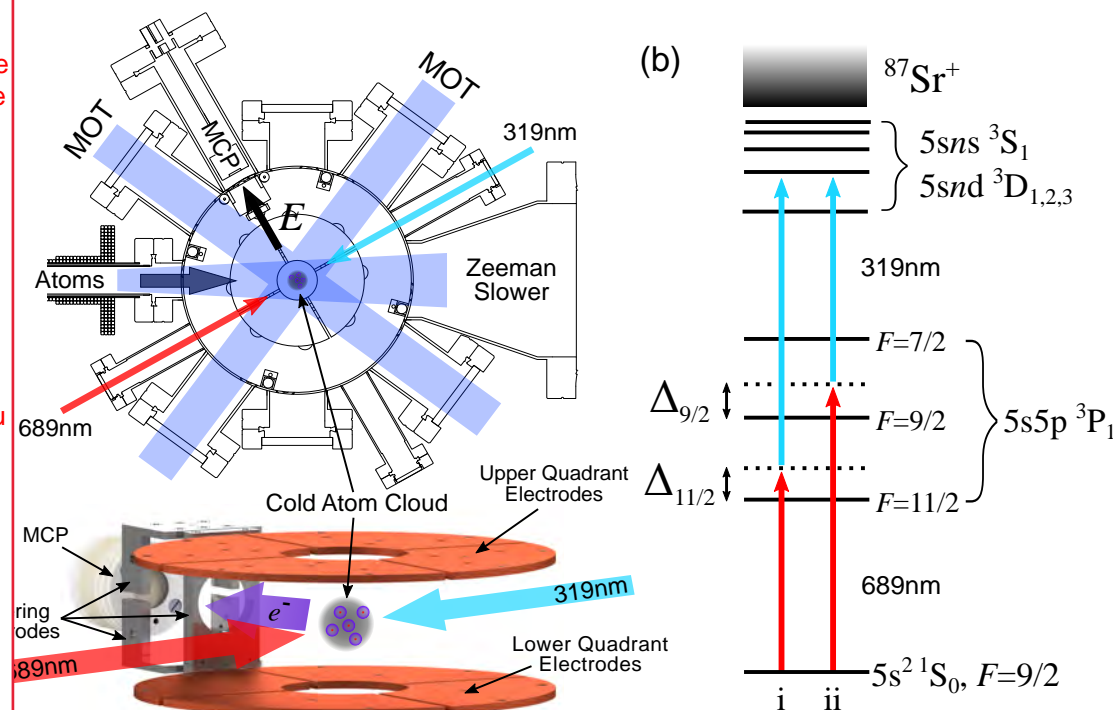


Figure 3.4: (a) Diagram of the experimental arrangement showing the 461 nm cool-beams and the counterpropagating 689 nm and 319 nm Rydberg excitation lasers. Two-photon excitation schemes utilizing either the (i)  $(5s5p) \ ^3P_1, F = 11/2$  or  $(5s5p) \ ^3P_1, F = 9/2$  intermediate states. The detunings relative to these intermediate states are fixed at  $\Delta_{11/2} \approx 12$  MHz and  $\Delta_{9/2} \approx 36$  MHz. (c) Arrangement of the electrodes for ionizing Rydberg atoms and guiding the electrons towards the MCP detector.

be briefly covered here. Following the standard procedure for laser cooling strontium, start from a Zeeman slowed atomic beam with the Zeeman laser tuned to  $^1S_0 \rightarrow ^1P_1$  resonance in  $^{87}\text{Sr}$ . The slowed atoms are then captured by a blue MOT operating on the  $^1S_0 \rightarrow ^3P_1$  transition which traps and cools the atoms to  $\sim 2$  mK. Further cooling is achieved via a narrow-line red MOT driving the  $^1S_0 \rightarrow ^3P_1$  transition. Approximately  $1 \times 10^6$  atoms  $\sim 2 \mu\text{K}$  are captured and cooled before turning off all trapping fields for spectroscopy measurements.

Rydberg atoms are created by two-photon excitation using counterpropagating cross-linearly polarized 689 nm and 319 nm excitation lasers which drive transitions to the  $(5sns)^3S_1$  and  $(5snd)^3D_{1,2,3}$  Rydberg levels via the intermediate  $(5s5p)^3P_1, F = 9/2$  or  $F = 11/2$  states. These intermediate states were selected to take advantage of selection rules to aid in identifying the Rydberg hyperfine states populated. The typical detunings of the 689 nm laser were fixed at  $\Delta_{9/2} \approx 36$  MHz and  $\Delta_{11/2} \approx 12$  MHz relative to the intermediate states. During excitation, the 319 nm laser was kept on while the 689 nm laser was chopped into  $(10 - 20)$   $\mu$ s-long pulses to generate temporally localized groups of Rydberg atoms. The number of Rydberg atoms produced by each pulse was determined by using the electrodes in Fig. 3.4 to generate a ramped electric field sufficient to ionize the Rydberg atoms with the resulting electrons directed towards, and detected by, a micro-channel plate (MCP) whose output was fed into a multichannel scalar (MCS). Typically 100 – 500 measurement cycles were performed before loading a new sample and changing the 319 nm laser frequency. Spectroscopic measurements at high  $n$  using  $^{84}\text{Sr}$  showed that the stray fields in the trapping region were less than  $10\text{ mV cm}^{-1}$  so any resultant Stark shifts should be at most a few megahertz even at  $n \sim 90$ .

The 319 nm radiation was generated by frequency doubling the output of a 638 nm optical parametric oscillator (OPO). A sample of the output is sent through a broadband fiber electro-optic modulator (fEOM) from which one of the tunable sidebands was locked to a transfer cavity, allowing the 319 nm laser to be scanned over multiple gigahertz. The transfer cavity was stabilized using a 689 nm laser locked to the  $(5s^2)^1S_0 \rightarrow (5s5p)^3P_1$  transition in  $^{88}\text{Sr}$ . The linewidth of the 319 nm laser is estimated to be  $\lesssim 500$  kHz based on the narrowest observed spectroscopic features. The Rydberg state energies are determined by measuring the 638 nm frequency with an EXFO WA-1500 wavemeter and is resolution-limited to about  $\approx 60$  MHz. Relative measurements of line splittings can be obtained to kilohertz-level accuracies when scanning within a single free spectral range (FSR) of the transfer cavity and to megahertz-level accuracies when piecing together scans over successive

didn't you say this in  
chapter 2?

FSR<sup>52</sup>.

### 3.3.1 Calibrating the EXFO WA-1500 Wavemeter

All light used in the calibration measurements were delivered to the EXFO WA-1500 using a single mode fiber<sup>53</sup>. We had previously used a multimode fiber but found that the wavemeter readings were inconsistent, likely due to the speckle pattern or slight beam pointing deviations from the output of the multimode fiber. Switching to a single mode fiber alleviated these issue and we were able to consistently obtain resolution-limited measurements of the wavenumber with a statistical uncertainty of about  $\sigma_{\text{stat}} = \pm 15 \text{ MHz}$  wavelengths we measured. Since the 319 nm light is generated by frequency-doubling 638 nm, the statistical uncertainty is approximately doubled as well  $\sigma_{\text{stat}} = \pm 30 \text{ MHz}$

it is confusing to use  
the same symbol for  
two different things. If  
you are just defining  
the uncertainty, do you  
need a symbol?

Since we rely on the wavemeter to determine the absolute energy of the 638 nm photon, we also needed to characterize potential systematics. We initially attempted to perform Doppler-free spectroscopy of molecular iodine ( $^{127}\text{I}_2$ ) using the  $P65$  (7–4) line at  $15\,672\,517\,398(25) \text{ cm}^{-1}$  [172] which is near the wavelength required to excite the  $(5s40s)^3S_1$  Rydberg state. We didn't have much luck observing narrow Doppler-free signals scanning the 638 nm laser through a ~~our~~ iodine cell using a simple saturated absorption setup<sup>54</sup>. A longer cell and a more sensitive detection method may be necessary since most  $^{127}\text{I}_2$  spectroscopy setups in this wavelength range used cells longer than 30 cm and some sort of modulation spectroscopy (e.g., [172, 174, 175]).

Although the iodine spectroscopy didn't work out, we were able to calibrate the wavemeter by measuring wavelengths of lasers lock to atomic transitions in  $^{88}\text{Sr}$  (689 nm) and  $^6\text{Li}$  (671 nm and 646 nm). The 689 nm reference comes from the red master laser locked to the  $^1S_0 \rightarrow ^3P_1$  in  $^{88}\text{Sr}$ . Ya-Ting Chang, Danyel Cavazos, and Dr. Randy Hulet were kind

<sup>52</sup>We have since developed a method that can provide kilohertz-level accuracies over successive FSRs without needing an accurate measurement of the FSR.

<sup>53</sup>Thorlabs SM600 FC/PC single mode fiber.

<sup>54</sup>This matches similar experiences according to Jason Nguyen and Henry Luo in the Hulet lab when they were looking to use an iodine cell to lock their 646 nm laser for a  $^6\text{Li}$  UV MOT [173].

enough to let us run a fiber between the Killian and Hulet labs in order to measure the wavelengths of their 671 nm and 646 nm lasers for laser cooling  ${}^6\text{Li}$ . The 671 nm is used for a standard  $D_2$  MOT while the 646 nm is frequency doubled to 323 nm for a UV MOT [173]. The wavemeter measurements of those three wavelengths were performed within about 2 h to reduce sensitivity to environmental changes and are presented in Tab. 3.1. These mea-

Table 3.1: Values used to calibrate the WA-1500 on a single day (2018/03/09) within about 2 h. The value of the 689 nm transition in  ${}^{88}\text{Sr}$  [106, 176]. The values of the 671 nm and 323 nm (646 nm) transitions in  ${}^6\text{Li}$  were taken from [177–179].

$\lambda$ [nm]	Atom	Transition	Reference [ $\text{cm}^{-1}$ ]	Measured [ $\text{cm}^{-1}$ ]
689	${}^{88}\text{Sr}$	$(5s^2)^1S_0 \rightarrow (5s5p)^3P_1$	14 504.338 241 59(33)	14 504.342 24(35)
671	${}^6\text{Li}$	$(2s)^2S_{1/2}, F = 3/2 \rightarrow (2p)^2P_{3/2}$	14 903.629 524 2(7)	14 903.633 91(33)
323 (646)	${}^6\text{Li}$	$(2s)^2S_{1/2}, F = 3/2 \rightarrow (3p)^2P_{3/2}$	30 925.1703(10) (15 462.5851(5))	30 925.1792(10) (15 462.5896(5))

surements were used to calculate the frequency offset  $\delta(\lambda) = \nu_{\text{measured}} - \nu_{\text{reference}}$  between the measured and reported values and is plotted in Fig. 3.5. A linear fit yields a correction

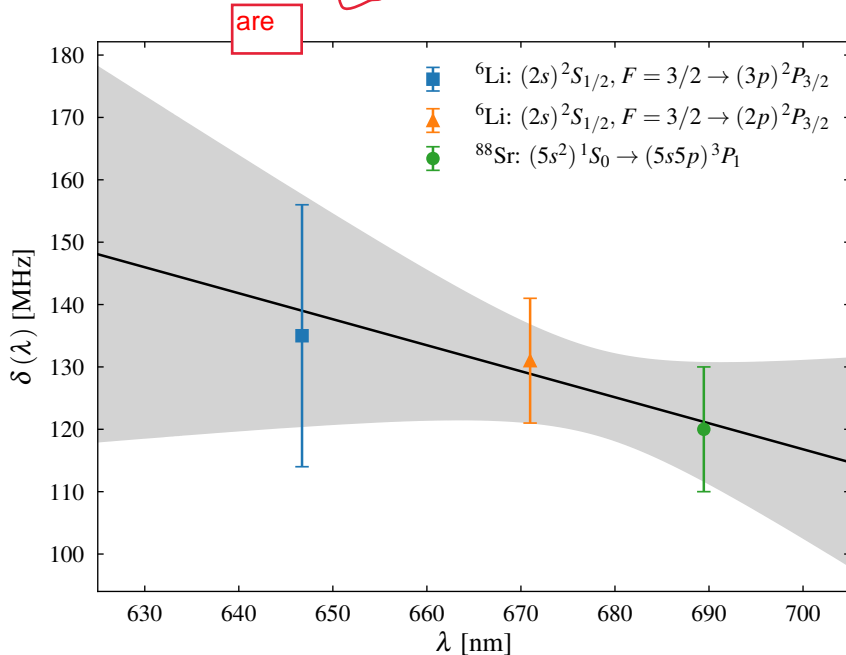


Figure 3.5: Wavelength dependence of the offset between the measured and published transition frequencies used to calibrate the wavemeter  $\delta(\lambda) = \nu_{\text{measured}} - \nu_{\text{reference}}$ . The black line shows the linear fit used to obtain the offset at 638 nm with the shaded region representing the uncertainty in the wavemeter calibration obtained from Monte Carlo simulations.

of  $\approx 140$  MHz at 638 nm. In an attempt to estimate the systematic uncertainty in this calibration factor, a Monte Carlo sampling was adopted in which linear fits to points drawn at random from a Gaussian distributions appropriate to each point in the calibration were repeated, resulting in a systematic uncertainty of about  $\sigma_{\text{sys}} = \pm 25$  MHz ( $\sigma_{\text{sys}} = \pm 50$  MHz) at 638 nm (319 nm).

is this the object  
modified by the  
clause? I am not sure.

To check for drifts in the wavemeter calibration, each 638 nm wavelength measurement was followed by a reference measurement of the 689 nm master laser. As shown in Fig. 3.6, the day-to-day variations were relatively small compared to the wavemeter's systematic uncertainty which we suspect are due to changes in environmental conditions (e.g., temperature, humidity, pressure). These effects were mitigated by using the 689 nm reference

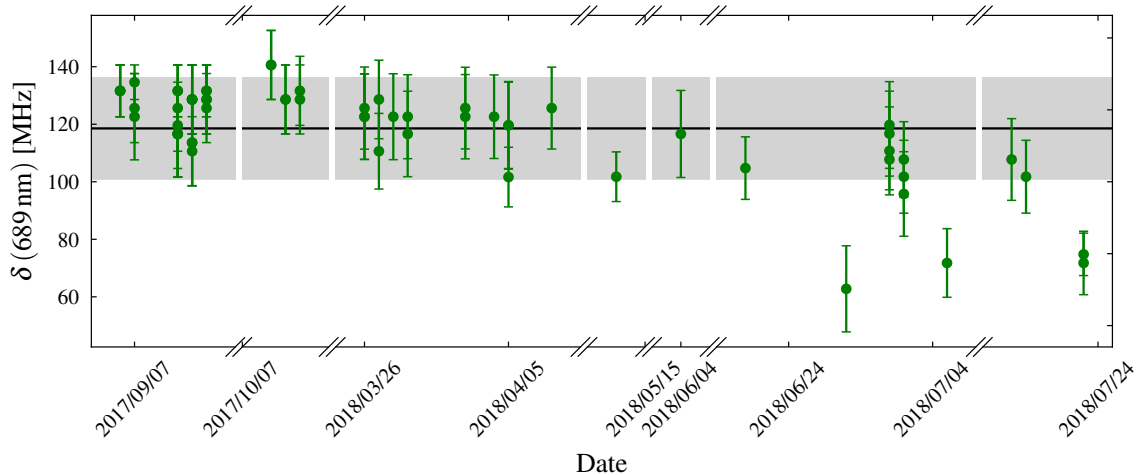


Figure 3.6: Compiled measurements of the wavemeter offset of the 689 nm transition. The data comes from the 689 nm reference measurements paired with each 638 nm measurement.

measurement paired with each 638 nm measurement to remove the day-to-day wavemeter offset before using  $\delta(\lambda)$  to calculate the offset at 638 nm.

### 3.4 Results and Discussion

Table 3.2 lists the measured term energies for multiple  $(5sns)^{1,3}S$  Rydberg states for  $30 \lesssim n \lesssim 99$  including their theoretical predictions by diagonalization of the rescaled Hamil-

Discuss the spectrum before referring to extracted quantum defects. Otherwise, it is too many tables and figures in one place without any discussion.

tonian \*\*\* CITE EQUATION \*\*\*. Figures 3.7 and 3.8 show the quantum defects calculated with the Rydberg-Ritz formula [157] from the measured  $^{88}\text{Sr}$  term energies together with those extracted from the current measurements in  $^{87}\text{Sr}$ . For  $^{88}\text{Sr}$ , the most recent value of the ionization limit was used along with the mass-scaled Rydberg constant<sup>55</sup>. For  $^{87}\text{Sr}$ , along with using the appropriately mass-corrected Rydberg constant and \*\*\*\* ionization energy \*\*\*\*, the hyperfine shifts for each state was calculated and subtracted from the measured term energies to obtain the quantum defect for an effective  $I = 0$  atom.

save this for later

Table 3.2: Experimentally measured and calculated energies of selected  $(5sns)^1S_0$  and  $(5sns)^3S_1$  states in  $^{87}\text{Sr}$ .  $\Delta E_{\text{expt}}$  and  $\Delta E_{\text{theor}}$  are the measured and predicted separations from the  $(5sns)^3S_1, F = 11/2$  state of the same  $n$  which is used as a reference. The uncertainties shown include both the statistical and systematic uncertainties in the wavemeter calibration.

Series	$n$	Term	$F$	$E_{\text{expt}}$ [cm $^{-1}$ ]	$\Delta E_{\text{expt}}$ [GHz]	$E_{\text{theor}}$ [cm $^{-1}$ ]	$\Delta E_{\text{theor}}$ [GHz]
5sns	40	$^1S_0$	9/2	45 850.8762(21)	16.35(8)	45 850.8702	16.22
	60			45 898.1444(22)	7.28(9)	45 898.1421	7.26
	72			45 909.0252(20)	6.10(9)	45 909.0240	6.1
	74			45 910.3230(21)	5.98(9)	45 910.3211	5.99
	76			45 911.5148(20)	5.91(8)	45 911.5127	5.89
	77			45 912.0738(20)	5.84(9)	45 912.0725	5.85
	78			45 912.6114(20)		45 912.6100	5.81
	82			45 914.5606(22)	5.66(9)	45 914.5589	5.67
	86			45 916.2336(21)	5.56(8)	45 916.2321	5.56
	90			45 917.6802(19)	5.46(8)	45 917.6791	5.47
	94			45 918.9402(19)	5.40(8)	45 918.9388	5.39
	98			45 920.0438(22)	5.325(5)	45 920.0423	5.327
5sns	40	$^3S_1$	7/2	45 850.4974(21)	4.99(8)	45 850.4960	5.0
	60			45 898.0688(21)	5.02(8)	45 898.0668	5.0
5sns	40	$^3S_1$	9/2	45 850.4078(21)	2.31(8)	45 850.4061	2.31
	50			45 881.7138(22)	1.88(9)	45 881.7119	1.89
	72			45 908.8546(21)	0.99(9)	45 908.8528	0.97
	74			45 910.1518(22)	0.85(9)	45 910.1516	0.91
	76			45 911.3460(19)	0.85(8)	45 911.3445	0.85
	77			45 911.9068(21)	0.83(9)	45 911.9049	0.83
	78			45 912.4444(19)		45 912.4429	0.8
	82			45 914.3958(21)	0.72(9)	45 914.3935	0.71
	86			45 916.0696(21)	0.64(8)	45 916.0677	0.63

Continued on next page.

<sup>55</sup>  $E_{\text{ion}}^{88} = 45 932.200\ 24(33) \text{ cm}^{-1}$  [141] and  $R_{\text{Sr}}^{88} = 109\ 736.630\ 867\ 5(7) \text{ cm}^{-1}$ . See appendix C.4.

Table 3.2 – *Continued from previous page.*

Series	$n$	Term	$F$	$E_{\text{expt}}$ [cm $^{-1}$ ]	$\Delta E_{\text{expt}}$ [GHz]	$E_{\text{theor}}$ [cm $^{-1}$ ]	$\Delta E_{\text{theor}}$ [GHz]
	90			45 917.5172(21)	0.57(8)	45 917.5155	0.56
	94			45 918.7774(22)	0.52(9)	45 918.7759	0.51
	98			45 919.8816(22)	0.463 02(7)	45 919.8800	0.461 64
$5sns$	30	$^3S_1$	11/2	45 777.3637(20)		45 777.3621	
	31			45 788.3644(21)		45 788.3624	
	32			45 798.2325(22)		45 798.2302	
	33			45 807.1179(19)		45 807.1158	
	34			45 815.1469(21)		45 815.1452	
	35			45 822.4253(21)		45 822.4252	
	36			45 829.0469(20)		45 829.0460	
	37			45 835.0865(21)		45 835.0851	
	38			45 840.6098(14)		45 840.6085	
	39			45 845.6759(22)		45 845.6734	
	40			45 850.3308(15)		45 850.3291	
	42			45 858.5807(21)		45 858.5793	
	43			45 862.2455(20)		45 862.2439	
	44			45 865.6435(21)		45 865.6413	
	45			45 868.7988(15)		45 868.7968	
	49			45 879.4140(19)		45 879.4124	
	50			45 881.6510(21)		45 881.6488	
	55			45 890.9526(20)		45 890.9511	
	60			45 897.9014(19)		45 897.9000	
	65			45 903.2294(19)		45 903.2272	
	72			45 908.8216(22)		45 908.8205	
	74			45 910.1236(22)		45 910.1213	
	76			45 911.3178(19)		45 911.3161	
	77			45 911.8790(21)		45 911.8774	
	82			45 914.3718(22)		45 914.3699	
	86			45 916.0482(19)		45 916.0467	
	90			45 917.4982(19)		45 917.4967	
	94			45 918.7600(21)		45 918.7590	
	98			45 919.8662(22)		45 919.8646	
	99			45 920.1210(22)		45 920.1196	

Figures 3.9 to 3.11 show the positions of the measured  $(5snd)^3D$  spectral lines near  $n = 50, 60, 97$  and  $98$  relative to the energy of the  $(5sns)^3S_1, F = 11/2$  state. The corresponding term values are listed in Tab. 3.3 along with their theoretical predictions. The  $n = 50$  and  $60$  states were excited via the intermediate  $(5s5p)^3P_1, F = 9/2$  state (scheme (ii)), allowing the creation of  $F = 7/2, 9/2$  and  $11/2$  Rydberg states. The  $n = 97$  and  $98$

did you do it this way in the PRA. It is confusing....splittings should be between two states, but they are listed on a single line. So it is ambiguous as to which splitting this refers to. You could use a bracket and locate the splitting between the lines corresponding to the two levels in question.

Table 3.3: Comparison of measured and calculated positions of  $(5s\text{nd})^3D_{1,2,3}$  lines at 50, 60 and  $\sim 98$ . The splittings  $\Delta E_{\text{expt}}$  between those lines that could be measured in a single FSR scan of the 319 nm laser frequency (delineated by the horizontal line at  $n \sim 98$ , where neighboring scans could be accurately patched together are included) with the corresponding theoretical predictions. For the  $n = 98\text{-}99$  scan, all differences are referenced to the  $(5s\text{ns})^3S_1, F = 11/2$  level.

Series	$n$	Term	$F$	$E_{\text{expt}}$ [cm $^{-1}$ ]	$\Delta E_{\text{expt}}$ [MHz]	$E_{\text{theor}}$ [cm $^{-1}$ ]	$\Delta E_{\text{theor}}$ [MHz]
$5s\text{nd}$	50	$^3D_1$	7/2	45 883.1440(22)	-295.60(7)	45 883.1414	299.01
	50	$^3D_1$	9/2	45 883.1538(22)	0	45 883.1514	299.01
	50	$^3D_2$	11/2	45 883.1685(22)	439.39(7)	45 883.1662	443.71
$5s\text{nd}$	50	$^3D_2$	7/2	45 883.2882(21)	0	45 883.2855	0
	50	$^3D_2$	9/2	45 883.2922(21)	118.91(7)	45 883.2893	114.7
	50	$^3D_1$	11/2	45 883.2972(21)	269.12(7)	45 883.2942	260.55
$5s\text{nd}$	50	$^3D_3$	11/2	45 883.3849(22)	-890.64(7)	45 883.3814	-890.22
	50	$^3D_3$	9/2	45 883.4146(22)	0	45 883.4111	0
$5s\text{nd}$	50	$^3D_3$	7/2	45 883.4374(22)		45 883.4339	
$5s\text{nd}$	60	$^3D_1$	7/2	45 898.7367(21)	-183.64(7)	45 898.7347	-178.89
	60	$^3D_1$	9/2	45 898.7428(21)	0	45 898.7407	0
	60	$^3D_2$	11/2	45 898.7521(21)	277.34(7)	45 898.7497	270.37
$5s\text{nd}$	60	$^3D_2$	7/2	45 898.8568(22)	-79.40(7)	45 898.8544	-72.67
	60	$^3D_2$	9/2	45 898.8594(22)	0	45 898.8569	0
	60	$^3D_3$	11/2	45 898.8618(22)	71.37(7)	45 898.8588	58.8
$5s\text{nd}$	60	$^3D_1$	11/2	45 898.9223(22)	-626.40(7)	45 898.9197	-609.77
	60	$^3D_3$	9/2	45 898.9432(22)	0	45 898.9400	0
	60	$^3D_3$	7/2	45 898.9608(22)	526.18(7)	45 898.9573	517.37
$5s\text{ns}$	98	$^3S_1$	11/2	45 919.8662(22)	0	45 919.8646	0
	98	$^3S_1$	9/2	45 919.8816(22)	463.02(7)	45 919.8800	461.64
$5s\text{nd}$	97	$^3D_1$	11/2	45 919.9565(22)	2707.6(35)	45 919.9552	2716.6
	97	$^3D_2$	9/2	45 919.9593(22)	2792.4(35)	45 919.9579	2796.2
	97	$^1D_2$	9/2	45 919.9896(22)	3701(4)	45 919.9879	3697
	97	$^1D_2$	11/2	45 919.9925(22)	3785(4)	45 919.9909	3786
	97	$^1D_2$	13/2	45 919.9946(22)	3850(4)	45 919.9933	3857
$5s\text{ns}$	98	$^1S_0$	9/2	45 920.0438(22)	5325(5)	45 920.0423	5327
$5s\text{nd}$	98	$^3D_1$	9/2	45 920.0474(22)	5432(5)	45 920.0460	5439
	98	$^3D_2$	11/2	45 920.0501(22)	5512(5)	45 920.0485	5514
	98	$^3D_2$	13/2	45 920.0544(22)	5641(5)	45 920.0526	5636
	98	$^3D_3$	13/2	45 920.0916(22)	6756(6)	45 920.0901	6761
	98	$^3D_3$	11/2	45 920.0956(22)	6877(6)	45 920.0943	6886
$5s\text{ns}$	98	$^3D_3$	9/2	45 920.0982(22)	6954(6)	45 920.0971	6970
	99	$^3S_1$	11/2	45 920.1210(22)	7639(6)	45 920.1196	7643

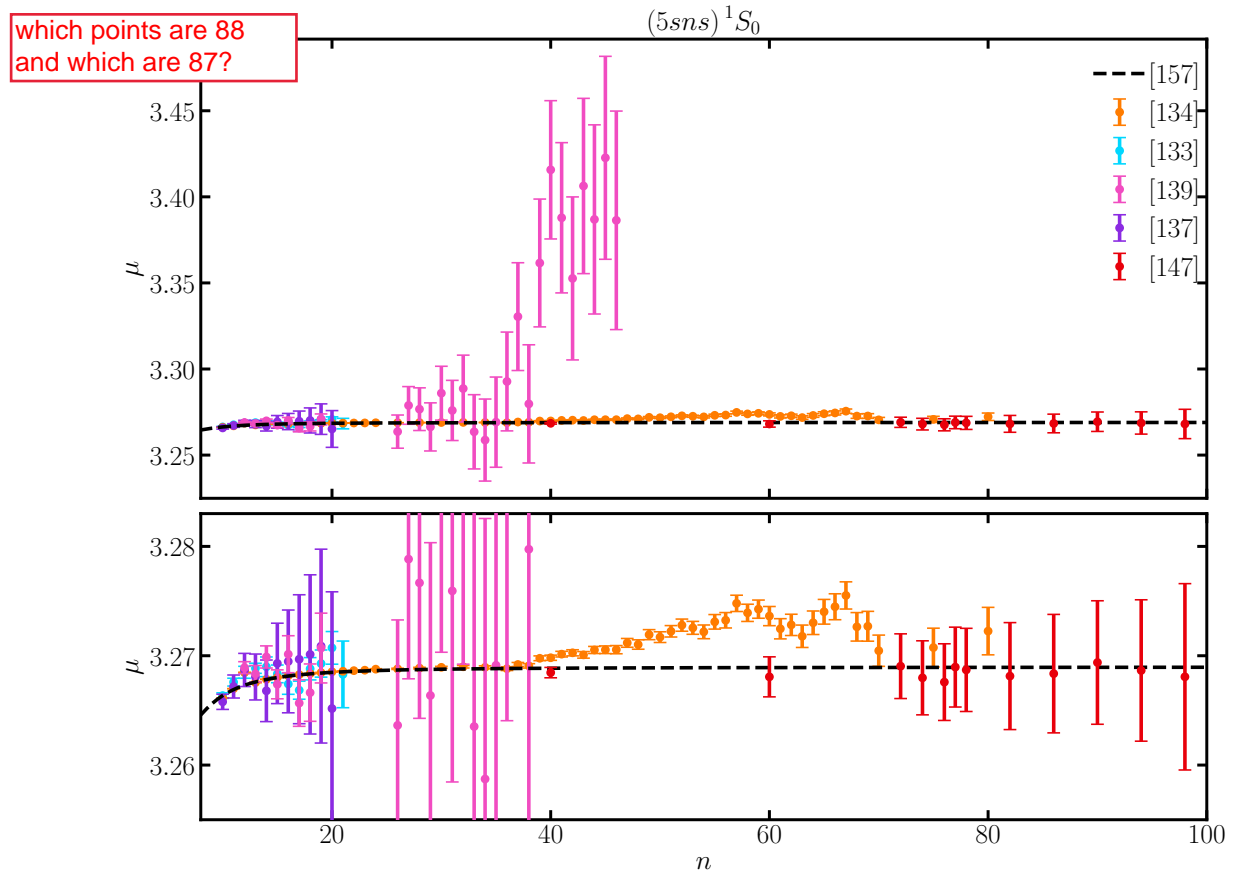


Figure 3.7: Quantum defects for the  $(5sns)^1S_0$  Rydberg series. For  $^{88}\text{Sr}$ , the quantum defects were calculated from the term energies reported in [133, 134, 137, 139]. The quantum defects from the  $^{87}\text{Sr}$  data was extracted after removing the hyperfine shift.

states were excited via the intermediate  $(5s5p)^3P_1, F = 11/2$  state (scheme (i)), leading to the excitation of states with  $F = 9/2, 11/2$  and  $13/2$ . A theoretical fit to the data is also shown in Figs. 3.9 to 3.11 which was determined by varying the quantum defects of the  $(5snd)^3D_{1,2,3}$  series until the best agreement with the measured energies was obtained (see Tab. 3.4). Since the measured quantum defects of the  $(5snd)^1D_2$  series in  $^{88}\text{Sr}$  was available up to  $n = 84$  [134], the quantum defects from [157] were used for those states.

\*\*\*\*\*

\*\*\*\*\*

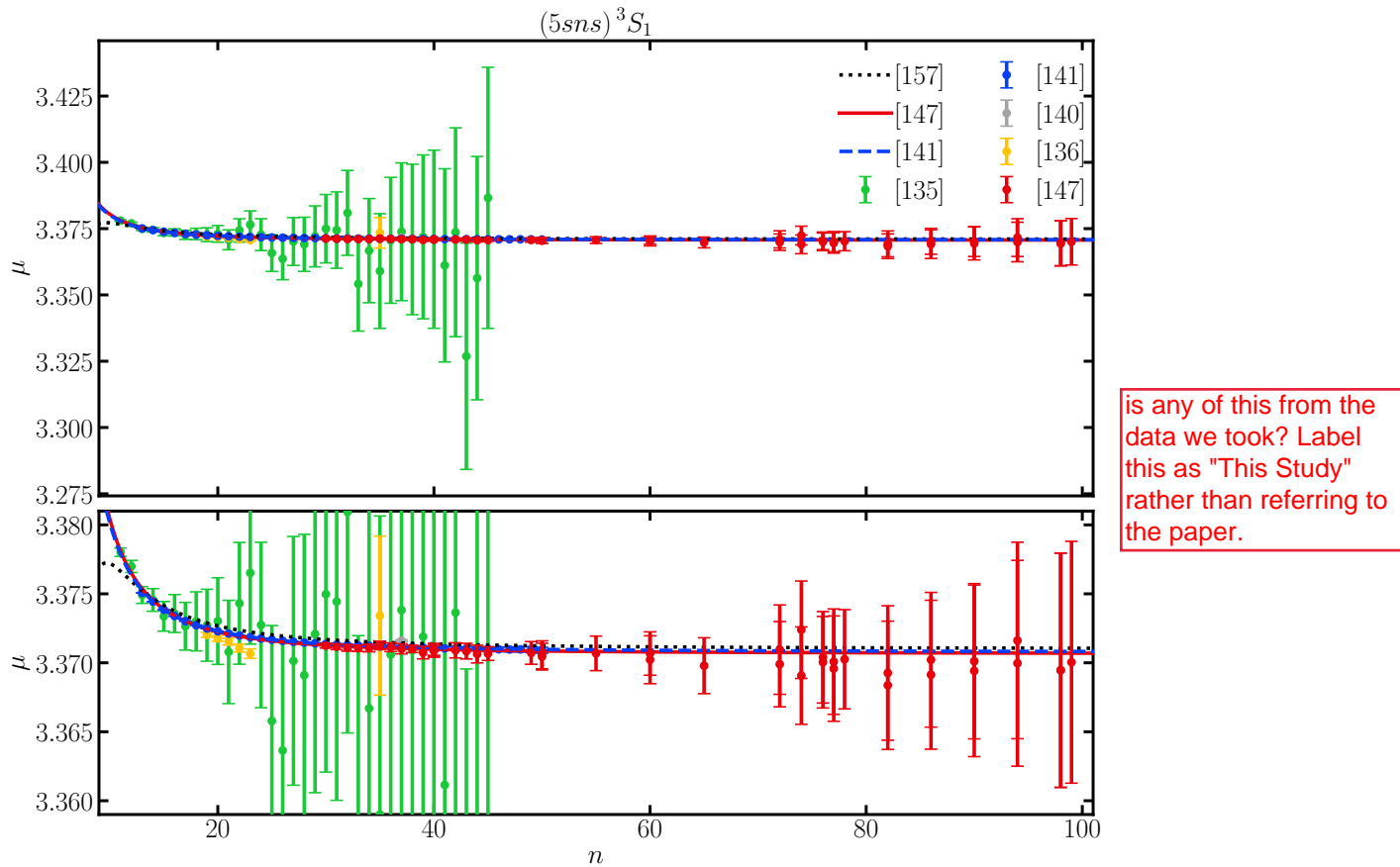


Figure 3.8: Quantum defects for the  $(5sns) ^3S_1$  Rydberg series. For  $^{88}\text{Sr}$ , the quantum defects were calculated from the term energies reported in [135, 136, 140, 141]. The quantum defects from the  $^{87}\text{Sr}$  data was extracted after removing the hyperfine shift.

\*\*\*\*\*

These figures also includes the best theoretical fit to the data that could be obtained. This was realized by first determining the values of the quantum defects  $\mu_{n,S,L,J}$  that best reproduce the measured energy levels and then using these to update the Rydberg-Ritz expression (\*\* 16 \*\*) for the  $n$  dependence of the quantum defect at high  $n$  (see \*\* Table III \*\*). The predicted levels shown in \*\* Fig. 7 \*\* are derived using the updated Rydberg-Ritz formulas. However, since the measured quantum defects of  $^{88}\text{Sr} ^1D_2$  states (with  $I = 0$ ) are available up to  $n = 70$ , the Rydberg-Ritz expression from \*\* [18] \*\* is used for these states. The measured quantum defects for the  $^3D$  states are shown in \*\* Fig. 8 \*\* together

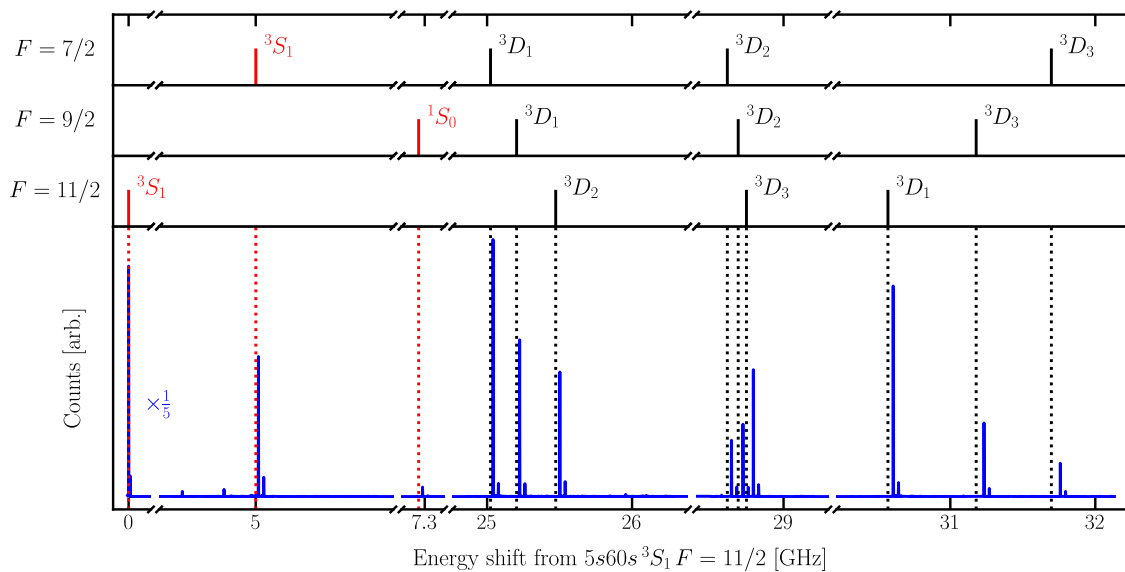
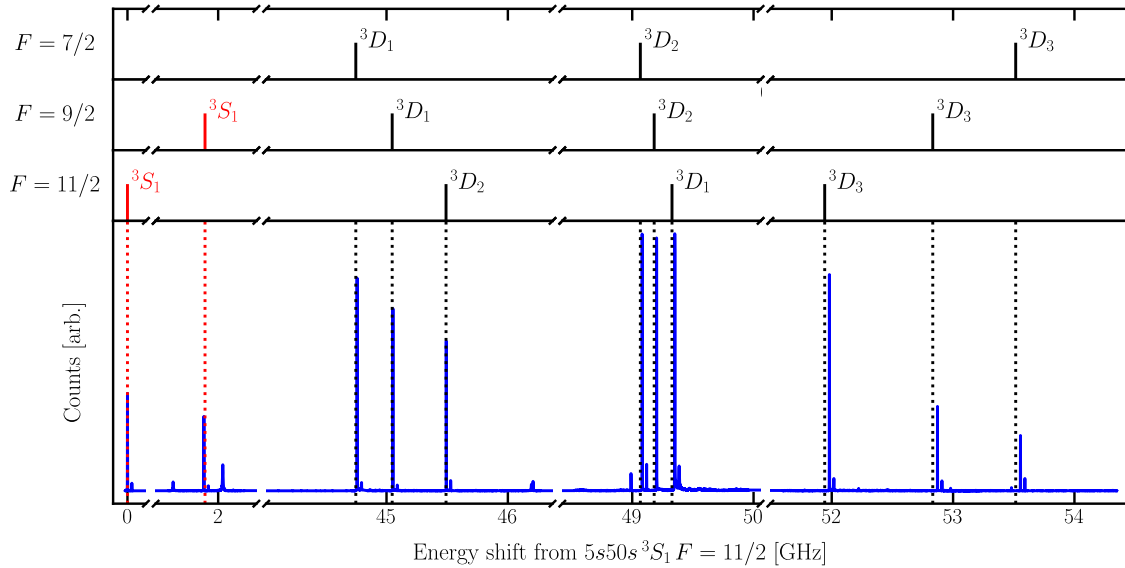


Figure 3.9: Experimentally measured and theoretically predicted spectra for  $D$  states near  $n = 50$  plotted relative to the  $(5s50s)^3S_1, F = 11/2$  state. The vertical bars above the data show the calculated positions for the various hyperfine states. The measured energy levels and splittings are given in Tab. 3.3.

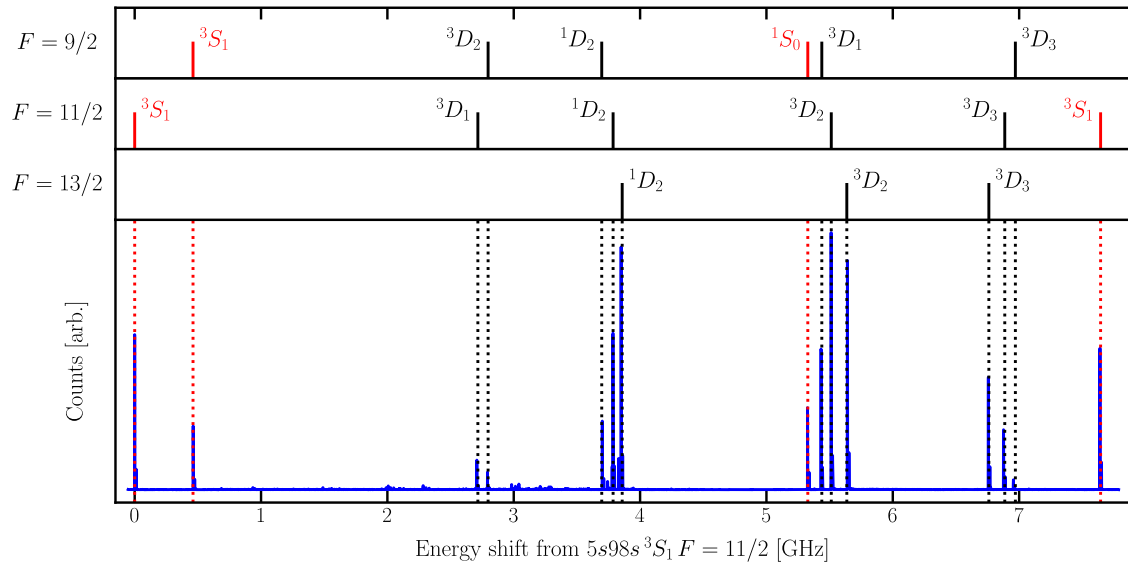


Figure 3.11: Experimentally measured and theoretically predicted spectra for  $D$  states near  $n = 98$  plotted relative to the  $(5s98s)\ ^3S_1, F = 11/2$  state. The measured energy levels and splittings are given in Tab. 3.3.

with the values given by both the present and the earlier Rydberg-Ritz expressions. The differences between the predicted quantum defects \*\* [Eq. (16)] \*\* based on the present data for  $^{87}\text{Sr}$  and previous data for  $^{88}\text{Sr}$  \*\* [18] \*\* appear to be small,  $\sim 0.02$ . However, when converted to energy, this small difference translates into discrepancies of 130 MHz for  $n = 100$  and 1 GHz for  $n = 50$  well outside the uncertainty of the current experiment.

The present Rydberg-Ritz formulas can also be tested against earlier measured quantum defects for  $D$  states in  $^{87}\text{Sr}$  ( $n > 100$ ) \*\* [26] \*\*. The data are reproduced to within an average difference of  $\sim 60$  MHz. When the modified ionization limit discussed above is used to evaluate the quantum defect, the average difference is reduced to  $\sim 25$  MHz. These residual differences could be caused by stray fields present in the heat pipe used for the earlier work. Additionally, the current theoretical model can predict the hyperfine structure of  $D$  states around  $n \simeq 280$ , which can again be compared with the earlier measurements \*\* [40] \*\*. Due to the uncertainty in the ionization threshold, the exact energies cannot be evaluated but the size of the hyperfine splittings is well reproduced within an error of 10 MHz.

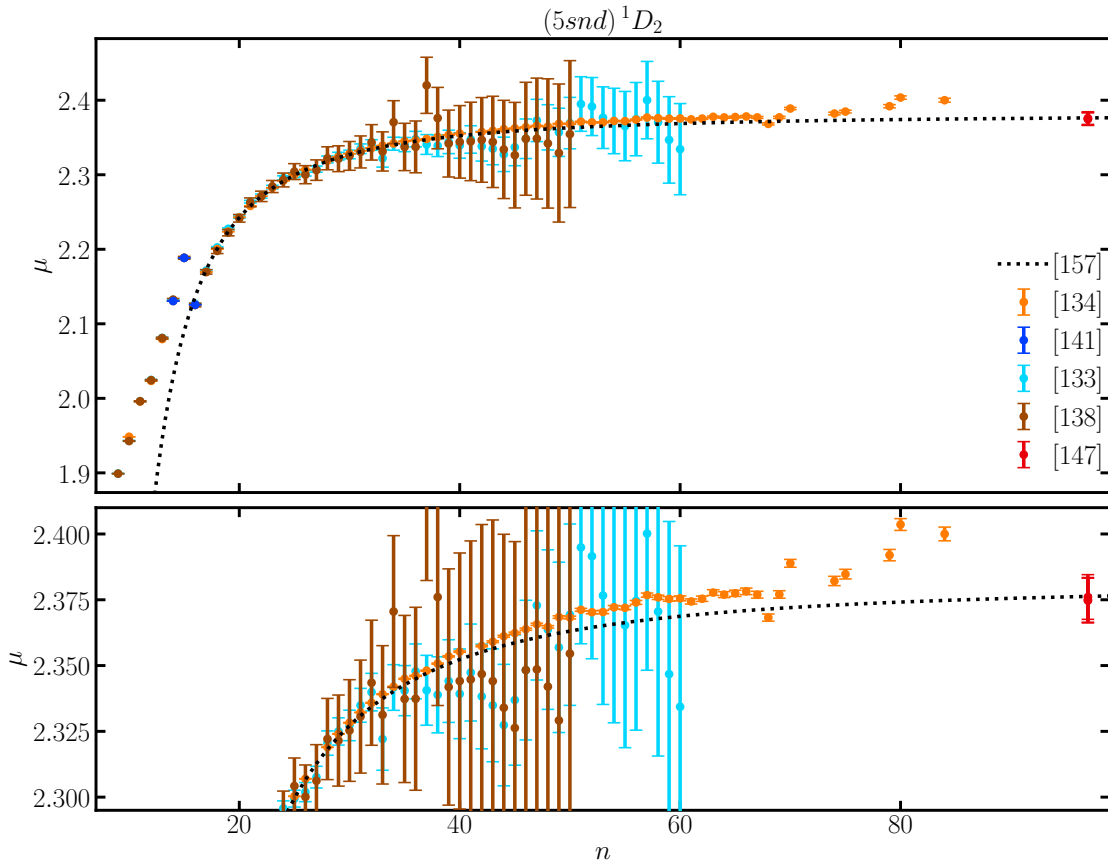


Figure 3.12: Quantum defects for the  $(5s5d)$   $^1D_2$  Rydberg series. For  $^{88}\text{Sr}$ , the quantum defects were calculated from the reported term energies. The quantum defects from the  $^{87}\text{Sr}$  data was extracted after removing the hyperfine shift.

Finally, the improved Rydberg-Ritz formulas for the  $^3D$  states determined from the present data for  $^{87}\text{Sr}$  can be used to determine spectroscopic information for  $^{88}\text{SrSr}$ . When we compare energies for the  $5s50d$  and  $5s80d$   $^3D_{1,2}$  states derived using the present updated Rydberg-Ritz formulas with earlier measurements \*\* [50,51] \*\* the agreement is significantly improved over that obtained using the earlier Rydberg-Ritz parametrization, the differences between theory and experiment being reduced by several hundred megahertz.

As a further test of the present theoretical approach, \*\* Table II \*\* includes the frequency separations between selected pairs of levels that could be measured during a single FSR scan of the 319 nm laser and that are known to high precision. \*\* Table II \*\* also

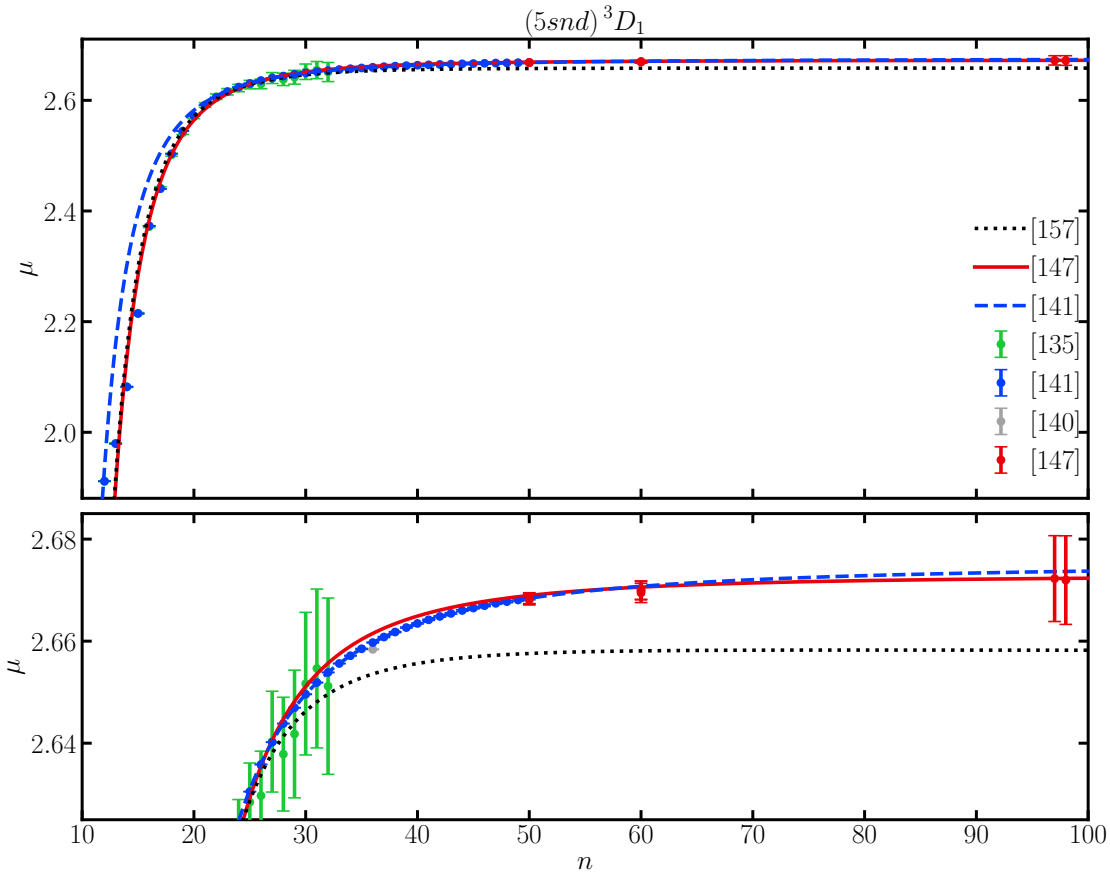


Figure 3.13: Quantum defects for the  $(5s^{n}d)^3D_1$  Rydberg series. For  $^{88}\text{Sr}$ , the quantum defects were calculated from the reported term energies. The quantum defects from the  $^{87}\text{Sr}$  data was extracted after removing the hyperfine shift.

includes the corresponding theoretical predictions. In all but one case the measured and theoretical separations agree to better than  $\pm 10$  MHz.

### 3.5 Conclusion

\*\* Update and reword the summary from PRA !! \*\*

The present work demonstrates that the energies of high- $n$   $^{87}\text{Sr}$  Rydberg states can be accurately determined by diagonalizing an isotope-rescaled Hamiltonian. This Hamiltonian is constructed using spectral information for the bosonic isotope ( $^{88}\text{Sr}$ ) which has vanishing

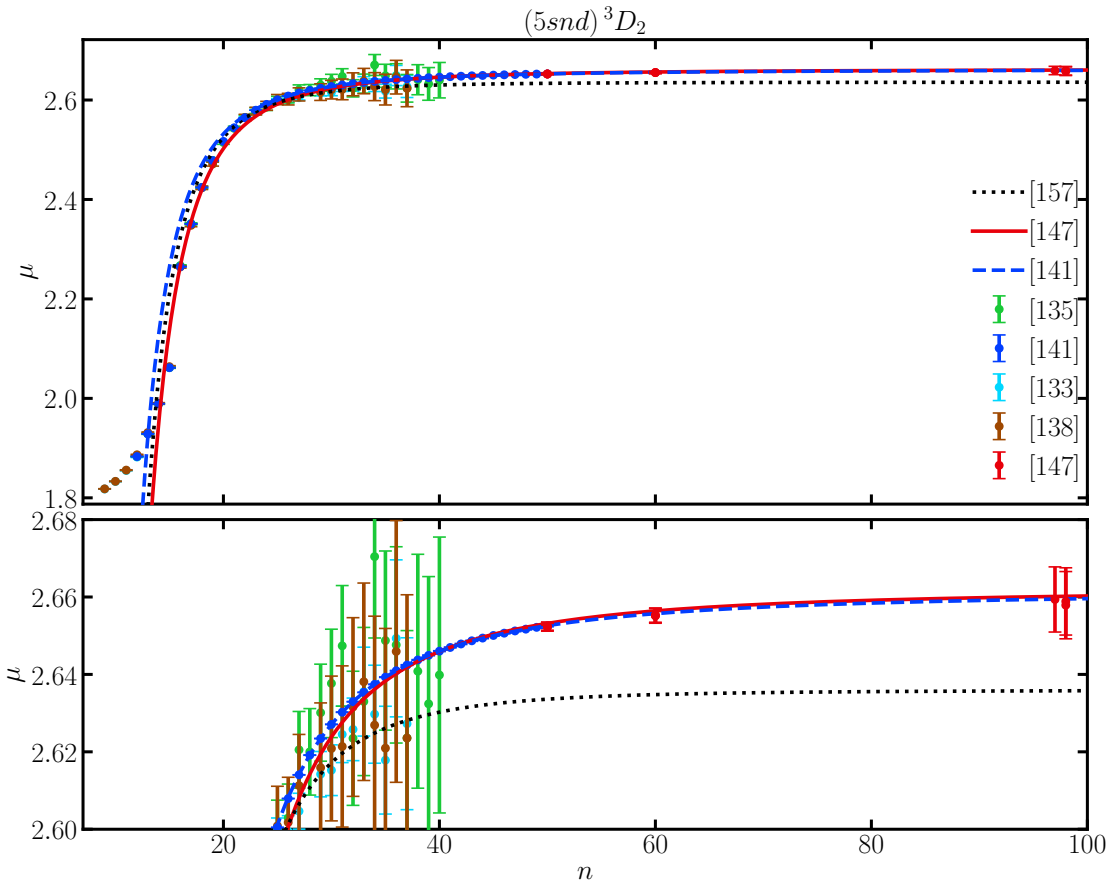


Figure 3.14: Quantum defects for the  $(5\text{snd})^3D_2$  Rydberg series. For  $^{88}\text{Sr}$ , the quantum defects were calculated from the reported term energies. The quantum defects from the  $^{87}\text{Sr}$  data was extracted after removing the hyperfine shift.

nuclear spin combined with the hyperfine interaction present in  $^{87}\text{Sr}$ . The present approach can be implemented for fermionic atoms whenever the energy levels for an isotope with vanishing nuclear spin are available. The method can also be applied in reverse, allowing determination of spectroscopic information, in particular quantum defects, for bosonic isotopes from the hyperfine-resolved spectrum of the fermionic isotope. The major limitation on the accuracy of the present analysis is the uncertainty in the hyperfine-resolved ionization threshold. This uncertainty can be removed by focusing on energy differences to a reference level whereupon accuracies of the order of a few megahertz can be achieved.

\*\*\*\*\*

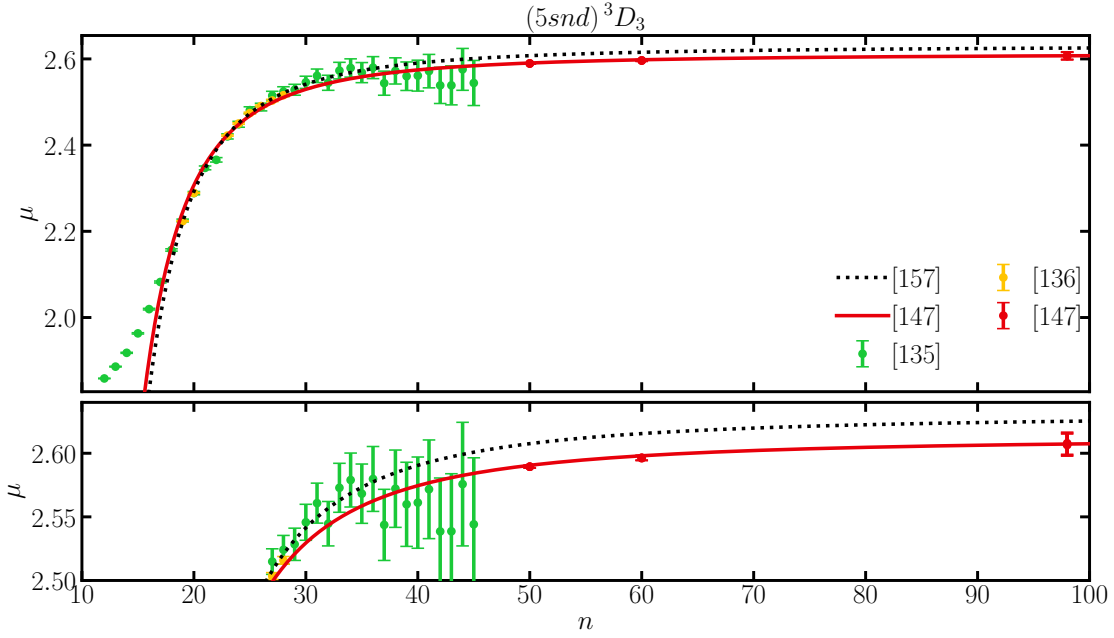


Figure 3.15: Quantum defects for the  $(5snd)^3D_3$  Rydberg series. For  $^{88}\text{Sr}$ , the quantum defects were calculated from the reported term energies. The quantum defects from the  $^{87}\text{Sr}$  data was extracted after removing the hyperfine shift.

Table 3.4: Values of the parameters  $\delta_0$ ,  $\delta_2$ , and  $\delta_4$  for the Rydberg-Ritz formula.

Series	Term	$\delta_0$	$\delta_2$	$\delta_4$	Ref.
$5sns$	$^1S_0$	3.268 96(2)	-0.138(7)	0.9(6)	[157]
$5sns$	$^3S_1$	3.371(2)	0.5(2)	$-1(2) \times 10^1$	[157]
		3.370 65	0.443	-0.553	[147] (this work)
		3.369 24(2)	0.52(2)	-0.1(3)	[140]
		3.370 778(4)	0.418(1)	-0.3(1)	[141]
$5snd$	$^1D_2$	2.3807(2)	-39.41(6)	$-109(2) \times 10^1$	[157]
$5snd$	$^3D_1$	2.658(6)	3(2)	$-8.8(7) \times 10^3$	[157]
		2.673	-5.4	-8166	[147] (this work)
		2.664(7)	-1(9)	$-8(2) \times 10^3$	[140]
		2.675 17(20)	-13.15(26)	$-4.444(91) \times 10^3$	[141]
$5snd$	$^3D_2$	2.636(5)	-1(2)	$-9.8(9) \times 10^3$	[157]
		2.662	-15.4	-9804	[147] (this work)
		2.661 42(30)	-16.77(38)	$-6.656(134) \times 10^3$	[141]
$5snd$	$^3D_3$	2.63(1)	-42.3(3)	$-18(1) \times 10^3$	[157]
		2.612	-41.4	-15 363	[147] (this work)

Although the hyperfine interaction complicates the Rydberg spectra of  $^{87}\text{Sr}$ , it does offer some interesting possibilities. One possibility is to access Rydberg states with either attractive ( $(5sns)^1S_0$ ) or repulsive ( $(5sns)^3S_1$ )  $C_6$  coefficients [157] from the  $(5s5p)^3P_1$  intermediate due to the hyperfine mixing.

